NOVEL BIOHYBRID PHOTOVOLTAICS FOR EXPEDITIONARY ENERGY

By

John Michael Williams II

Dissertation

Submitted to the Faculty of the

Graduate School of Vanderbilt University

in partial fulfillment of the requirements

for the degree of

DOCTOR OF PHILOSOPHY

in

Interdisciplinary Material Science

May 13th, 2022

Nashville, Tennessee

Approved:

David E. Cliffel, Ph.D.

G. Kane Jennings, Ph.D.

Douglas Adams, Ph.D.

Janet Macdonald, Ph.D.

David Baker, Ph.D.

For Candace, Candace Nicole, John Michael, Chrystal Naomi, Jai Matthew, and the world you create.

ACKNOWLEDGMENTS

First, I would like to acknowledge my committee, starting with my advisor Dr. David Cliffel, for not only taking a chance on accepting me into his lab and program but supporting me the entire way through. You never hesitated in allowing me to prioritize my family during this time and accommodating my fluctuating schedule. I am forever grateful for your leadership. Additionally, Dr. Kane Jennings for your mentorship as co-chair for my committee and for leading the PSI subgroup. You accepted me and my ideas early on, constantly providing great guidance and sound advice. Dr. Janet Macdonald, thank you for your support, and kindness throughout this process. I have appreciated your very cool and fun approach to the exciting world of nanoparticles since having the privilege of taking your class. On a personal note, it meant the world to be able to empathize with you in raising small children during the pandemic. Seeing you thrive in the academy was an assurance that I could keep going. Thank you. Dr. Douglas Adams, thank you for not only welcoming me to the Vanderbilt campus but also t your work with Army Futures Command. I hope you can see your influence in this work. Lastly, I would like to recognize Dr. David Baker from the Army Research Lab. I cannot thank you enough for agreeing to be a part of this process and allowing me to connect my research interest to your work. Your support, and readiness to have long conversations, and read through the stream of consciousness emails, were key to the success of this research. Thank you.

I want to thank my collaborators in this research, Dr. Kody Wolf, Dr. Chris Stachurski. Matthew Gallazo, William Lowery for quickly getting me up to speed within the lab and helping me every step along the way. A special thanks to my undergraduate researcher who allowed me the pleasure of mentoring her in the lab, E. Dale Wood. Not only was your work invaluable to the overall effort, but I also cherished the opportunity to interact with such an incredible person, with such a bright future. Thank you for the motivation to keep moving forward. I must also thank the rest of the Cliffel lab, and the PSI Subgroup team: Dr. Dusty Miller, Dr. Aaron Daniels, Dr. Dilek Dervishogullari, Dr. Sarah Winn, Dr. Ethan McClain, Margaret Calhoun (BEAT NAVY!), Nicholas Hortance, Grace Buckey, Kaixua Xu, Pragun Tuladhar, Olivia Eldridge, Sammy Calvert, Josh Passianto, Marc Nabhan, and Long Than. Also, my IMS cohort, Lexi Yates, Cal Craven, Jeremy Espano, Braden Terry, Ryan Kowalski, and Katie Browning, thank you for welcoming me to campus and working hard to make me feel both young and cool.

I want to thank my Previous PI from my time at UNC-Chapel Hill, Dr. Elizabeth Loboa. You absolutely took a chance on me, introduced me to serious research, set an incredibly high bar, and did so much to help me

reach it. I cannot thank you enough for the impact you have had on me personally and professionally, and while I didn't believe it when you suggested I would be hereafter my thesis defense way back in 2012, I can't thank you enough for seeing this for me even back then.

I especially want to thank the IMS program and VINSE Staff, Dr. Greg Walker, Dr. Josh Caldwell, Sarah Ross, Alicia McCord, and Alice Leach. You all bent over backward for me, even before I was enrolled, and did everything in your power to ensure I was successful. Additionally, Dr. Padme Radghaven for all of your time, support, and encouragement.

Academically, I would not be here if not for so many great professors and mentors at USMA, including COL (r) Patricia Dooley, LTC (r) Way Fountain, and COL John Burpo. Additionally, for those who mentored me while serving on faculty at USMA to be more than just a scientist, but a better educator, LTC (r) Hailey Clancy, and Dr. Nick Fell. I must also recognize my professional mentors, as I would not have this opportunity if not for their guidance throughout my career: COL (r) Fritz McNair, COL Stevenson Reed, COL Charles Branson, COL Reginal R Davis, COL Tom Saltysiak, COL Debra Thedford, and Dr. Eric Moore.

Most importantly I have to thank my family. My parents John M Williams, DBA, and REV Diana Williams EdD are both such inspirations, and I am so proud to be your son! My incredible sisters, Keisha, Anita, Emojoy, and Dana, thank you for a lifetime of unabashed encouragement. To my wonderful in-laws, John and Faye Norris, Elisa, Jason, John, Tamisha, Andreis, Victor, Tony, Omari, AJ, and Chris, thank you for being family. To my many aunts, uncles, cousins, nieces, nephews, godchildren, and friends, thank you for being there for me.

To my four incredible children, thank you for all you have sacrificed, and for being the absolute best of me. I hope this work will be a source of pride for you, as you are the source of pride for me.

To my incredible wife Candace, I don't have enough words, but will simply say we did it, because of you, we did it, and I love you!

TABLE OF CONTENTS

Page

LIST OF TABLES

LIST OF FIGURES

CHAPTER 1

Introduction: The Need for Expeditionary Energy

This chapter aims to focus on the central question of the research by providing a clear use case for biohybrid photovoltaics. This chapter will provide background on the shifting requirements, current material solutions, and planned path forward to address a growing energy gap on the battlefield, between the energy required, and the energy available.

1.1 Army Modernization/Multi-Domain Operations (MDO)

In his 2016 speech at the Association of the U.S. Army annual meeting and exposition, GEN Mark Milley, the 39th Chief of Staff of the US Army, and current Chairman of the Joint Chiefs of Staff, spoke at length about the future[1]. He highlighted the need for modernization, both technologically, and with regards to our acquisition process, recognizing the variety of threats posed by rival military powers, fragile nation-states, and climate change, to our national security. He stated that while the Army is ready to fight and will remain that way, we must prepare for the future[1]. This speech, which was considered hard-edged by many, was the prelude to several sweeping changes in the Army, and the military overall, including the formation of a new 4-Star headquarters, Army Futures Command (AFC). This also began a paradigm shift away from the counterinsurgency focus that had dominated the military over the 20 years of the Global War on Terrorism, and towards large-scale combat operations (LSCO) and a concept called Multi-Domain Operations (MDO). Multi-Domain Operations, as a concept, aims to coordinate, maneuver, and amass fires across the five domains of Air, Land, Sea, Space, and Cyberspace to maximize effects and lethality with the minimal size force[2,3]. Application of the concept is cyclical, phasing through competition with a near-peer

adversary, penetration of their anti-access defenses, disintegration of their defensive capabilities, exploitation of newfound freedom of maneuver, and re-competing to consolidate gains. This concept demands a more holistic view of the combined force, as well as increased cooperation and coordination across services, drastically changing the size and shape of the battlespace[2,3]. These shifts created new opportunities for research and technology, demanding that the new solutions being developed would address multiple threats, maximizing the return on investment for the army.

Figure 1.1 GEN Mark Milley addressing the 2016 AUSA Eisenhower Luncheon discussing modernization. Photo taken by Chuck Burden and owned by imago/Zuma Press. Front cover of US Army Training and Doctrine Command Pamphlet 525-3-1 describing MDO[2].

Army Futures Command, which was stood up in Austin, TX in July of 2018, was designed to address the recommendations of the Decker-Wagner 2010 acquisition review, creating a unified command responsible for the development of technology and systems over its life cycle[4,5]. It was formed with six modernization priorities provided by Army leadership, which resulted in eight cross-functional teams (CFTs), made up of leaders from the user community, Science & Technology community (S&T), and acquisition community with the responsibility of developing "quick wins" by directing immediate and short term investments. The eight CFTs are Future Vertical Lift, Next Generation Combat

Vehicle, Air and Missile Defense, Soldier Lethality, Long Range Precision Fire, Synthetic Training Environment, Assured Position Navigation & Timing, and the Army Network. The army then redirected billions of its S&T funding to support these 8 efforts[6]. While each of the CFTs is separate and unique, many of the immediate and near future solutions being developed across the board include teamed robotics, delocalized sensors, and networked warfighters[7].

The designed applications are aligned with the current focus on LSCO and MDO, which changes the perspective of the battlefield in recognition of how different domains interact. Traditional doctrinal terms, like "Forward Line of Troops" (FLOT), or the "Deep Sustainment Area", are no longer applicable[2,3]. Nor are the stovepipes that separated different services on the battlefield, restricting the Air Force to the air, and the Navy to the water. The new doctrine being produced by AFC with regards to MDO, (AFC 71-20 series), highlights these ideas in future concepts[8]. The inclusion of the Cyberspace and Space domains, and recognition of the need to converge all domains to maximize effects, has forced better integration across the services, with distributed impact throughout the battlespace. This further emphasizes the importance of teamed robotics supporting everything from port operations to air refueling and active combat. Delocalized sensors, distributed from the deep rear echelon and forward, provide real-time information on the state of the battlefield, while serving as communication and positioning nodes. Warfighters are connected with advanced communications equipment, as well as systems to augment reality, improving situational awareness, and lethality at the individual and squad level. What all of these new capabilities have in common is an increased demand for expeditionary energy.

1.2 Current Expedition Energy Paradigm

Expeditionary energy is the energy that is required by forces to conduct operations within the battlespace. The energy gap is the difference between the required amount of energy, and what can be transported to or produced within the battlespace. In speaking with leaders from the two acquisition organizations required to produce material solutions for expeditionary energy, Project Manager Expeditionary Energy & Force Sustainment (PM EEFS), and Product Manager Ground Soldier Systems (PdM GSS), the energy gap has been steadily increasing over time, but modernization has made the problem much more urgent. The current methodology for providing expeditionary energy has relied heavily upon fossil fuels and rechargeable batteries. Much of the portfolio for PM EEFS includes large-scale, mobile, or small-scale fossil fuel-based generators for use in combat operations[9]. PdM GSS, as part of PM Integrated Visual Augmentation System (PM IVAS), is responsible for soldier tactical power, with a portfolio that includes conformal wearable batteries, squad power management systems, and the integrated soldier power and data system as part of the Soldier Worn Integrated Power Equipment System (SWIPES)[10]. This portfolio reflects the impact the growing energy gap has had on dismounted warfighters over the last two decades in combat, where increased technologies like scopes and radios kept adding new unique batteries, and their weight, to the basic load of the Soldier, reaching an unsustainable level[11]. The SWIPES gear, with its rechargeable battery and power distribution system, reduces the weight from unique batteries and simplifies powering the dismounted soldier. PM EEFS is currently developing a similar system at a large scale called the Secure Tactical Advanced Mobile Power program, to utilize a hybrid of vehicles, batteries, and generators to more efficiently distribute energy to units with smaller footprints[12]. Unfortunately, as new technology adds new power

demands, the requirements for battery capacity must increase, as well as new requirements for recharging the batteries while on a mission.

While research on improving battery materials and performance is ongoing, additional work is being done to add more energy-generating capabilities within the expeditionary energy portfolio. The current dependence on fossil fuels is not sustainable for several well-documented reasons. Long slow fuel convoys have been especially vulnerable targets during combat operations in both Iraq and Afghanistan, often victims of improvised explosive devices and ambushes, resulting in a leading cause of death for Soldiers and contractors[13]. Additionally, the source of the fossil fuels used by the military can create economic and defense ties that strain strategic political alliances[14]. More recent concern with the use of fossil fuels is the environmental impact of burning the fuel, recognizing that even the most efficient tactical generators are still producing waste without using the majority of the electricity produced. The US army has recognized the importance of its environmental impact and as part of its recently released climate strategy, has invested in efforts to develop renewable energy solutions for new technologies, making sustainability a critical attribute of new system acquisitions[15].

AFC is working closely with program offices to research and develop renewable energy generation technologies, reaching out to both industry and academia for solutions. Groups, such as the Army's Energy Informed Operations Program are working with PM EEFS on the STAMPs Joint Capability, and the Solar Sustainable Integrated Collaborative Environment (SolStICE) working with PdM GSS, are helping develop long term plans with both civilian and operational impact[12]. PdM GSS is currently fielding a 120 W solar blanket, weighing 5.6 lb, with an area of 10 ft^2. The system uses an array of thin-film crystalline silicon solar cells, that are durable in extreme weather but demonstrate less than

5% efficiency[17]. These systems provide the size, weight, performance, and cost (SWaP-C) baseline for future fielded technology. PdM GSS, working with SolStICE, has already established a long-range plan to upgrade these systems over the next two decades, transitioning from monocrystalline silicon thin films to amorphous silicon, and eventually, perovskite solar cells. This plan is based on the demonstrated performance observed in early research, but the goal is to eventually field a solar blanket that is capable of producing 300-500 W, weighing 2-4 lb, with an area of 14 ft^2. Perovskites are a focus of the group due to their tunable band structure, direct band gaps, high solubility in water, and the elimination of rare earth elements, which represent a strategic supply line risk[17]. As with all military acquisition efforts, the team is looking to balance risk between the total life cycle cost of a system, the schedule of development and production, and its ability to perform the requirements. The group will be looking for key maturation points for the technology to minimize risk to the schedule, namely, stability of the active layers, scalable deposition methods, and encapsulation. Beyond the technical maturity, the team is tracking the price per unit of energy produced, as solar power remains one of the more expensive renewable energies by that metric, with much of the cost due to the price of silicon wafers. Over the next 20 years, the team looks to see that metric shift from where it is currently, at roughly $10/watt produced in the field, to $1.50/ watt produced. This research emphasizes the need to improve the efficiency and stability of photovoltaics, as a means of reducing the cost of energy produced. The improvements though must be made in balance, suggesting a new technology that increases efficiency, cannot reduce stability so much that more devices need to be purchased in the same period, and the cost of the improvement cannot add to the price of the energy produced. Fortunately, the group's many collaborators are taking advantage of the global interest in this technology to move

the effort forward.

1.3 Opportunities with Synthetic Biology

In addition to the investments by AFC towards modernization efforts, the Army has placed special emphasis and investments into the field of synthetic biology, making it a priority research area[18,19]. This interest is in recognition of the ability of nature to solve a complex problem, efficiently, especially at the micro and nanoscale. Much of the focus for this effort is in developing new materials for survivability, leveraging biological materials for their strength, self-assembly/self-healing, and camouflage capabilities[18,19]. While energy generation is not mentioned as one of the goals within the synthetic biology push, the two areas of research intersect at biohybrid photovoltaics, or solar cells based on the machinery of photosynthesis. Biohybrid photovoltaic research goes back decades and can include everything from full thylakoid stacks to individual membrane-bound protein complexes, to light-harvesting chlorophylls[20-23]. Photosynthesis uses solar energy to drive electrons and create chemical energy in the form of sugars within the plants, algae, and bacteria that use the process. The machinery can be applied to accomplish similar goals, with some notable advantages. First, the materials are ubiquitous and cheap, growing on land and within water all over the globe, meaning there is no strategic risk with regards to the material supply chain, and no means to drive up the cost. Next, the material is renewable and benign, without limit to how much can be produced, or risk from how it is disposed at the end of its life cycle[20-23]. Finally, the proteins are already optimized to absorb light and efficiently translate the energy. Unfortunately, the materials are not known for their stability and can degrade quickly. The efficiencies observed within

biohybrid systems are well below performances seen in other devices. While the army is invested in some biohybrid photovoltaic research, in general, these systems have not been a priority, as the research does not fit the paradigm of increased efficiency and stability to reduce cost per unit energy[24-28]. A shift in that paradigm though may offer a new perspective in biohybrid photovoltaic research. Instead of a focus on efficiency and stability, a device could be designed for limited use, at a cost so low the systems could be considered disposable. This model would take advantage of the cheap materials to offer a supplemental energy generation capability, using local resources like vegetation, to temporarily provide energy at the point of need.

The central aim of this research is to design a solid-state biohybrid photovoltaic based on that shifted view of expeditionary energy generation requirements. In short, modernization is increasing the demand for energy on the battlefield, and to meet that demand we will need to generate energy that is both low cost and environmentally benign. Biohybrids can meet this need by taking advantage of the abundant and renewable plant materials. The goal will be to introduce materials and fabrication techniques that reduce the cost dramatically, while maintaining the limited impact on the environment, and demonstrating enough efficiency to garner further investment. While the technology is not yet mature, success in this endeavor will provide a starting point for more in-depth consideration.

CHAPTER 2

Foundations in Emerging Photovoltaics

This chapter aims to provide background information about current and emerging solid-state photovoltaic devices. The goal is to describe how they work, key features, and future development. Additionally, this chapter will attempt to compare different types of solid-state photovoltaics in terms of the key performance attributes of size, weight, performance, cost (SWaP-C), and sustainability to better understand how they fit within the army's need for expeditionary energy

2.1 The National Renewable Energy Laboratory

Over the last 50 years, energy has held a key role in the economic and political health of the nation, as well as a critical consideration for our national defense. The political shifts in the middle east of the 1970s resulted in fuel shortages, with enormous impact on the US economy, and everyday life. In response, President Ford established the Energy Research, Development and Demonstration Administration, that would later become the Department of Energy, and the Solar Energy Research Institute, which would become the National Renewable Energy laboratory (NREL)[29]. This lab holds the responsibility of conducting, publishing, and advancing the science and engineering technology of clean renewable energy. In addition to advance research on the various clean energy generating sources, like solar, geothermal and wind, this charter also directs efforts in energy analysis, infrastructure, transportation, and integrated solutions[30]. NREL provides a clearing house of information on the latest break throughs in solar capabilities, annually publishing reports on novel photovoltaic performance, economic benchmarks on solar production and storage, as well as a graphic showing the improvement of PV system efficiency by type

over time. That last document, the "Best Research-Cell Efficiencies" divides photovoltaics into five categories (Multijunction Cells, Single Junction Gallium Arsenide cells, Crystalline Silicon Cells, Thin Film Technologies, and emerging photovoltaics) and describes the highest efficiencies reported by year, beginning in 1975. In the most recent version (dated July 2021) the highest performing system was a six junction system achieving 47.1% efficiency with the use of a concentrator, produced and tested at NREL. This chart helps to highlight the state of the art within the field of photovoltaics, as well as depicting the rate of change within a particular field, allowing for better predictions about future development and performance. Emerging PVs, while demonstrating the lowest overall efficiencies of the five categories, has shown some of the greatest improvement in the shortest time, and thus, are promising for long-term investments for future systems. Many review publications focus on the improvement in efficiency of different types of photovoltaics, and NREL annually publishes updates with new PV characterizations being reported in literature. Few efforts though, focus on the key performance attributes that are used to evaluate the maturity of the technology, and its readiness to transition into a program of record. This effort will review three types of emerging photovoltaics, solid-state dye sensitized solar cells (ssDSSC), organic photovoltaics (OPV), and perovskite solar cells (PSC), providing not only background and function, but an evaluation based on SWaP-C, and environmental impact.

2.2 Solid-State Dye Sensitized Solar Cells

The dye-sensitized solar cell provided a paradigm shift in the design and fabrication of photovoltaics since 1991 when O'Regan and Gratzel demonstrated efficient systems[32]. The dye within the cell is responsible for absorbing the photons of light, generating the

charge carriers, and transferring the electrons directly to the semiconductor nanoparticles. The semiconductor then transfers the electrons to the transparent conductive metal oxide electrode, and on to the external load. The dye is then regenerated by a redox electrolyte, which transfers the charge carriers between the counter and working electrodes[33-35]. These systems produced efficiencies over 14% percent, and the low cost of materials suggested the technology was promising for future energy requirements. However, the liquid electrolytes presented a number of challenges, as they were often corrosive, flammable, volatile, toxic, with a tendency to leak or evaporate. Solid-state Dye Sensitized Solar cells address this issue by replacing the liquid redox electrolyte with a solid heterojunction made up of wide bandgap semiconductor, an organic semiconductor, or a polymer electrolyte to serve as the hole transport material[33-35]. Benesperi et al. published a thorough review in 2018 explaining the function, kinetics, and impact of different materials within ssDSSC[34].

These devices are generally composed of the same features seen in traditional DSSC. The working electrode, or anode, is generally composed of a transparent conductive metal oxide, such as Indium doped Tin Oxide (ITO) or Fluorine doped Tin Oxide (FTO), coated on glass slides. A thin compact blocking layer, usually, TiO_2, is added directly onto the conductive surface to minimize shorts and recombination at the anode surface[37-42]. Next, a nano- or meso-porous layer of a wide bandgap semiconductor is sintered onto the electrode surface, to act as a substrate for the dye[43-48]. The increased surface area allows for more dye to be loaded within the system, and ultimately, for more charge carriers to be generated from absorbed photons. The dye itself can be metal-organic complexes, designed to absorb specific wavelengths of light, or naturally occurring organic dyes, like the anthocyanin used within the original Gratzel cell[32-36]. The dye is usually bound to the

nanoporous layer by its functional groups. The hole transport material must be energetically aligned with the organic dye to ensure a favorable flow of charge carriers. The thickness of the layer is also a critical consideration, as the layer can add serial resistance with increased thickness, impacting performance[34]. While layers that are too thin may include structural defects like pinholes or fissures that allow for shorts or recombination within the layer[34]. The working electrode is usually a metal or carbon material, energetically aligned so that it can accept holes from the transport material.

Of the different material layers, the hole transport material and dye are the layers most unique to ssDSSC. Devices using polymer electrolytes, where salts are fixed within a polar polymer matrix, allowing both electrical and ionic charge transfer within the device, demonstrate high conductivity and stability, but still suffer from ineffective pore filling, and a low dye regeneration rate. Gel Polymer electrolyte address that issue by entrapping liquid electrolyte within the gel polymer matrix, producing a quasi-solid-state DSSC with efficiencies similar to those observed in traditional DSSC[34]. In contrast to the polymer electrolytes that leverage ion transfer to regenerate the dye, most other hole transport materials used in ssDSSC use molecular charge hopping through the material itself. A common material used in early ssDSSC is spiro-OMeTAD, developed by Bach et al in 1998, and composed of aromatic rings connected with nitrogen[49]. The shifting pi bonds within the molecule allow for effective electron charge hopping through the material. While early ssDSSC were optimized and efficient with this material, and it became the HTM of reference, spiro-OMeTAD presented a number of challenges that held back further advancement of ssDSSC, including poor conductivity and poor long-term stability. Additionally, the process to produce and apply the material was expensive, complex and time consuming, limiting the commercial application of the material[34,49-52]. Other HTMs

used within ssDSSC are small molecules, like those based on triphenylamine, and demonstrate a tunable energy level with additional molecular moieties, ideal for designing the appropriate band alignment[34]. These materials also have the advantage of small size, that allows them to better fill the pores of the nano porous layer for more efficient charge transfer[34]. The small molecules are generally poor conductors and can add to the serial resistance of the device. Polymer based HTMs allow for faster charge transfer, as the long polymer chains with overlapping pi bonds permit efficient movement of charge carriers. The size of the polymer, and the process of its application can limit its ability to interact with fully with the pores of the nano porous layer. Dopants and additives can be used to change both the energy level of the HTM and its conductivity, improving the performance of the device overall[34,35,53,54].

The requirements for the dye sensitizer include the ability to absorb standard wavelengths of light to generate charge carriers, and also possessing a functional group, like carboxylate or silyl, that allows it to strongly bond or complex directly with the nano porous layer for charge injection. The dye must evenly coat the transport layer to reduce recombination on the nanoparticle surface, which hinders device performance. While new dyes are regularly developed for standard DSSCs, the additional requirement of band alignment with the HTM adds complexity to the dye choices for ssDSSC[34,35]. The ruthenium-based metal organic dyes that produce efficiencies around 10% in traditional DSSCs are also used in ssDSSC with significantly lower performance, though some studies have shown improved efficiencies through additives and co-absorbers that increase the wavelengths of light absorbed, or the length of the dye to nanoparticle bond, or adding hydrophobic tails, all of which reduce interfacial recombination[34,35]. Organic metal-free dyes based on triphenylamines have demonstrated the highest efficiency within ssDSSC,

with a number of notable improvements over the ruthenium dyes, namely, the metal component is toxic, rare, and relatively expensive[34,35]. Porphyrin-based dyes are large aromatic molecules complexed with a zinc center. Overall, they represent an improvement over the ruthenium-based dyes as they are more sustainable, adjustable, and cost-efficient, with a higher extinction coefficient, which allows for more absorption of light with a thinner layer of dye[34,35]. Inorganic nanoparticles called Quantum Dots are currently being studied as dyes, leveraging the unique electric and optical properties associated with their size to absorb light at different wavelengths and inject charge carriers into the anode[55].

The introduction of the solid-state heterojunction saw an immediate reduction in performance, as the new layer increased impedance with ineffective pore filling between the mesoporous nanoparticle layer and the new hole transport material. The new interface also became the site of electron recombination within the device, reducing both current and potential. Lastly, the reduced conductivity of the new material added resistance to the device, which also decreased performance.

2.3 Organic Photovoltaics

Organic photovoltaic cells (OPVs) use the photovoltaic effect on conductive polymers and small organic molecules to generate electron flow from absorbed light[35,53,56-65]. Unlike other photovoltaics, which generate free charge carriers, these systems rely on the junction of electron donor and acceptor materials, where confined excitons are exchanged directly. The donor material, with a smaller electron affinity and ionization potential, absorbs the photon to generate the electron-hole pair. The excited electron is transferred from the highest occupied molecular orbital (HOMO) to the acceptor material's lowest unoccupied molecular orbital (LUMO), while the hole generated at the HOMO is transferred away towards the cathode. The acceptor material, with a greater electron affinity, and lower

energy LUMO, receives the excited electron from the donor material, before transferring it towards the anode. [35,53,56-65] The open circuit potential within these systems is ideally the difference in energy between the HOMO of the donor material, and the LUMO of the acceptor material; however, OPVs traditionally suffer from relatively low Voc. The potential of the device can be reduced by recombination within the cell, and is impacted by temperature, light intensity, work function of the electrodes, and material microstructure[69].

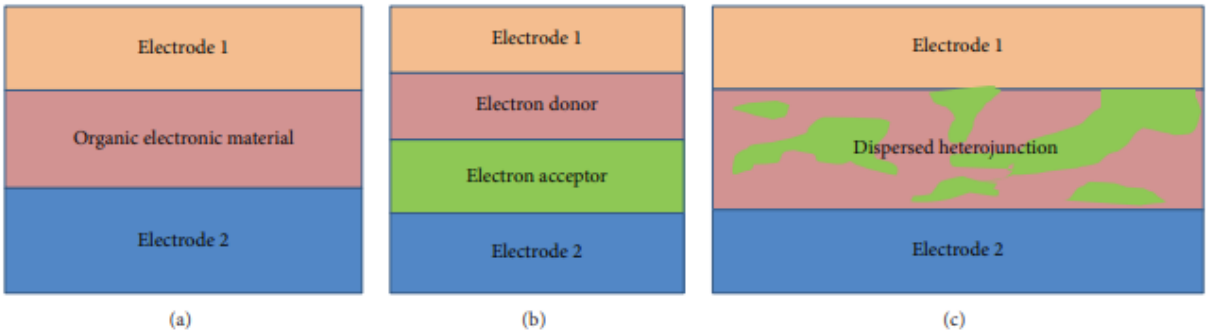

Figure 2.1. Schematics of typical OPV structures based on a single junction, Heterojunction, and Bulk heterojunction designs. Image is taken from Rao et al.[65]

Like other emerging photovoltaics, OPVs still rely on energetically aligned charge transfer layers to allow carriers to efficiently travel to their respective electrodes. Transparent conductive metal oxide-coated glass slides are still utilized as electrode materials, as well as metals, energetically aligned based on their work function. Polymer-based OPVs can be arranged with singular junctions, as the organic material is sandwiched in layers between the conducting electrodes, or in bulk hetero-junctions where the materials are blended to maximize the surface area of interaction between the donor and acceptor[56-65]. Conjugated polymers, like polyaniline (PANI), polypyrrole (PPY), and poly(3,4-ethylene dioxythiophene) (PEDOT), are used within these devices based on the delocalized electrons along the polymer backbone. When doped with counter ions, or more polar organic molecules, mixed oxidation states along the polymer chain make the material conductive and allow charge carriers to move freely across the material[53,56,66,67].

The conductive polymers used within these devices are dependent on the electrochemical properties, like conductivity, and energy bandgap, but also on their processability, as many conductive polymers are insoluble in common solvents, or fabrication methods produce heterogeneous properties[66,67]. Other polymers suffer mechanical photodegradation and cannot withstand the stresses associated with a functional photovoltaic, including atmospheric, electronic, or temperature changes. These shortcomings reduce the feasibility of certain polymers whose efficiencies within a laboratory environment may seem ideal. To address these issues, some devices have incorporated encapsulation with a protective polymer to limit the impact of environmental stressors on the performance of the cell[68].

The efficiencies observed in OPVs are comparable to other emerging photovoltaics, but still below the average observed in inorganic systems. The devices are thin, and flexible, owing to the mechanical properties of the polymer makeup, and often the lack of crystalline semiconductors. These properties are ideal for future applications like conformal power generation for robotic systems, or wearable electronics. Additionally, because the different layers are predominately composed of polymers, simple and cost-effective manufacturing practices can be applied to the production of the devices.

2.4 Perovskite Solar Cells

Perovskites are a family of materials of critical research interest right now due to their optoelectrical properties. The chemical structure is usually described as ABX_3, where A is the monovalent cation, B is a divalent metal, and X is a Halide, producing a crystal structure with unique properties[17,35]. In general, the A material is set within a cuboctahedral space formed by the nearest neighbor X atoms for an AX_{12} configuration, while the B material is coordinated within an octahedral shape of X nearest neighbors, with a BX_6 configuration. The tunability of the optical, mechanical, chemical and

electrical properties of perovskites is based on the multiple permutations of A, B, and X within the same crystal structure. Though there are constraints as to the size of the substances used within each lattice point, and the various combinations can impact the stability of the material, the ability to slightly shift the spacing within the crystal structure allows the material to be designed with specific properties[17,35,70]. The density of states analysis of MHP shows many are direct bandgap semiconductors, with conduction band electrons having similar effective mass. This is ideal for photovoltaic applications as it suggests the absorbed energy from the photon will be more efficiently transferred to the electron, without losing energy to momentum[17].

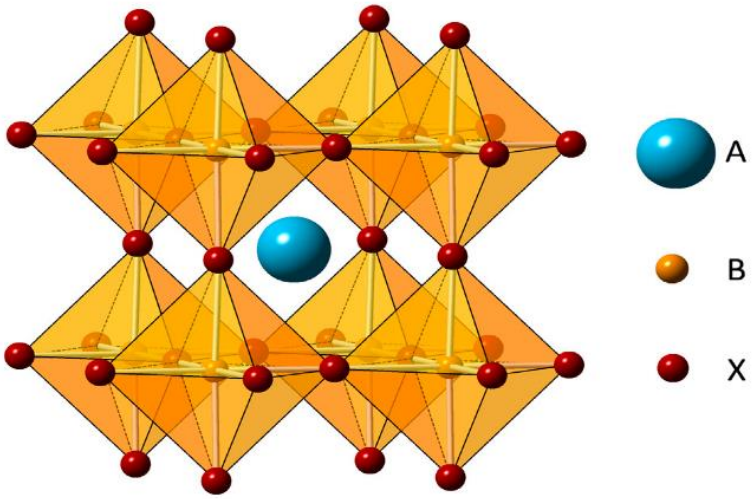

Figure 2.2. General crystal structure of an ABX_3 perovskite. Image is taken from Luceno-Sanchez et al.[35]

The first perovskites were reported in 1839, though early research focused on optical applications in pigments and paints, with electrical applications not studied until the mid-1940s[17]. Optoelectronic work with perovskites, both metal halide, and metal-organic halides, demonstrated the tunability of the material, and how the molecular structure could be adjusted with precision. The current interest is based on their recent application as a tunable light absorber in photovoltaic cells, with advances in efficiency being generated in

a relatively short period[17,35,70-72]. The first application of perovskites within a photovoltaic was reported in a 2009 paper which applied methylammonium lead iodide ($MeAPbI_3$, $CH_3NH_3PbI_3$) as a dye within a DSSC, bonding the perovskite to TiO_2 nanoparticles, using a liquid electrolyte, demonstrating efficiency of 3.9%[72]. The perovskite served as the active layer, absorbing photons of light, and generating charge carriers within the device. In later efforts, the perovskite material was applied in a thin layer, directly between the HTM and ETL, like OPVs, taking advantage of the relatively high extinction coefficients that allow more light to be absorbed by a thinner layer[17,35,72]. Carrier generation within the single material is one of the key advantages of the PSC, as excitons do not need a long life span, and energy is not lost in charge carrier movement. Today, in addition to PSCs achieving over 20% efficiency, perovskite layers are being applied in multijunction cells with other types of active layers, increasing the spectrum of light absorbed and raising the overall device efficiency.

PSC research has benefitted from the work done to improve both ssDSSC and OPVs, leveraging many of the same technologies for HTM, ETL, blocking layers, and layer applications. The advantage of PSCs over other emerging photovoltaics is found within the material properties of the active layer. One key disadvantage is the stability of the perovskite material, which demonstrated degradation in response to heat, moisture, oxygen, thermal influence, applied voltage, intense light, and mechanical strain[17,35]. Additionally, imperfections within the lattice structure can result in heterogenous properties and reduce performance. To overcome these issues, many researchers are looking for methods of encapsulation to shield the perovskite active layer[73-75]. Also, improvements in the composition, deposition method, and cell architecture are being applied to optimize the performance of the material for photovoltaic applications.

2.5 Evaluation

The field of emerging photovoltaics has demonstrated drastic improvement in performance over a very short period, and continued investment will be necessary to meet future energy needs. While the three design classes have some distinct differences, they each have roots in the DSSC and share many of the same advances. Most still use transparent conductive metal oxide-coated glass as an electrode. All three still leverage solid-state charge transfer layers, using many of the same materials and fabrication techniques to produce HTMs and ETLs. An objective evaluation of the different classes would then be based upon the active layers, as the generation of charge carriers is the primary difference between the three. The ssDSSC rely on organic and inorganic dyes, OPVs use a difference in energy between conjugated polymers and small molecules, and PSC leverage the tunable properties of the perovskite crystal structure. Comparing the maturing technologies will require an even application of certain evaluation criteria. In discussing this topic with leaders from the PdM Ground Soldier System team, specifically working on the long-term photovoltaics plan, the evaluation criteria they use primarily is size, weight, performance, and cost (SWaP-C), with the ultimate goal of reducing the price per unit of energy produced. Other criteria like environmental impact, scalability, and durability also matter, but not to the same extent. According to the NREL 2021 chart, the emerging photovoltaics with the best performance in each of these three classes was a PSC which demonstrated an efficiency of 25.5%, an OPV that demonstrated 18.2%, and a DSSC that demonstrated 13% efficiency. Looking closely at each study and comparing the outcomes may provide insight on the path forward for each type of device.

The PSC study was produced by Jeong et al. as a collaborative effort between South Korea's Ulsan national Institute of Science and Technology (UNIST) and the Swiss

Federal Institute of Technology Lausanne (EPFL)[76]. The goal of the effort was to optimize the performance of a PSC using a promising formulation of the material formamidinium lead triiodide ($FAPbI_3$) by reducing vacancy defects and augmenting the crystallinity of the film. This perovskite was chosen over methylammonium lead triiodide ($MeAPbI_3$) because it is thermally more stable, with a greater bandgap for photovoltaic efficiency. However, only the a-phase version of $FAPbI_3$ is desirable, and at lower temperatures the phase shifts to a photoinactive and unstable phase. This group has worked to overcome this issue with additives during the formulation of the perovskite layer, with demonstrated success, however crystallinity defects, specifically iodide vacancies, still remain. This study added the formate ions during the synthesis of the perovskite, filling the vacancies, improving crystallinity, and ultimately improving performance.

The device design used FTO coated glass with a compact TiO_2 blocking layer, and a mesoporous TiO_2 nanoparticle layer. The perovskite layer was added via spin coating on top of the TiO_2 np layer, followed by octyl ammonium iodide, and a Spiro-OMeTAD HTM. Gold leads were evaporated directly onto the device under a vacuum. At a certified testing center, this system demonstrated a maximum power conversion efficiency of 25.21%, with V_{oc} of 1.174 V, a J_{sc} of 26.25 mA/cm^2, and a fill factor of 81.8%. Shelf life and operational stability studies demonstrated the unencapsulated systems maintained over 80% of their efficiency, both in 20% relative humidity and at 60^oC, for over 1000 hours.

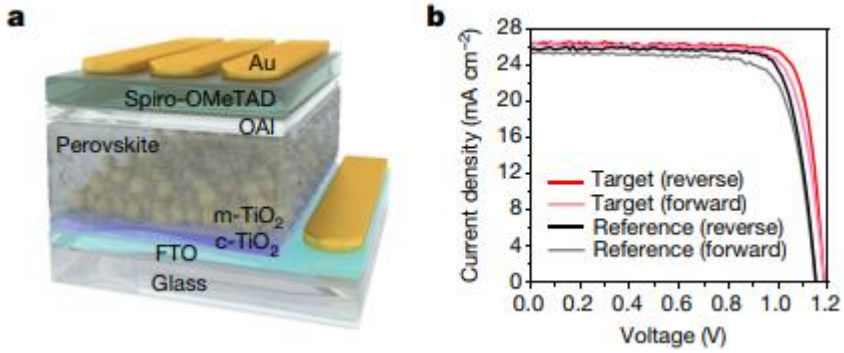

Figure 2.3. Schematic and i-V for PSC with the highest record efficiency. Image is taken from Jeong et al[76].

The OPV study was produced by Zhang et al from the Shanghai Jiao Tong University[77]. This study aimed to overcome limitations on the PCE of OPVs set by the energy levels of the donor and acceptor material while balancing the impact of morphological and electronic structure on the system performance. The team began with a donor-acceptor pair that has previously demonstrated high PCE, PM6:Y6, and blended in an additional donor and acceptor to create a cascading charge effect. The additional donor, PM 7, is miscible within the PM6 base, and possesses a slightly deeper HOMO than the PM6, allowing donations of electrons from lower energy without changing the morphology of the materials. The additional acceptor, PC71BM is compatible with the base blend of PM6:Y6 but with a slightly higher LUMO than Y6. The cascading charge creates a greater separation between the donor HOMO and acceptor LUMO, increasing the Voc of the system. Additionally, favorable direct interactions between the materials improved charge carrier transfer, which resulted in increased J_{sc}. This study showed how a bulk heterojunction OPV can leverage a quaternary blend of donors and acceptors to improve performance while managing physical and electrochemical properties.

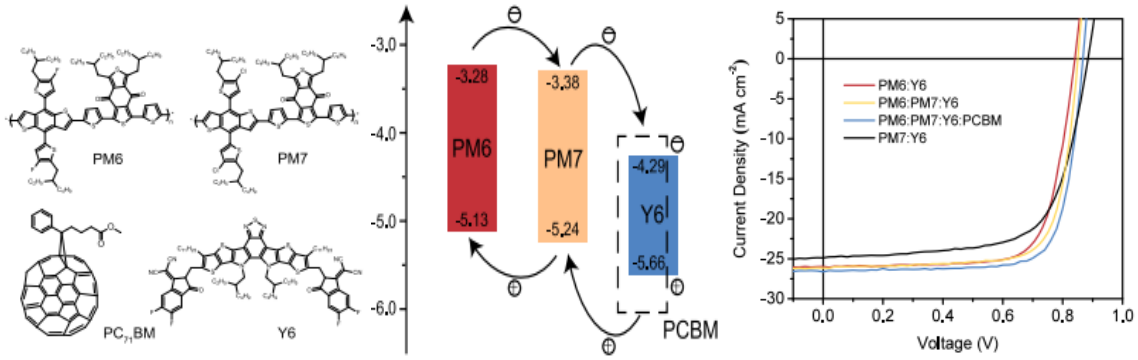

Figure 2.4. Depiction of organic molecules used within the quaternary blend, schematic of band alignment and electron flow within the device, and i-V curve of top-performing OPV. Images were taken from Zhang et al[77].

The device was composed of an ITO anode, with PEDOT: PSS serving as an ETL. The bulk heterojunction quaternary blend active layer was applied to the ETL via spin coating. The HTM applied was PFNDI-Br, with silver leads evaporated onto the device under vacuum. The device demonstrated a PCE of 18.02%, V_{oc} of .859v, J_{sc} of 26.55mA/cm^2, a fill factor of 79.23%, and maintained 81% of its performance after 1000 hours.

The DSSC study was prepared by Zhang et al. from EPFL[78]. This paper used multiple organic dyes to improve the PCE of the DSSC, recognizing the limitations single dyes impose on the overall device performance. Some dyes offer a broad spectrum of absorbance, and high photocurrent density, but low V_{oc}, while others only absorb narrowly within the blue or yellow spectrum, with low photocurrent, but high V_{oc}. When appropriately mixed, the two dyes can be synergetic, providing increases in both photocurrent and V_{oc}. This study developed an organic donor-acceptor co-sensitizers, named MS4 and MS5, using a bulky donor N-(2',4'-bis(dodecyloxy)-[1,1'-biphenyl]-4-yl)-2',4'-bis(dode- cyloxy)-N-phenyl-[1,1'-biphenyl]-4-amine(coined a Hagfeldst donor), and BTBA as an acceptor. In addition to setting a record for DSSC PCE under standard illumination, the system also demonstrated PCE over 30% under ambient light.

The device used an FTO anode, a TiO_2 blocking layer, and TiO_2 mesoporous layer. The

counter electrode was ITO with electrodeposited PEDOT: PSS. The two electrodes were stacked, and sealed, with the copper-based electrolyte added via a drilled hole. This system demonstrated a PCE of 13.5%, V_{oc} of 1.05 V, J_{sc} of 15.84 mA/cm2, and fill factor of 81.3%, while maintaining 93% of its performance after 1000 hours

In comparing these three studies using SWaP-C, the difference in size and weight between the different designs is negligible, as many of the materials and fabrication processes are common across devices. The mass of the active layer or overall thickness of the device is not distinct enough to differentiate between systems. Concerning performance, the PSC demonstrates efficiency 38% greater than the OPV and 86% greater than the DSSC and except for stability over time, out-performed the other devices in each category. The difference in current performance and the rate of increased performance observed over recent years suggest that PSC will maintain a discrete performance advantage over other emerging photovoltaics in the coming years. About cost, the comparison is more complicated as many of the materials and fabrication techniques are the same, and various applications of manufacturing advancements will reduce the price of production. In this case, though the OPV cell may have an advantage as the device does not include any TiO_2, which can be a costly component both in time and money. With regards to the impact on the environment, the OPV would be favored, as the PSC still contains lead, which would be toxic at the end of the device life cycle, and the DSSC includes a toxic copper electrolyte solution. Ultimately, based on the evaluation criteria, and the ultimate goal of reducing the cost per unit of energy produced, PSCs provide the best path forward for development.

2.6 Conclusion

While the performance of emerging photovoltaics still lags behind traditional

crystalline semiconductor systems, the rapid increase over a very short amount of time is promising. The continued investments and research for generally applied improvements, like novel HTMs, and overcoming class-specific shortfalls, like crystallinity defects in perovskites, will make the commercial application much more likely, as the price per unit energy produced will decrease. Understanding how these systems, and other emerging classes of photovoltaics, like biohybrids and multijunction hybrids, will be critical in solving the current urgent need for clean cheap renewable energy.

CHAPTER 3

Materials & Method

This chapter will introduce the primary materials used throughout the research, as well as key techniques, equipment, and procedures used. Individual chapters will also include a section on materials and methods for specific protocols and unique materials.

3.1 Photosystem 1

3.1.1 Protein Background

Photosystem I (PSI) is a membrane-bound protein found within the thylakoid stacks of plants and algae in its monomeric form, and certain cyanobacteria in its trimeric form[24]. The protein plays a key role within oxygenic photosynthesis serving as an efficient photodiode, absorbing solar energy to excite electrons from plastocyanin within the thylakoids, and transfer them to ferredoxin on the stromal side[79]. The monomeric protein is roughly 500kDA in size, is generally broken down into 14 subunits, and is predominately composed of chlorophyll arrays surrounding an electron transport chain[80-87]. The chain begins at a chlorophyll dimer called the p700 site, where the protein accepts electrons[82]. The light energy absorbed by the chlorophyll arrays is used to excite the accepted electrons by approximately 1.7 eV to p700*before the charge carrier is transported through a series of phylloquinone (An, A1), and culminating in a series of Iron-sulfur complex (F_X, F_A, F_B) with a potential difference of roughly 1.1v compared to the accepted electron[87,88]. This process occurs in roughly 1μs and depending on conditions can reach turnover rates over 20 electrons within a second[82,88].

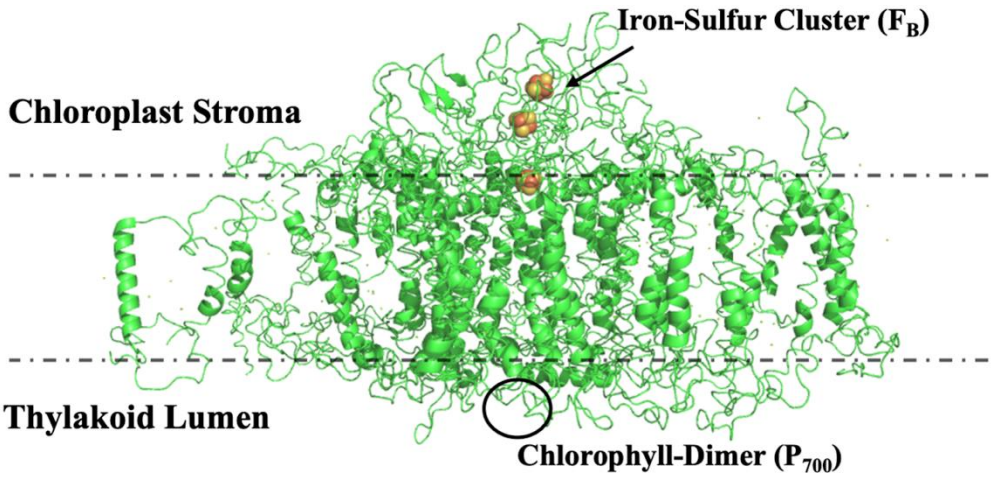

Figure 3.1. Crystal Structure of Monomeric PSI from *Spinacia oleracea*. Structure of photosystem I from *Spinacia oleracea.* The thylakoid membrane is simulated by dashed lines across the transmembrane region of PSI. (Structure taken from PDB: 2WSC)

3.1.2 Previous work

Photosystem I has been a central protein in research for years, with applications in fuel cells and photovoltaics taking advantage of the protein's efficient translation of light energy into a flow of electrons[89]. Capturing that efficiency within an engineered system is significantly more difficult, as demonstrated by the fact that biohybrid PSI-based photovoltaics have yet to demonstrate efficiency near those of crystalline silicon or other emerging photovoltaics. Research in the field of PSI-based photovoltaics has benefitted though from advances in adjacent photovoltaic work, as demonstrated by improvements in PSI-based device performance over the years.

Early research aimed to better understand the protein, its internal functions of light-harvesting and charge transfer, and the overall system structure, with some labs looking to modify the protein itself for improved use in engineered devices[28,79-93]. While some efforts looked to use the protein and chlorophyll arrays as dyes within modified biohybrid dye-sensitized solar cells, much of the early work focused on developing self-assembled

monolayers and multilayers on various electrode surfaces and evaluated the photoactivity of those monolayers within electrochemical wet cells, with the use of diffusional mediators to donate and accept electrons to and from the protein[94-118]. These surfaces included planar gold, gold leaf, heavily doped silicon, reduced graphene oxide, and others. The charge transfer between monolayers and the electrode surface was improved with various types of direct connections by first treating the electrodes with a layer that would then complex with the protein. These improvements were necessary to translate the success observed within wet cells to future solid-state devices that would not benefit from the diffused mediator. These improvements in attaching the proteins in layers to the electrode surfaces saw the efficiency of PSI based devices increase by orders of magnitude over a short time.[110]

Continued efforts for direct charge transfer of electrons to and from the electrode began entrapping the electrode within conductive polymers and hydrogels. This had the advantage over monolayers, and multilayers as the polymers and gels could mediate the charge, and more efficiently use the proteins, while providing greater physical support for the protein and allowing it to maintain its natural conformation[27,119-127]. Our lab has previously entrapped PSI within a film of electropolymerized Polyaniline on planar gold electrodes, demonstrating improved photocurrent density while using far less protein compared to self-assembled monolayers[122]. Other studies have shown PSI encapsulated within PLGA and Metal-Organic frameworks can demonstrate improved photocatalytic activity compared to solubilized proteins, while preserving the stability over time[119,124].

More studies on solid-state PSI systems are being reported, building on the success seen in other types of devices, particularly in the application of band alignment to the PSI based devices[128-131]. More care is being taken to introduce HTM and ETL that efficiently donate

or accept electrons to and from the protein[131]. The Lisdat group has demonstrated the application of complexing PSI directly with cytochrome C and attaching the protein complex directly to a high surface area ITO electrode[82,132,133]. Baker et al have entrapped PSI within a Nafion film, using an Osmium complex to scavenge holes from the protein P700 site and methyl viologen to accept electrons from the F_B site[27]. A 2017 paper by Kazemzadeh et al created a solid-state PSI based device with an FTO anode, PEDOT:PSS HTM, a vacuum deposited PSI active layer, a LiF ETL, and an evaporated Aluminum cathode, which produced an average Voc of .25v, Jsc of .960mA/cm2, fill factor of .31, and efficiency of .069%, which at the time of publication was a record for PSI based devices [134]. Our group has previously reported producing PSI based solid state devices using PANI/PSI film active layers, PSI monolayers with the redox polymer Polyviologen, and a layer-by-layer design with PEDOT: PSS and PSI on gold electrodes.[125]

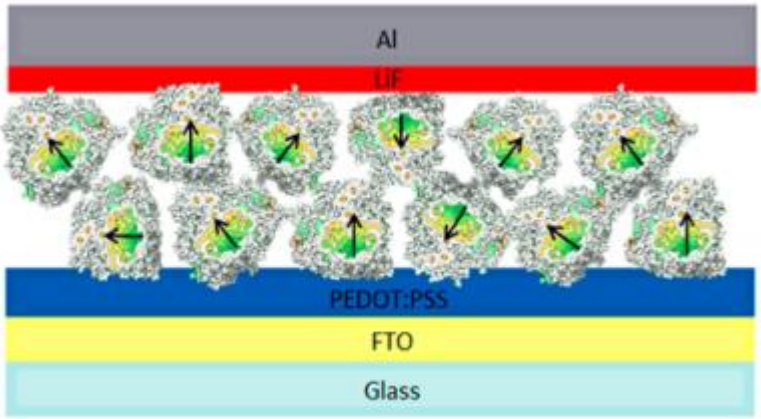

Figure 3.2 Schematic of PSI based solid-state photovoltaic with highest recorded PCE. Image taken from Kazemzadeh et al.[134]

While the performance of PSI based devices remain orders of magnitude below that of other current photovoltaics, the abundance of the protein, and urgent demand for clean renewable, and cheap energy will continue to drive research. Future efforts will continue to apply improvements from other types of devices to improve active layer stability,

increase V_{oc}, and improve charge transfer from the protein to the electrodes, driving the efficiency of the devices up, and the cost of energy produced down.

3.1.3 Extraction

The protocol used by our lab to extract PSI is adapted from the process established by Reeves, Hall and others, and has been described in detail in multiple publications[121,135-134]. Our lab chose organic baby spinach as the primary source of monomeric PSI, to minimize any chemical contamination, and maximize the concentration of protein within the leaves at harvesting. The process first works to isolate the whole thylakoid, then use protein chromatography to separate PSI from other proteins present. This process utilizes an ion affinity column (Hydroxyapatite), and two sodium buffer solutions with different ion concentrations and pH. The column buffer, with a lower concentration of ions and neutral pH, helps to activate the column, and allows the slightly charged PSI protein to cling to the column, while other materials without charges pass through the column. The second buffer, with significantly higher ionic concentration, a more acidic pH, and the surfactant Triton X-100, allows the column to release the protein for collection. The flow chart below, prepared by Dr. Kody Wolf, summarizes the process.

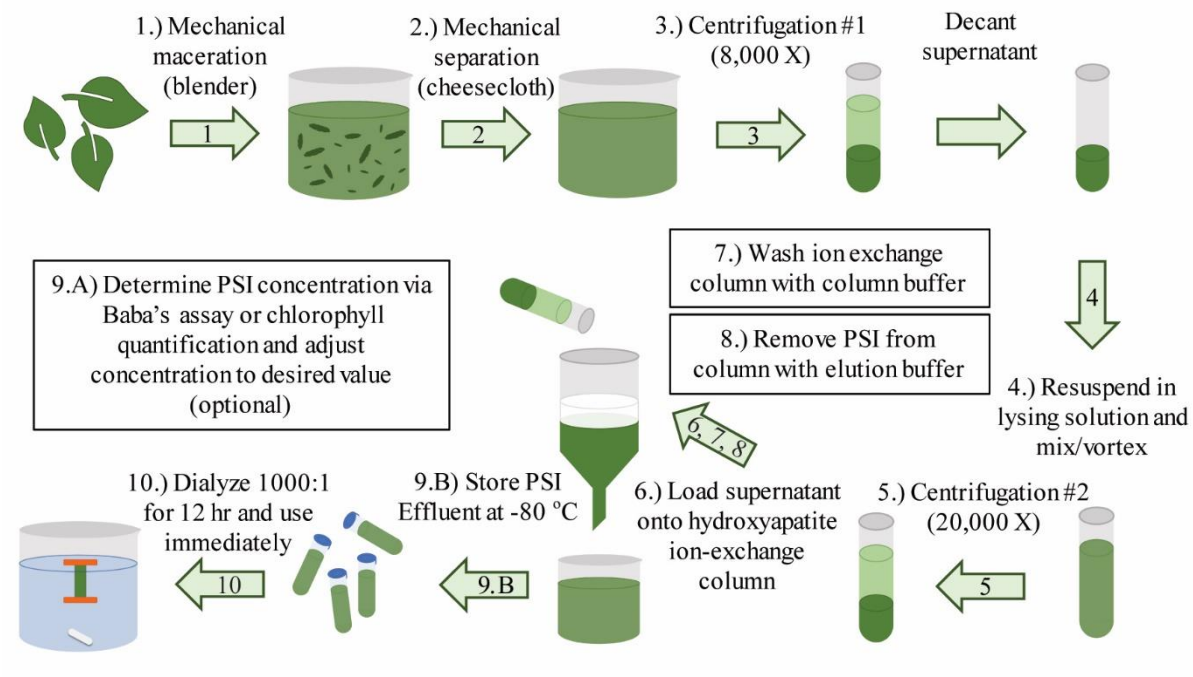

Figure 3.3. Schematic of Cliffel lab PSI extraction procedure from baby spinach as prepared by Dr. Kody Wolf.

Because of the length of the protocol, it is recommended that all solutions are prepared the day before the extraction, and stored at 4° C. Additionally, the organic baby spinach should be fresh, and can be purchased and stored at 4° C as well. The quantities for solutions prepared are sufficient for an extraction from 100-150g of spinach. Grinding medium (300ml) was prepared with DI water, Sorbitol (18.040g), Sodium Pyrophosphate (1.340g), Magnesium Chloride ($MgCl_2 \cdot 6H_2O$ .240g), and (L) Ascorbic Acid (.110g). The pH of the solution is adjusted to 6.5 with HCl. Lysing solution (100ml) was prepared with DI water, HEPES (1.192g), Sorbitol (6.012g), EDTA (.058g), Magnesium Chloride ($MgCl_2 \cdot 6H_2O$ .020g), Manganese Chloride ($MnCl_2 \cdot 4H_2O$ .020g), and Triton X-100 (1.00% w/v, 1.000g). Column Buffer (1L) is prepared with DI water, Monobasic Sodium Phosphate ($NaH_2PO_4 \cdot H_2O$, .549g), Dibasic Sodium phosphate anhydrous (Na_2HPO_4, .855g), and the solution pH was adjusted to 7.0. Elution buffer (1L) was prepared with DI water, Monobasic Sodium Phosphate ($NaH_2PO_4 \cdot H_2O$, 18.656g), Dibasic Sodium

phosphate anhydrous (Na_2HPO_4, 9.199g), Triton X-100 (.055w/v, .500g), and the solution pH was adjusted to 6.5.

The first step was to prepare the fresh baby spinach leaves by removing large stalks, veins, and other hard plant materials. These materials were discarded, while the remaining leaf material was weighed to ensure 100-150g. The leaf material was then placed in a blender, along with 200ml of grinding medium in order to fully macerate the spinach leaves. The leaves were blended until homogenous, and no large pieces of leaf remained. This step lysed the leaf cell walls, releasing the thylakoids and other leaf organelles into solution with the grinding medium. The resulting blend was then filtered through two layers of cheesecloth to separate large leaf materials that were not macerated. This process was repeated with eight layers of cheesecloth to ensure the large leaf materials were mechanically separated from the macerated leaf blend. This step required a gentle squeeze of the cheesecloth to ensure the blended solution passed through and was collected. This step produced between 150ml and 200ml of solution, and the materials collected within the cheesecloth were discarded.

The filtered solution was then divided evenly within centrifuge tubes to separate the heavier thylakoid stacks from the other leaf organelles in solution. The Allegra X-30R centrifuge was set at 4^o C, with a relative centrifugal force (RCF) of 8,000 G. Centrifuge tubes were filled approximately halfway and balanced to ensure equal weight distribution. The solution was centrifuged for one minute, creating a pellet of thylakoid stacks, and leaving the remaining organelle material within the supernatant. The solution was then aspirated, discarding the supernatant without disturbing the pellet.

The next step was to lyse the thylakoid membrane in order to release the membrane-bound proteins, including PSI. The surfactant within the lysing medium inserts itself into

the hydrophobic regions of the lipid bilayer of the thylakoids, solubilizing the lipids, while also solubilizing the membrane bound proteins by binding to their hydrophobic regions. This allows the protein to stay in solution throughout the rest of the procedure until the surfactant is removed through dialysis. In this step 2-3 ml of lysing solution was added to each centrifuge tube to resuspend the pellets. Vortexing for 30s or vigorous shaking was needed to ensure the entire pellet was resuspended.

Next, the solution was centrifuged again to separate the solubilized PSI proteins from the denser thylakoid materials. The solution of lysing medium and pellets was evenly distributed into centrifuge tubes once again. The centrifuge was set at 4^{o} C and an RCF of 20000 G. This time the solution was centrifuged for 15 minutes. At the end of this step, the solubilized PSI protein is within the supernatant, and the denser remaining cell material will form the pellet. Afterwards, we aspirated and collected the supernatant from each centrifuge tube, without disturbing the pellets, which were discarded after this step. This produced 25-30ml of dark green solution.

To prepare the Ion affinity column used to separate PSI from the other proteins within the solution, we secured an upright straight-jacketed extraction column with valve to a ring stand. Tubing was attached to the inlet and outlet nozzles to pump and recycle ice water around the column. In a separate beaker, 15g of hydroxyapatite was added, covered with column buffer, and stirred. Once the solution settled, the cloudy column buffer was removed, and the processes repeated. This step is used to both activate the hydroxyapatite, with exposure to the low ion concentration buffer, as well as remove the extra-fine particulates which may get caught within the column filter, slowing the process. After a second wash and activation, the column valve was closed, and the hydroxyapatite and column buffer mixture was poured into the column. The hydroxyapatite will settle and

separate from the column buffer within the column. We then removed the excess column buffer, leaving only the enough to cover the top of the column, ensuring the ice water was being properly cycled around the column. This column takes advantage of the net negative ionic charge of the solubilized PSI and hydrostatic interactions with the hydroxyapatite particles within the column[143]. The net negative surface charge of the PSI is based on the surface amino acid residues and is dependent on both the pH and pKa of the solution. Akerlund et al reported the isoelectric point of solubilized PSI at 4.4, meaning the protein should be negatively charged in the neutral column buffer, and attracted to the positive hydroxyapatite particles within the column[143]. While the column valve was closed, we slowly pipetted the dark green supernatant solution onto the inner wall of the column 1-3cm above the hydroxyapatite, taking care not to disrupt the packed powder within the column. Once all of the solution was loaded, a waste collection beaker was placed beneath the column valve to allow the buffer to run off and the PSI solution to cover the hydroxyapatite column. Next, the valve was closed once again when the meniscus of the fluid was just above the hydroxyapatite within the column, which was stained with the dark green solution.

The next step was to wash the column with buffer as a means of removing the other materials that may have been in solution with PSI. This includes weakly bound species, positively charged proteins, lipids, and other complexes. With the column valve closed, the column buffer was added in the same manner as the PSI solution, taking care not to disturb the hydroxyapatite. The green effluent was collected within a waste beaker. While the effluent of the washing step is green, the column also maintained its green appearance. More column buffer was added in the same manner described above to ensure the meniscus of the fluid did not reach the top of the hydroxyapatite. This step continued until

the effluent collected was clear. This was a slow step and took hours to complete but was critical to ensuring isolation of the correct protein.

Once the effluent of the washing step was clear, and the level of column buffer was reduced where the meniscus of the fluid was at the top of the powder within the column, the elution buffer was added in the same manner as described above. The elution buffer introduces a higher concentration of ions, a lower pH, and additional surfactant, all of which work together to separate the PSI from the hydroxyapatite. The initial effluent was collected in a waste beaker until a it began to appear dark green. At that point, a collection beaker beneath the column collected the dark green solution. We observed a dark band move downward on the powder column, leaving white hydroxyapatite above it. This is an indicator of the progress of elution, as it continued moving, with additional elution buffer, until the dark band has reached the bottom of the column. The total collected PSI solution was typically 150ml. The PSI solution was then quantified, and stored in 1ml aliquots at -80^{o} C.

3.1.4 Quantification

The concentration of PSI in the solution collected is unique to each extraction, though is typically between 1-3mg PSI/ml of solution. Determining the actual concentration of PSI within the stored aliquots allows for standardization and repeatability for experiments. Our group usually uses an assay first described by Baba et al to quantify the p700 reaction centers within a solution using Ultraviolet-Visible spectrum spectroscopy (UV-Vis)[138]. The process compares the absorption spectrum of two samples, with equal amounts of PSI solution, where one sample includes an oxidizing agent, and the other a reducing agent. Assuming that all p700 sights react fully, the two absorbance spectrum can be compared to

determine the concentration of p700 in the original solution.

The Baba assay requires a number of solutions to be prepared prior to attempting quantification. The Baba assay buffer (100ml) is composed of DI water, Tricine (.896g), Sorbitol (1.822g), Sodium Chloride (NaCl .059g), and Triton (.050g). The oxidation solution (10ml) is prepared with DI water, and Ferricyanide (3.293g). The reduction solution (1ml) is prepared with DI water, Sodium Ascorbate (.099g), and Dithiothreitol (.001g).

To conduct the assay, the UV-VIS system was first set to a baseline, using a cuvette filled with only assay buffer(3ml). Next an absorbance spectrum was taken with two cuvettes, filled with assay buffer(2.775ml), elution buffer(.1ml), and either oxidation solution (.125ml) or reduction solution (.005 ml and .120ml DI water). These spectra were nearly identical, and their difference served as a reference for the assay. Next, two additional cuvettes were prepared with assay buffer (1.875ml), PSI solution (.5ml), and either oxidation solution (.625ml) or reduction solution (.025ml and .6ml DI water). After mixing, these cuvettes were allowed to settle for at least 15 minutes to allow the oxidation or reduction reaction at the p700 sight happen fully. During this process, a divergent color change was observed in the two cuvettes. Next, absorbance spectra from both cuvettes in the range of 750nm-650nm were collected. Using the recorded absorbance spectra, the values of the baseline scan were subtracted from the values of the PSI scans. The difference of the spectra will show a peak absorbance value near 700nm. Using the peak absorbance value, the absorbance value at the isosbestic point for PSI (725nm), and the extinction coefficient of P700 ($64mM^{-1}cm^{-1}$), the concentration of PSI within the cuvettes was calculated as described below, and used to quantify the concentration of PSI within the collected solution:

$$C_{PSI,\ sample\ cuvette}(mM) = \frac{[A_{peak} - A_{isobestic}]}{64\ (mM^{-1}\ cm^{-1}) \times L\ (cm)} \qquad \text{Eq. 1}$$

$C_{PSI,\ sample\ cuvette}$ = PSI Concentration in the Sample Cuvette (mM)
A_{peak} = Peak absorbance from the differential spectrum (unitless)
$A_{isobestic}$ = Isosbestic point absorbance (unitless)
$L\ (cm)$ = Pathlength in the cuvette (cm), typically 1 cm

3.2 Polyaniline

3.2.1 Background

Among the family of organic conductive polymers, Polyaniline (PANI) stands out both as one of the most studied, and most promising materials. While it was initially discovered in the late 19th century, and known as aniline black, it was roughly 80 years later that its potential applications were first theorized, and over the last thirty years, PANI has been a staple of electrochemical research. [144] While it has not demonstrated the highest conductive properties, PANI is preferred amongst organic conductive polymers due to its high stability, ease of synthesis, and the ease of control over electroactivity. Additionally, the aniline monomer is relatively cheap, and readily available.[145] These attributes allow researchers to incorporate PANI into novel electrical devices, like sensors, photovoltaic cells, and batteries, generally as a charge transport layer, improving the electroactivity, or connecting other aspects of the devices.

Aniline is composed of a benzene ring functionalized with an amino group. When oxidized, the resulting polymer can take on different structures, and morphologies, depending on the level of oxidation and most notably marked by the color (leucoemeraldine is usually white or colorless, emeraldine is a green/blue, and nigraniline can be brown).[67,146] Emeraldine is produced when polymerized within an acidic

environment and is the only form that is conductive based on a mix of oxidation states. The electroactive properties of PANI are based on the delocalized electrons within the aromatic repeating unit backbone, providing an electrical pathway for charge carriers. When emeraldine is fully reduced, it becomes leucoemeraldine, and when fully oxidized, pernigraniline All carbons within the polymer are SP^2 hybridized with electrons in orthogonal pi-bonds contributing to conduction.[145] In theory, this should make the substance a semimetal like graphene, however, because the polymer chain is in one direction it allows for an energetically favorable relaxation to occur, leading a separation within the SP^2 band between the filled and unfilled states.[162] The nitrogen atoms between the phenyl rings allow for different oxidation states, which introduce different electrochemical properties. Undoped PANI has demonstrated conductivity of 6.28×10^{-9} S/m, though doping and changes in morphology have been shown to increase that value by multiple orders of magnitude.[149]

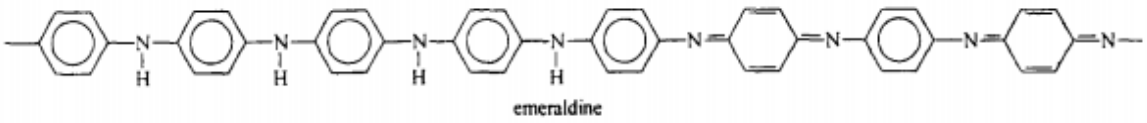

Figure 3.4. Emeraldine conformation of Polyaniline. Image taken from Feast et al [67]

Beyond PANI, the other two most prominent conductive polymers in research are poly(3,4-ethylenedioxythiophene)(PEDOT) and polypyrrole (PPy). All three polymers leverage delocalized electrons within the conjugated rings of the monomer to produce inherent conductivity in an oxidized state. PPy is the most similar to PANI by composition with a nitrogen hetero-atom incorporated within the aromatic ring and demonstrating similar conductive properties. The nitrogen hetero-atom within PANI is external to the aromatic rings. PEDOT incorporates sulfur and oxygen within a double-ringed structure. All three polymers have rigid backbones due to the highly conjugated chains, which result

in crystalline fibers with high tensile strength and low ductility. All three have similar electrochemical and physical properties, and in many cases are interchangeable. Polypyrrole has historically been used in commercial settings due to its long-term stability, though its applications were limited because of its poor solubility. PEDOT was developed in the late 1980s as an antistatic coating and is currently used in photovoltaic devices due to its transparency, high conductivity, and good stability in humid air. It is usually doped, with polystyrene sulfonate (PSS) for improved processability. [159] Some studies have compared these different polymers for specific applications, and while the information is helpful, the unique circumstances may limit how well the results translate to other projects. A study in 2010 used a rigid sulfonated poly(amic acid) as a template to directly compare these three polymers, across multiple parameters, including reaction time, conductivity, and thermal stability. In this study PANI had the fastest reaction time of the three and the highest conductivity by several order of magnitude. PEDOT had the slowest reaction time, and lowest conductivity, however, annealing the polymer increased the conductivity five-fold, demonstrating greater thermal stability than the PANI construct, which lost conductivity at higher temperatures. PPy was consistently recorded between the other two in each metric.[160] This aligns with the chemical formulas of the polymer, where PANI has a greater number of delocalized electrons within its aromatic rings, which may impact its conductivity, and PEDOT has the most rigid backbone, which would provide the greatest mechanical strength. A 2013 study made a similar comparison but coated the polymers on hollow sulfur nanoparticles for use in lithium sulfur batteries. In this study PEDOT was the most conductive, had the highest specific capacitance, and highest retention, whereas the PANI performed the worst in all three fields.[161] Whether this result stems from the physical properties of the polymers, the shape of the substrates, or the

chemical make-up of the hollow spheres is unclear, however the study demonstrates how the best conducting polymer for a study may have more to do with the specific application than inherent properties of the polymer. This may explain why PANI is more widely used as it has the longest history in literature, and more groups are familiar with protocols for the polymer.

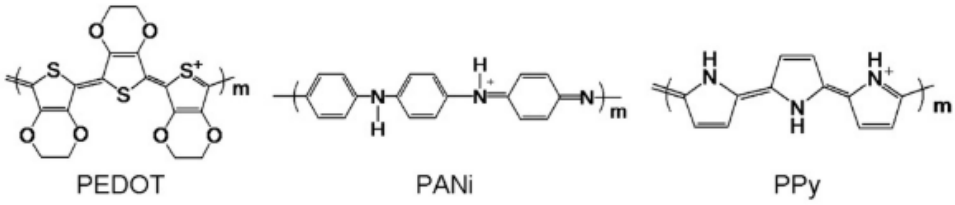

Figure 3.5 Examples of the conductive polymers PEDOT, PANI, and PPy. Image Taken from Somboonsub et al.[160]

In addition to conductivity, PANI has also demonstrated inherent pseudocapacitive behavior. During cyclic voltammetry, three redox peaks highlight transitions between different forms of the polymer, and the appearance of these peaks in a high background current indicate capacitive performance.[144] Pseudocapacitance differs from electric double layer capacitance in that storage and discharge are not based on a separation of charge, and the interface between the electrode and electrolyte. Instead, pseudocapacitance, as observed in conductive polymers, is the result of fast reversible faradic REDOX reactions that involve the entire material. This property allows for greater energy density and capacitance.[150] Literature has shown PANI electrodes can charge and discharge in the potential window of .8-1.0 V, which is promising for novel supercapacitors, but may negatively impact other applications.[144] Improving the capacitance of PANI has predominantly been through doping and changing the morphology. When PANI is developed in long thin nanofibers, or with high porosity, it demonstrates a higher specific capacitance. [144] Unfortunately, devices made with PANI-based electrodes have

demonstrated structural deterioration, like swelling and shrinking, during cycling, resulting in poor cycling stability.[151]

Polyaniline is generally polymerized in two methods: chemical oxidation and electropolymerization. Aniline salts are generally oxidized chemically in acidic aqueous solutions, with strong oxidizers, like ammonium peroxydisulfate, or I_2. These reactions can also create side products of branched oligomers, which reduce the electroactivity of the polymer.[67,146] These side reactions can be controlled thermodynamically and with the pH of the solution. Electropolymerization of PANI uses a current to drive oxidation of the aniline monomers in an acidic solution, growing the polymer out from the surface of the electrode.[144,147] The mechanism for polymerization is generally accepted as an E(CE)n process with forming radical cations from aniline monomers being the rate-determining step[163]. The growth of the polymer chain has been demonstrated to be self-catalyzing, showing that the rate of formation increases with the amount of polymer formed[163]. Changing the electropolymerization conditions, like the substrate, voltage, current, and scan rate, can result in different morphologies of the PANI, as well as variance in measured electrochemical properties.[148] Chemical oxidation provides better flexibility for nucleation and growth during polymerization, while electropolymerization methods allow PANI to be grown in films directly on novel substrates, adding a conductive layer to the surface. Both are advantageous in the development of novel electrochemical systems, including photovoltaics.

The processability of PANI is a key aspect of the promise for future advancements with the material. Protonated polyaniline is insoluble in organic solvents, which makes it difficult to use traditional polymer processes to produce pure PANI fibers, and those that are produced are generally fragile[163]. There has been success processing PANI with

copolymers that add physical strength, however, as the fraction of insulating polymers increases, the electrochemical properties of the combined polymer decrease[164-166].

Electrospinning has been a method of creating high surface area devices from conductive nanofibers, though many studies have relied on a copolymer due to the difficulty in electrospinning pure PANI. Others used carbon based grounding surface, building a carbon composite surface with the PANI nanofibers. In one study the electrospun PANI nanowebs produced in aqueous electrolytic solution had a measured capacitance of 267 F/g, current density of .35A/g, and retained 86% capacitance over 100 cycles, all of which were improvements on PANI powder alone (208 F/g, 48%).[145] This demonstrates the value of the electrospinning process in maximizing the electrochemical properties of PANI. A 2019 study combined Solgel and electrospinning to produce novel flexible carbon nanofibers(CNFs). PANI was then grown on the CNF via chemical oxidation over various lengths of time. The PANI coating improved the electrochemical performance of the CNF, with the greatest improvements observed with the longest polymerization time. SEM was used to confirm a uniform morphology of PANI on the CNF. Mechanical testing showed the PANI-CNF demonstrated greater tensile strength than traditional CNF, though less strength than the solgel-electrospun CNF without PANI. This method produced electrodes with a capacitance of 234 F/g, retention of roughly 90% of its capacitance after 1000 cycles, energy density of 32 Whr/kg and power density of 500W/kg.[151] This study utilize the PANI as a coating and maximized its impact by growing the polymer directly on the CNF, maximizing coverage and surface area of the PANI.

Doping, another method of improving the electrochemical properties of PANI, introduces another substance, usually ionic, during chemical oxidation that can modify the polymer with a specific function for a particular application. Doping in conductive polymers is somewhat different than in semiconductors as the process creates a charge island within the gap produced in the SP^2 band and excludes doping limits from simple statistics or calculations. In general doping levels are less than one dopant per polymer unit.[162] Metal ions are able to bond with secondary amine groups, and the anionic portion of the dopant will generally associate with protonated polymer to produce salts. A 2017 study evaluated PANI nanorods doped with sulfuric acid at various molar ratios.[153] The highest ratio of dopant to PANI produced the best electrochemical results, conductivity of 6.65 S/CM, specific capacitance of 449.1 F/g at 1A/g, and retention of 75.15% after 1000 cycles.[153] A 2018 study used a LiCl dopant to create PANI-LiCl nanotubes, and observe their individual capacitance, after initial studies showed the material had a conductivity of 25 S/cm, which represents a drastic improvement.[152]

3.2.2 Electropolymerization

Electropolymerization of polyaniline was conducted using protocols described in previous published works and will be further described within later chapters.[120,122] In summary, the process is conducted using a CH Instruments 660A electrochemical workstation three-electrode setup, with Ag/AgCl (saturated KCl) reference electrodes, and a platinum mesh counter electrode. The polymerization solution is DI water, 1M aniline solution, hydrochloric acid (HCl, .941M) and phosphate buffer. The hydrochloric acid serves both to lower the pH of the electropolymerization solution, as the reaction requires

an acidic solution, and provide the chloride ions necessary to dope the emeraldine formed in the process. Polyaniline is formed on the working electrode of choice using either cyclic voltammetry or potentiostatic deposition. Using cyclic voltammetry, the potential was cycled between -.155v and 1.2v compared to the Ag/AgCl (Sat'd KCl) reference. The scan rate and number of cycles are determined by the individual experiment. For potentiostatic deposition, the working electrode was held at 1.2v, with the length of deposition dependent on the experiment.

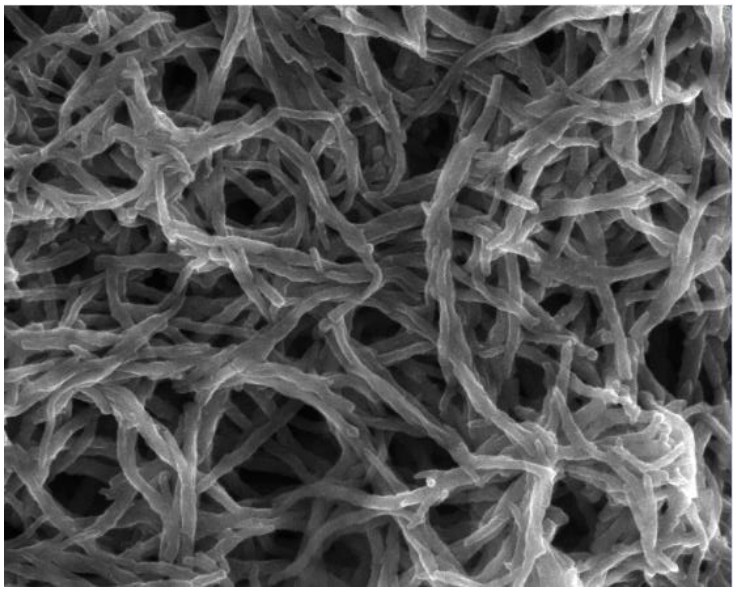

Figure 3.6 SEM of PANI fibers electropolymerized on CP electrode

This research leveraged electropolymerization as the primary means of producing PANI films. HCl was chosen as both the dopant, and agent to reduce the pH of the aqueous solution. The choice in dopant impacts the polymerization rate, morphology, and electrochemical properties of the polymer formed[163]. The Cl- ion was showed to produce smaller diameter fibrils, higher polymerization rates, and less branching of fibrils than other small counter ions, though the reduced branching may account for the decreased conductivity compared to some oxyacid[163]. Studies by Desilvestro and Scheifele have also

showed the morphology of the polymer shifts in different stages electropolymerization[167]. They suggest an induction period produces an initial dense layer of polymer with a globular morphology. These amorphous, and low surface area deposits demonstrate low conductivity, which is reflected in the reduce current observed during the polymerization. From there, polymerization proceeds from the globules into fibrils of roughly uniform diameter. The fiber continue to grow at the ends with minimal thickening of diameter, increasing the available surface area, and conductivity of the material. This is also demonstrated in the graph of polymerization, as the magnitude of current continues to increase as polymerization times continue. In contrast, graphing electropolymerization with cyclic voltammetry shows the initial sweep in the positive direction with minimal change in current magnitude until a steep change near .500v. With each cycle, the magnitudes of the peaks increase, suggesting an increase in conductivity of the polymer(Figure 3.7). Additionally, the oxidative peak shifts into more positive values with each cycle, suggesting a change in the conformation of the polymer between conductive and non-conductive states. This shift becomes less obvious in later cycles, suggesting that the confirmation change does not impact all of the deposited polymer uniformly, and an increased proportion of the polymer is remaining stable.

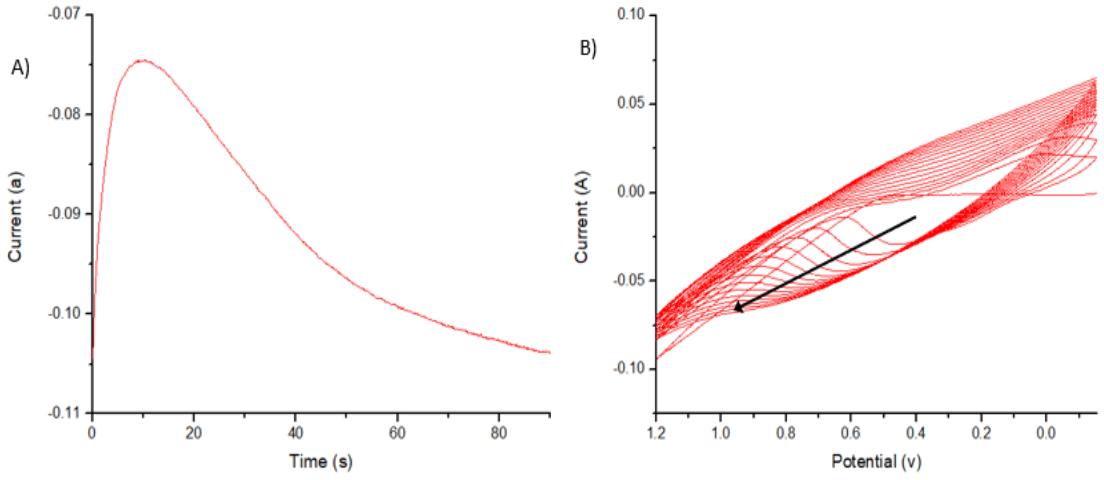

Figure 3.7 Electropolymerization of PANI films on carbon paper via (A) Potentiostatic and (B) Potentiodynamic methods

3.3 Carbon Paper

3.3.1 Background

Commercially available carbon paper is a common material used within a variety of electronics, including fuel cells, redox flow batteries, sensors, and capacitors[168]. The physical and electrochemical properties are consistent and well documented, which allows for many applications in research. The material is traditionally composed of polyacrylonitrile fibers, spun into a yarn, arrayed (organized or randomly) into sheets with a resin, and carbonized with heat and pressure[168-170]. The resulting material demonstrates high surface area, long and connected conductive fibers, low resistance, and a carbon surface that can be readily modified as required. Carbon paper demonstrates high mechanical strength, and scalability with a low cost compared to other electrode materials like precious metals or silicon wafers. Due to its application within fuel cells, and its role as a gas diffusion layer, the material is often coated with a 5-10% PTFE coating to make the material more hydrophobic. Later chapters will discuss the various methods of removing this layer, increasing the electroactivity of the material by increasing the electroactive surface area, improving electroactivity by intercalating polyatomic ions, introducing radicals to the carbon paper surface, and even shifting the work function of the material[169,171,172].

Multiple versions of Toray carbon paper were available for use within this research, including TGP-H-30, TGP-H-60, and TGP-H-120, in multiple size sheets. The primary differences between the three are the thickness, porosity, and density, with TGP-H-30 being the thinnest with the greatest porosity, and TGP-H-120 being the thickest. Additionally, molded graphite laminate is a similar material derived from petroleum and

pressed into high surface area sheets with features comparable to carbon paper, both presenting predominately sp3 hybridized carbons at the surface. During this research, all four materials were evaluated, though to standardize reported results, TGP-H-60 was the primary material applied. The manufacturer reports a thickness of .19mm, density of .44g/cm^3, and resistance of 5.8mΩcm in plane.

The high surface area of the electrodes are ideal for applications needing increased loading within a small geometric area, and especially in conjunction with polymer films. A 2008 paper by Kuwahara et al modified carbon paper electrodes by electropolymerizing a film of the conductive polymer 3-methylthiopene and thiopene-3-acetic acid for use in a glucose fuel cell. Glucose oxidase was covalently immobilized on the electrode surface, which resulted in greater catalytic activity, and a higher rate of electron transfer[173]. A 2011 paper by Yuan et al reported an improvement in biosensors, with greater sensitivity and a wider range of detection by loading the detector compound, tyrosinase, on the high surface area carbon paper electrode, rather than the standard screen printed carbon paste electrodes[169]. The applications within this research focused on the high surface area of the carbon paper electrode as a replacement for planar and evaporated metal electrodes within biohybrid photovoltaics.

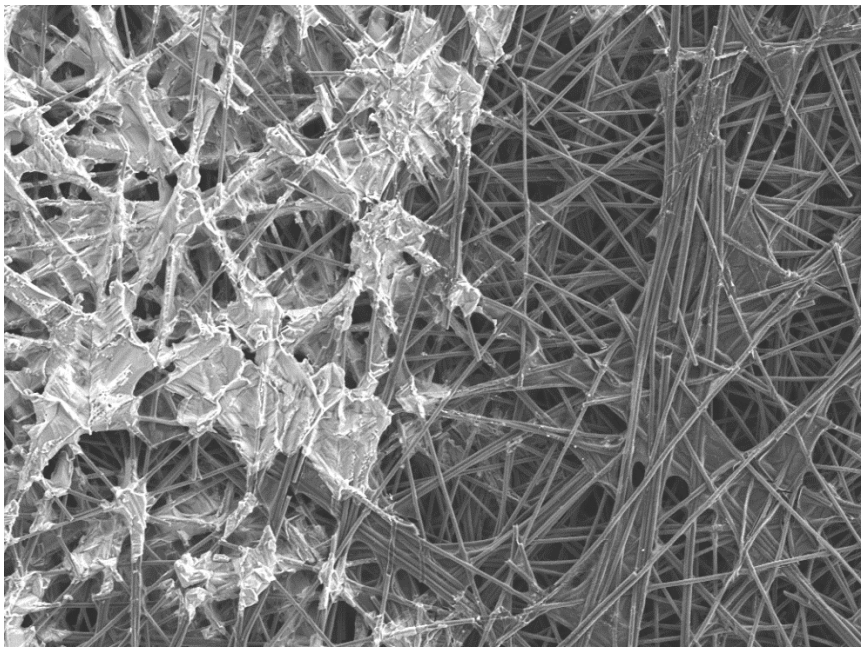

Figure 3.8 SEM image of PEDOT:PSS electropolymerized on CP electrode.

3.3.2 Electrode Preparation

Preparation of the various carbon paper electrodes is described in later chapters in more detail and are specific to the individual experiments. In summary, the carbon paper is pre-treated to remove the hydrophobic PTFE layer, using flame or a 15 min bath within 1M H_2SO_4. The electrodes are then cut to an appropriate size (3cm x 2cm or 2cm x 1cm). Some electrodes were masked with non-conductive adhesive to limit exposed surface area to a circular area or .71cm^2 or 1cm^2, depending on the experiment application. Due to the damage caused by the workstation electrode clips to the CP electrodes, conductive tags of either copper tape or carbon tape were added to the electrodes.

3.4 Other Materials

Indium doped tin oxide coated glass slide, rectangular, 30-60 Ω (Sigma Aldrich); Carbon Conductive tape, double coated, 12mm (Ted Pella, Inc.); 3M Copper conductive tape, 6.3mm (Ted Pella, inc); N,N-Dimethyl formamide (DMF, Fischer Scientific); Chloroform (Sigma Aldrich); Aniline (Sigma Aldrich); Titanium(IV) oxide, anatase, nano powder, <25nm particle size (Sigma Aldrich);Titanium (III) chloride, 20%w/v solution in 2N Hydrochloric acid (Acros Organics);Camphor-10-sulfonic acid(Aldrich); 4,4-Dipyridyl (Aldrich); Ethylene glycol (Sigma Aldrich);Poly(ethylene oxide), Mv 100,000(Aldrich); 1,10-Dibromodecane (Aldrich);Polyaniline (emeraldine salt), MW>15,000(Aldrich);Triton X-100(Sigma); Titanium(IV) chloride (Aldrich); Tracecert Iron standard for ICP (Sigma Aldrich); Hydroxyl Apatite, fast flow (EMD Milipore Corp); Water was deionized (18MW-cm) by an in-house purification system (Barnstead Nanopure, Thermo scientific, Waltham, MA)

3.5 Electrochemical Techniques

Application of electrochemistry was central to this research as a number of electrochemical techniques were used to both fabricate and characterize materials used throughout different experiments. Most techniques leveraged the CH Instruments 660A workstation with associate software, and a three-electrode setup. The reference electrode was usually silver/silver chloride (Ag/AgCl, Saturated KCl), with a platinum mesh counter electrode. This section serves to introduce a number of the techniques used regularly throughout the research, though more thorough descriptions can be found in later chapters.

3.5.1 Cyclic Voltammetry

Cyclic voltammetry is a powerful tool used both for characterization and fabrication. The technique is executed within an electrochemical workstation typically within a three-electrode set-up, with a reference, and counter electrode. The processes continuously shifts the potential of the working electrode between two limits, at a fixed scan rate, and records the resulting current[174]. This technique can provide critical information about the electrochemical processes occurring on the electrode surface and within the electrochemical wet cell. Non-faradaic current is generally observed within the background of the system and does not indicate a redox reaction. This current can be impacted by the concentration of electrolytes within the solution, the CV scan rate, and the capacitance of the working electrode. Non-faradaic current measurements at different scan rates is used in this research as a tool to determine the scaling factor difference between electrodes of the same material, but different sizes[174]. Faradaic current reflects a redox reaction within the system and is recorded within the CV graph as a peak. The shape of the CV graph is defined by the faradaic peaks, with different qualities of the peaks providing insight on the chemical reactions within the system. The number of peaks can reflect the number of electrons transferred within the system, while symmetry of peaks can be used to determine if a reaction is reversible, quasi reversible, or irreversible. The magnitude of peaks can reflect the surface area of the electrode, as well as the scan rate, and the onset of peaks can be used to determine the redox potential of the system[174]. In this research the faradaic current peaks observed in CV were used to characterize the blocking layer on ITO electrodes, as well as the redox potential of a synthesized redox polymer.

Lastly, CV was used to provide potentiodynamic electropolymerization of conductive polymers directly onto electrodes. The layered growth of the polymer can be observed as the graph expands with each cycle, shifting the onset of the anodic peak. While there a many more applications associated with cyclic voltammetry, these were the tools utilized within this research effort.

3.5.2 Amperometric i-t curves/Photochronoamperometry

Photochronoamperometry (PCA) was used to measure photocurrent of the designed systems. This is an important metric to demonstrate performance and calculate system efficiency. The technique measures the current of the working electrode over time, at a constant potential, while the system is held in darkness, exposed to light, and held in darkness again. The difference between the current observed while illuminated and the current observed in the dark represents the photocurrent of the system (*i*, Amps). Photocurrent density (*J*, Acm^{-2}) is calculated when the observed photocurrent is divided by the known area of the system. The direction of the change in observed current when illuminated is described as either cathodic (positive), or anodic (negative), and is associated with the work function of the electrode materials within the system. The light source is generally a 100mW white light, meant to represent the energy from the sun experienced at ground level, and is held at a fixed distance from the system. Prior to measuring the photocurrent, it is critical to measure the open circuit potential of the system, a point of equilibrium where no flow of electrons is observed. This is the potential set during the PCA, to ensure the performance is not biased electrochemically. The high surface area of the carbon paper electrodes often take longer to reach equilibrium and

establish the open circuit potential. This can produce a charging period during PCA prior to the current leveling out.

When exposed to light, PSI drives electrons from the p700 site to the FB site, creating a flow of electrons, or current within the system. For electrochemical wet cells, within a three-electrode set-up, the current is based on diffusion of charge carriers within the system, donating electrons to the p700 site, and accepting electrons from the FB site. The process often uses a high concentration electrolyte, like 1M KCl, as increased concentration of electrolytes reduces non-faradaic noise within the system. Additionally, diffusional mediators, like the Sodium Ascorbate and 2,6-Dichlorophenolindophenol (DCPIP), are added to the system and are electrochemically aligned to act as donors and acceptors to PSI. This can increase the photocurrent by improving the efficiency of the flow of electrons within the system. The shape of the PCA within the electrochemical wet cell often includes an immediate spike in current that immediately begins to drop off and level out to a steady state. The behavior is indicative of a Cottrellian response where the photocurrent is based on diffusion[174]. The initial spike in current at illumination reflects the immediate conversion of electrons at the working electrode surface, while the decay demonstrates a reliance on diffusion to replenish the mediator species for continued conversion. Prior studies have demonstrated that conducting PCA with stirring allows the mediator species to be readily replaced at the protein, and the peak current sustained throughout illumination[175]. In systems where the proteins are entrapped within conductive polymers, the shape of current response is different, slightly building to a steady state as the polymer shuttles electrons to and from the proteins based on its conductivity, and not diffusion.

3.5.3 Electrochemically Active Surface Area Scaling Factor

Much of the early research in this effort focuses on high surface area electrodes, including how to increase the surface area of CP electrodes through pretreatment, the impact of scaling high surface area electrodes, and comparing the performance of high surface area electrodes with planar electrodes of the same material and geometric size. This is made possible by calculating the electrochemically active surface area (ECSA) of the different electrodes. This process uses cyclic voltammetry at multiple scan rates and recording steady current values at potentials not impacted by reduction or oxidation. These flat current values represent charging or capacitance current, i_c, and have a linear relationship with the scan rate of the CV,ν, where the product of the material double layer capacitance, C_{dl}, and the ECSA, A, are the slope[174]. Leveraging this relationship and plotting the scan rate versus the charging current for different electrodes of the same material, the slopes of the two lines can be used to calculate the scaling factor of ECSA between the two electrodes.

3.5.4 Electrical Impedance Spectroscopy

Electrical impedance spectroscopy is a technique that introduces alternating signals at multiple frequencies over time to observe the electrochemical response of the cell. The dielectric response of the cell is recorded as impedance and can be used to model impedance dependent qualities of the system like resistance and capacitance[176]. The results are general reported in a Nyquist plot, where the real and imaginary parts of impedance are graphed at different frequencies, and Bode Plots, where the log of the absolute value of

impedance is graphed with the log of frequency[176]. Both plots can be used to interpret faradaic impedance characteristics by modeling an equivalent circuit and fitting the data. While the values obtained through this method are effective in describing key features of the system, it is still an approximation and is best suited to highlight trends in multiple systems.

Individual protocols used will be described in later chapters, but in general, EIS was conducted using the CHI 660A Potentiostat workstation and accompanying software in a three electrode set-up, with a platinum mesh counter electrode, and Ag/AgCl (sat'd KCl) reference electrode. The initial potential was set to either the open circuit potential of the working electrode within the system or the $E_{1/2}$ of the diffusional redox pair within the solution. EC Lab V10.40 was used to optimally fit the Randles circuit model to the impedance data (Figure 3.9). The resulting computational values for solution resistance, charge transfer resistance, and double layer capacitance were used to compare properties of different electrodes.

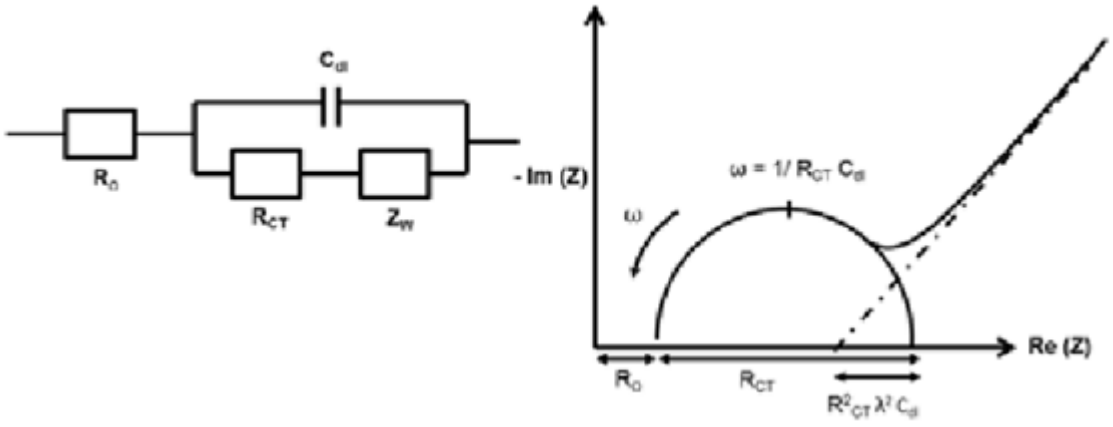

Figure 3.9 Schematic of Randles circuit, to model the impedance behavior of the working electrode within a three electrode set-up, and representative Nyquist plot. Image taken from Sekar et al. [177]

3.5.5 Linear Sweep Voltammetry

A key technique in determining the performance of a solid state photovoltaic cell is linear sweep voltammetry. This method measures the current at the working electrode as the potential is continuously shifted in a more positive or negative direction. This provides key statistics like the open circuit potential, V_{oc}, the potential where current is zero, and the short circuit current density, J_{sc}, which is the largest current that can be drawn from the cell and is measured where potential is zero. Additionally, the curve of the linear sweep voltammetry graph shows the maximum power point, the value where the product of current and potential are greatest. Efficiency of the cell, h, is derived from the product of current and potential at the maximum power point, divided by the power from the light source. Using the V_{oc}, J_{sc}, and the values of potential and photocurrent at the maximum power point, you are able determine the fill factor of the cell(Figure 3.10).

The technique uses a standard CHI 660 potentiostat workstation with associated software. The anode of the solid-state device is attached to the working electrode lead, and the cathode attached to the counter electrode lead. The reference electrode lead is attached to the counter electrode lead, ensuring the potential measured is the potential difference between the cathode and anode of the solid state device. In this research, the technique is run in either a negative or positive direction between -.5v and .5v, at a typically slow scan rate (100mv/s), both in the dark and under illumination.

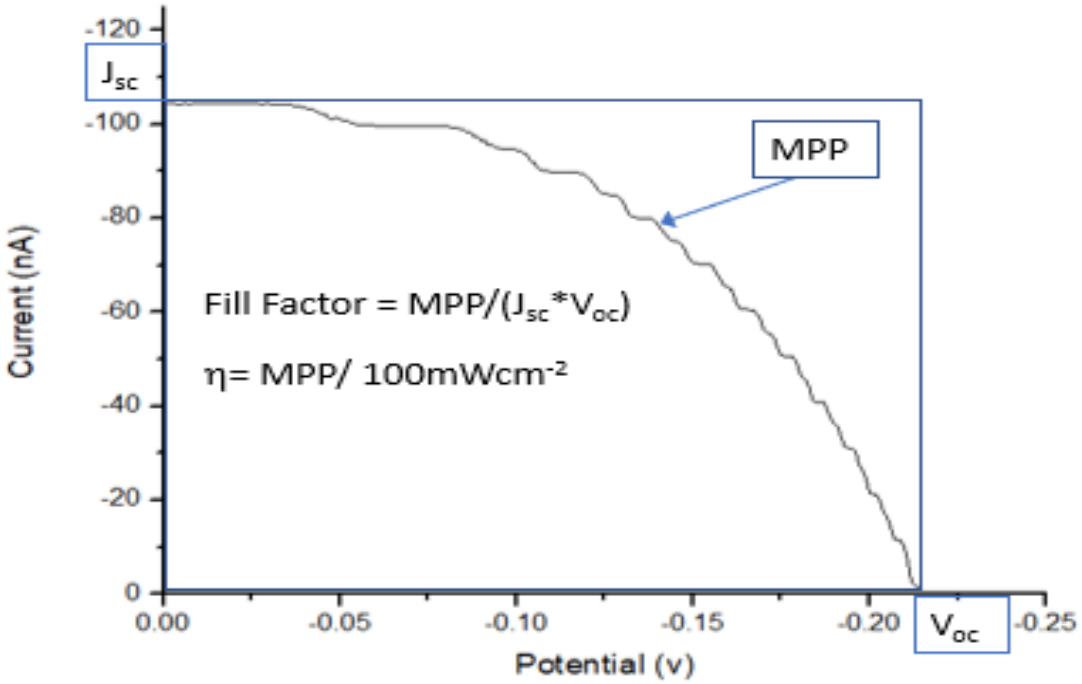

Figure 3.10 Representative i-V curve produce from LSV showing J_{sc}, V_{oc}, MPP, and the equations to find both fill factor and PCE

CHAPTER 4

Applications of Carbon Paper Electrodes in Biohybrid Photovoltaics

This chapter explores the application of Carbon Paper Electrodes (CPE) as the substrate for a PSI based photochemical electric cell. This work builds upon previous efforts within our group which used allotropes of carbon as the substrate for PSI based systems, as well as research that used electropolymerization of polyaniline to entrap PSI within an active layer directly onto the substrate. These efforts aimed to demonstrate the feasibility of adding a low cost, scalable, and high surface area substrates like carbon paper to PSI based systems and evaluate the impact of this substrate on system performance. This research was conducted with help of Dr. Chris Stachurski, Elisabeth Woods, Kyle Lira, Pamela Joy Tabaquin, and Dr. Nsoki Phambu of Tennessee State University. Portions of the research were prepared for publication within the peer reviewed journal ChemSusChem, and also appear in portions of the dissertation of Dr Christopher Stachurski. Dr Stachurski and I appear as co-authors for equal contribution to the research and manuscript.

4.1 Introduction

The demand for novel alternative energy solutions has driven increased focus on improving photovoltaic devices. Photosynthesis remains the most efficient process of converting solar radiation into usable energy, and since the 1980's has inspired research into plant-based biohybrid photovoltaic devices[122,178]. Photosystem I (PSI) is a transmembrane protein found within the chloroplast, specifically the thylakoid stacks, of plants, algae, and cyanobacteria, and plays a critical role within photosynthesis as an efficient photodiode. The roughly 500 kDa protein is primarily composed of a large array

of chlorophylls, pigments related to reduced poryphins with a magnesium complex, that surround an electron-transport chain which begins at a chlorophyll dimer at the center of the protein denoted as P_{700}, travels through a series of Phylloquinone mediators, and terminates at an Iron-sulfur complex known as F_B. The protein absorbs solar energy within the array of chlorophylls, which excites electrons at the P_{700} site, through the transport chain. At F_B, electrons are transferred with energy of -3.9 eV compared to vacuum[81,88].

In order to utilize PSI's unique photoelectric properties, biohybrid electrodes capable of both mediated and direct electron transfer have been fabricated using diffusible aqueous mediators or direct protein immobilization on charge transport layers, respectively[127,179-183]. The efficacy of the resulting devices depends both on the overlap of material work functions or redox potentials, and the connections between the protein and the charge transfer layers. Our lab has previously created self-assembled monolayers of PSI directly on precious metal electrodes like gold and silver, demonstrating improved performance with different materials, layer thickness, and method of deposition[120,122]. More recent efforts have incorporated conductive polymers, like polyaniline (PANI) and poly 3,4-ethylenedioxythiopene/polystyrene sulfonic acid (PEDOT/PSS), to serve as a charge transfer layer for the protein with and without the use of a liquid mediator. The polymers provide a three-dimensional framework to entangle the protein, increasing light adsorption and PSI loading, while also serving to preserve the protiens[120,122]. These systems have shown improvement over earlier designs but can be limited based on the surface material of the electrodes, the thickness of the polymer layers, and the interfaces between materials within the cells. The ideal thickness of the active layer in these devices must balance optical density, which maximizes the photons absorbed by the PSI, and the physical distance to the cathode, which can limit carrier diffusion efficiency and reduce current

density in some designs[122].

Carbon in various forms has been used as an electrode material in numerous types of electrochemical devices, including fuel cells, sensors, and capacitors. Pyrolytic carbon was used as an electrode material in early biohybrid photovoltaic devices and PSI monolayers have been successfully assembled on both graphene and reduced graphene oxide.[103,184-185] Recent studies have investigated carbon materials as alternatives to inorganic electrodes in PSI biohybrid solar cells. Carbon materials exhibit high conductivities, diverse morphologies, and increased affordability over metal-based substrates promoting their rapid incorporation into biohybrid energy applications. Many carbon allotropes are also amenable to upscaling alongside PSI as a means of device enhancement. Gunther et al. demonstrated how graphene could interface with monolayers of PSI for sustained anodic photocurrent production in the presence of diffusible chemical mediators[103]. Darby et al. expanded upon this work by substituting in reduced graphene oxide to facilitate higher amounts of PSI loading and lead to upwards of 5 $\mu A\ cm^{-2}$ of observed photocurrent[185]. Beyond planar allotropes of carbon, Ciornii et al. utilized multiwalled carbon nanotubes as a scaffold for PSI immobilization through the use of the redox protein cytochrome C (cyt C) to produce up to 18 $\mu A\ cm^{-2}$ at biased electrodes[186]. More recently, Morlock et al. created three-dimensional structures of reduced graphene oxide capable of similar cyt C-assisted immobilization of PSI, leading to high photocurrents (14 $\mu A\ cm^{-2}$) and high rates of protein turnover (30 $e^-\ PSI^{-1}\ s^{-1}$)[187]. Despite these successes, past uses of carbon allotropes in PSI biohybrid devices are often layered on conventional electrodes, such as gold or glassy carbon, restricting the benefits of affordable, sustainable, and scalable carbon materials. Some devices replace electrode materials with insulating supports, however additional processing steps serve as barriers to upscaling.

Carbon paper (CP) is a promising affordable electrode candidate for biohybrid photoelectrochemical cells due to inherently high surface area and conductivity. Commercially available carbon paper is composed of polyacrylonitrile fibers that have been arranged into sheets and carbonized with heat or chemicals. This material has been used extensively within fuels cells, capacitors, catalyst and photovoltaic devices, with consistent and characterized electrochemical properties.[79,173,188-194] Desirable attributes like high conductivity, minimal corrosion, and high mechanical strength make the substance ideal for certain applications. Past work by Rasmussen et al. demonstrated how CP has been employed as an electrode in whole thylakoid devices capable of highly sensitive herbicide detection using spinach-extracted thylakoids[195]. The high surface area of CP substrates makes them promising candidates for PSI-polymer composites prepared using electropolymerization. Protein-polymer composites have demonstrated improved structural and photoelectrochemical performance despite lower-than-average quantities of protein due to favorable interactions between the conducting polymer and terminal reaction centers of PSI. Robinson et al. successfully encapsulated PSI multilayers within a vapor-phase polymerized PEDOT scaffold which produced high-activity composite films resistant to delamination[123]. Gizzie et al. employed a solution of PSI and aniline monomer to rapidly grow photoactive films on planar gold electrodes, showing that the entrapped PSI outperformed more dense multilayers prepared in the absence of polyaniline (PANI)[122], yet planar electrodes have shown limitations in electropolymerization processes as diminishing returns are observed beyond critical film thicknesses. These limiting factors can be overcome by using three-dimensional electrodes that offer significantly higher electrode surface areas per geometric area, which enables significantly more electropolymerization before desorption limits any additional growth.

In this work, PSI is interfaced with CP electrodes either through physical adsorption or entrapment in conducting polymers formed *in situ*. Following preconditioning, the treated CP electrodes exhibit much improved hydrophilicity, which in turn increases the electrode surface area and leads to the formation of dense electroactive films. The prepared PSI or PSI-polymer films are assembled by using different procedures and tested in the presence of multiple chemical mediators to identify the optimal conditions for devices of this nature. Optimal devices generated up to 220 nA cm^{-2} of anodic photocurrent density governed by diffusion limited pathways rather than kinetic limitations at the electrode. Additionally, PANI and PSI were electropolymerized on planar gold, high surface area gold , and carbon paper electrodes to compare photocurrent density, polymer morphology, and protein entrapment in order to better demonstrate the impact of the high surface area electrodes on device performance. The composition and preparation of CP-based bioelectrodes prepared in this study opens the door to rapidly scalable device assembly unhindered by the limitations tied to systems based on inorganic materials and can lead to truly sustainable sources of renewable energy.

4.2 Materials and Methods

Toray Carbon Paper-060 was purchased from the Fuel Cell Store (fuelcellstore.com) in 20 cm x 20 cm sheets. The carbon paper sheets were covered with a standard 5% weight wet proofing layer of Teflon. Sheets were 0.19 mm thick, with a porosity of 78% and a resistivity of 80 mΩ cm through the plane as reported by the manufacturer. Hydrochloric acid, sulfuric acid, sodium phosphate monobasic, potassium chloride (Fisher Scientific), 3,4-ethylenedioxythiophene (EDOT), poly(sodium 4-styrenesulfonate) (PSS), aniline,

ruthenium hexamine trichloride (RuHex), ferricyanide, ferrocyanide, methyl viologen dichloride (MV), sodium ascorbate, 2,6-dichlorophenolindophenol (DCPIP), 2,3-dimethoxy-5-methyl-p-benzoquinone (ubiquinone-0)**,** triton X-100 (Sigma Aldrich) were procured and used as received. All deionized water (DI-water) was purified in-house (Millipore, 18 MΩ cm). Locally procured organic baby spinach from was used as the source of PSI for all experiments.

4.2.1 PSI extraction

The method used to extract PSI has been previously described and is based on the protocols developed by Reeves and Hall[139]. Fresh spinach was macerated in buffer to separate thylakoids from the rest of the leaves. After isolating the thylakoids from the remaining cell debris, Triton X-100 surfactant was added to release PSI from the membrane. The samples were once again centrifuged, and loaded through a hydroxyapatite column, trapping the PSI protein complex. The column was washed with a buffer solution to release the PSI protein under high salt buffers. Samples were then stored in 2 mL aliquots at -80° C and dialyzed to remove surfactants and salts prior to use within experiments. PSI aliquots were measured to be 1 μM in concentration following quantification with Baba's assay.

4.2.2 Electrode Preparation

Toray carbon paper-060 was cut into rectangular electrodes, approximately 3cm x 2cm. A tag of adhesive copper tape, 3 cm in length was attached to one side of the electrode and used for electrical contact. The electrode was then covered with a PortHole inert electrochemical mask (Gamry Instruments) leaving a circular exposed area of 0.71 cm^2. Electrodes pretreated with acid were briefly wetted with ethanol, then submerged in 0.1 M sulfuric acid for 5 min. Samples were rinsed with DI-water and allowed to dry. Additional

CP electrodes were subjected to flame treatment instead, consisting of 5s exposures to an open flame, followed by a DI-water rinse and masking analogous to the previously discussed samples. Gold electrodes were produced in an Angstrom Amod combined e-beam resistive and sputter deposition chamber via electron-beam physical vapor deposition of titanium (10nm adhesion layer) and gold (120nm) onto a standard silicon wafer (<100> orientation, University Wafer). The wafer was cut into 2cm x 2cm electrodes and covered with masking tape on the gold, leaving a circular exposed area 0.71cm^2. High surface area gold electrodes were prepared by evaporating a chromium adhesion layer (10nm) and gold (125nm) directly onto flame-treated, pre-cut CP electrodes, at a rate of .2nm/s in a diffusion pumped chamber at a base pressure of 4x10^{-6} Torr.

4.2.3 Electrochemical Measurements

All electronic measurements were conducted using a CH Instruments 660A electrochemical workstation using a three-electrode setup with either modified carbon paper or gold working electrode, a platinum mesh counter electrode and an Ag/AgCl (sat'd KCl) reference electrode. Cyclical voltammograms (CVs) of 2mM RuHex and ferri/ferrocyanide in electrolyte solution consisting of 1M KCl were obtained using CP electrodes subjected to different treatment methods as the working electrode.

Electropolymerization of polymer or polymer-PSI composites were prepared using a protocol modified from previous works. For poly(3,4-ethylenedioxythiophene) polystyrene sulfonate (PEDOT:PSS) and PEDOT-PSI films, a monomer stock solution containing 0.01 M EDOT, and 0.1 M PSS were combined with a 0.02 M phosphate buffer containing 0.001% wt. Triton X-100 with or without PSI. The two solutions, denoted as solution A (EDOT & PSS) and solution B (eluted PSI or phosphate buffer) were combined 4:1 volumetrically

unless otherwise specified. Films were polymerized either potentiostatically at +1.2 V (vs. Ag/AgCl) for varied times or by cycling the working electrode potential between 0 and +1.3 V at a scan rate of 0.1 V s^{-1} for varied numbers of cycles.

Photochronoamperometry (PCA) was performed under applied potentials matching the open circuit potential in either pure electrolyte or mediator solutions containing 2 mM RuHex, 2 mM MV, 5 mM sodium ascorbate/250 μM DCPIP, or 2mM ubiquinone in 1 M KCl unless otherwise specified. During photocurrent measurements, electrodes were held in the dark for 40 s before illumination using a 100 mW cm^{-2} light source (KL 2500 LCD, Micro Optical Solutions, Newburyport, MA) with 20 s followed by another 40 s of darkness.

Electrochemical impedance spectroscopy (EIS) was performed in a solution containing 2 mM RuHex and 1 M KCl using a three-electrode configuration as described above. The potential was oscillated 10 mV above and below the measured OCP (usually around -0.112 V vs Ag/AgCl) from 10,000 Hz to 0.01 Hz. The relevant values were obtained from the resulting data by fitting with a Randles equivalent circuit using EC-Lab software v10.40.

4.2.4 Additional Instrumentation

Scanning electron microscopy of the samples was conducted using a Zeiss Merlin system with a GEMINI II column using a 2 keV accelerating voltage at a working distance of 5 mm, with an InLens secondary electron detector.

All contact angle measurements were made using a Rame-Hart goniometer. A static 1 μL drop of deionized water was added to each sample and the contact angle was measured at one side of the drop. Triplicate samples were measured for each reported condition and the average contact angle with standard deviation is reported.

Raman measurements were conducted on a Thermo Scientific DXR confocal Raman microscope. All measurement were made using a 532 nm laser under normal operation parameters.

Quantification of protein entrapped within electropolymerized PANI on both planar gold and CP electrodes was conducted using a PerkinElmer Optima 7000 inductively coupled plasma optical emission spectrometer(ICP-OES), calibrated for iron emission at 238.204 nm. For quantification, a five-point calibration was constructed from Fe standards (SPEX CertiPrep) at 0, 10, 20, 35, and 50 ppb in 5% nitric Acid. Both planar gold and CP electrodes, with 1cm^2 of exposed surface area, were prepared and electropolymerized as described above with 1μM eluted PSI solution for either 45, 90, or 180s. Additional films were prepared without PSI as controls. Films were then digested with minimal concentrated nitric acid (Fisher, TraceMetal Grade) and diluted to 5% nitric acid with DI water.

4.3 Results and Discussion

4.3.1 Pre-treatment of CP Electrodes

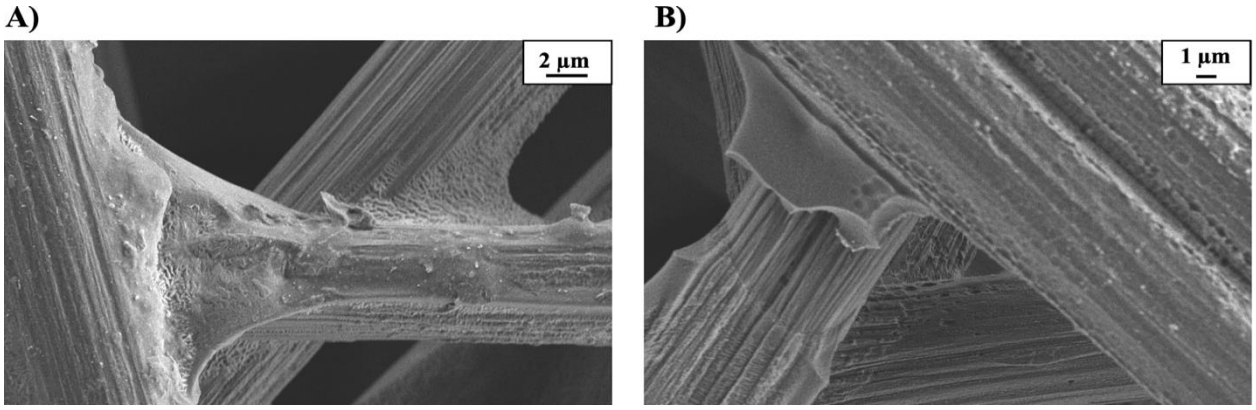

Figure S1. SEM images of carbon paper before (A) and after (B) flame treatment by exposure to a Bunsen burner for ~5 s.

Many carbon paper substrates are prepared for applications as gas permeation membranes and, as such, often come pretreated with a polytetrafluoroethylene (PTFE) coating. This

PTFE coating fortifies the CP materials against tear and does not detract from the material's superior conductivity. As a result of this treatment, however, CP surfaces often express hydrophobic or superhydrophobic properties, making them incompatible with aqueous electrochemical systems, including PSI-containing solutions. To prepare the electrodes for use in PSI biohybrid devices, CP substrates were pretreated by either chemical oxidation using sulfuric acid or flame treated using a Bunsen burner prior to use in electrochemical applications. By first wetting the substrate with ethanol followed by a brief (5 min) exposure to sulfuric acid, the wettability of the CP substrate was significantly enhanced as shown by the change in contact angle from 122 +/- 4° to 24 +/- 2° (Figure 4.2). More extreme surface modification was achieved through flame treatment and the resulting substrate (FT-CP) was fully wettable (< 5°) posing no barrier to interaction with PSI-containing solutions.

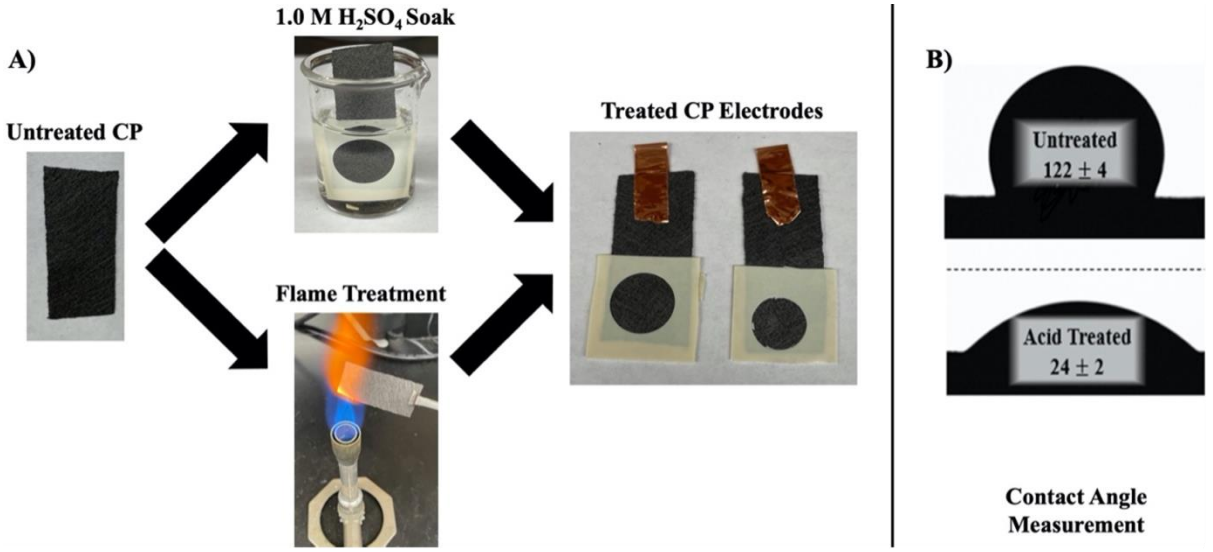

Figure 4.2. (A) Schematic of the oxidative treatment process used on CP substrates. Substrates were first cut to the desired dimensions. Samples to be acid treated were masked first followed by submerging the exposed surface area to a 1.0 M solution of H_2SO_4. (B) Following treatment CP surfaces exhibited superior hydrophilicity as compared to their untreated counterparts.

This improved hydrophilicity is attributed to simultaneously increasing the physical roughness of CP fibers, as evident in SEM images pre and post-treatment (Figure 4.1),

removing the PTFE coating, and increasing functionalized sp^3 carbon as evidenced in the resulting Raman spectra (Figure 4.3). Over the two treatment methods applied to CP substrates, the ratio of the D-band (~1356 cm^{-1}) to the G-band (~1585 cm^{-1}), comprising of signal from sp^3 and sp^2 carbon, respectively, increased from 0.13 (CP) to 0.60 (FT-CP). An increase in sp^3 hybridized carbon at the electrode surface suggests a more polarity, and in turn, an increasingly hydrophilic substrate. This finding is consistent with the results Choi et al., who sonicated commercial carbon paper in a mixture of concentrated sulfuric and nitric acid to improve the adhesion of polyaniline (PANI) polymerized from aqueous solutions[196].

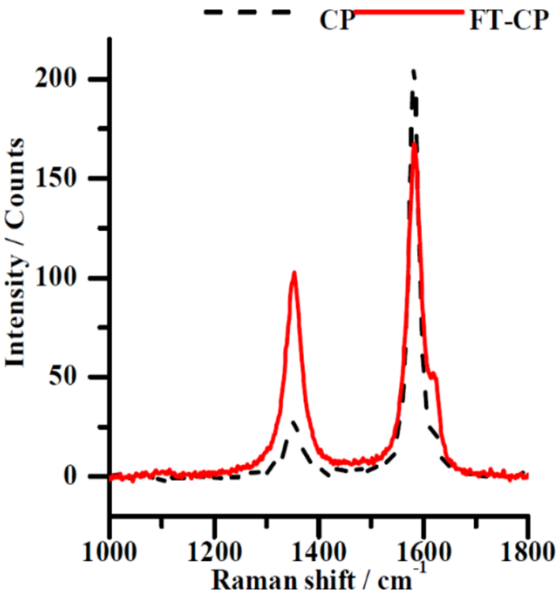

	$I_{p,D}/I_{p,G}$
Control	0.128 ± 0.006
Acid Soak (1 M, 30 min)	0.260 ± 0.008
Flame Treat	0.60 ± 0.02

Figure 4.3. Raman Spectra of Untreated CP and FT-CP electrodes. The resulting Raman spectra for untreated CP and flame treated CP electrodes. Following flame treatment, the I_D/I_G increases from 0.13 to 0.60 representing an increase in sp^3 functionalized carbon at the substrate surface.

Electrochemical characterization was used to measure changes in the electroactive surface area, likely a result of improved CP hydrophilicity following surface pretreatment. Cyclic voltammograms of CP substrates treated using different methods show increased faradaic and non-faradaic current responses over those without any form of modification.

Increased faradaic responses at CP electrodes that underwent more intense pretreatment demonstrate superior electroactive surface areas when compared to untreated CP or planar glassy carbon (Figure 4.4).

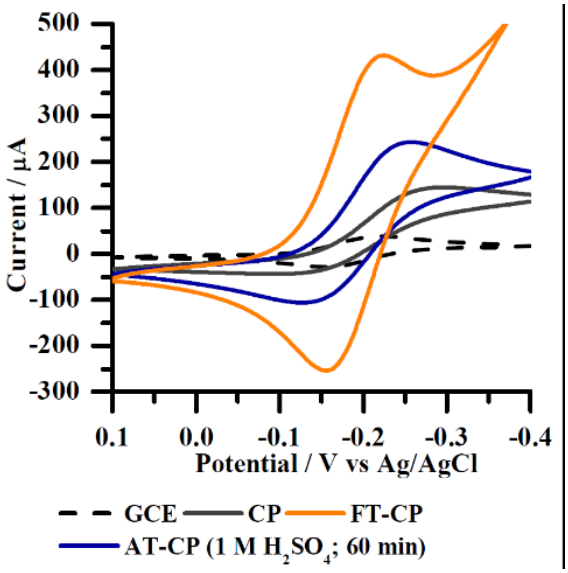

Figure 4.4. Cyclic voltammograms at 100 mVs^{-1} of untreated CP, acid treated CP (treated with 1M H_2SO_4 for 60 min), flame-treated CP, and a bare glassy carbon electrode in the presence of 2 mM RuHex and 1 M KCl mediator solution.

Peak currents (I_p) for the FT-CP increased by factors of six and nine for the observed oxidation and three and eleven for the observed reduction reaction, with respect to untreated CP and glassy carbon controls. These results, in conjunction with the observed increase in hydrophilicity, suggest that the applied treatment methods allow more of the available surface area of the CP substrates to be accessed by aqueous solutions, promoting their use in energy or sensing applications, including use with PSI-based systems.

As with the development of porous metal or semiconducting electrodes, the impact of porosity on electrochemical behavior can often obscure surface area-driven electrochemical measurements. Measuring changes in the capacitive behavior of the electrode can assist in characterizing changes to the electrochemically active surface area (ECSA) of a porous

material. By plotting the increase in non-faradaic current at varying scan rates, the specific capacitance (F cm^{-2}) for the electrode can be obtained and compared to determine changes in surface area between electrodes of similar composition, assuming the treatment does not significantly alter the double-layer capacitance of the material. Flame treatment of the CP substrate resulted in a change to specific capacitance two orders of magnitude greater than Acid-treated CP, and nearly 170 times that of untreated CP. These results align with the surface area enhancement trends observed through faradaic current-based processes.

As it stands untreated CP remains largely inaccessible to aqueous solutions detracting from its application in PSI-based biohybrid devices. Through simple and rapid pretreatment methods, CP electrodes can easily be converted into a usable, high surface area substrate in biohybrid solar energy conversion, serving as a metal-free alternative in energy harvesting applications. The superior wettability, hybridization, electroactive surface area, and minimal pretreatment requirements of FT-CP made it the modification method of choice over AT-CP and untreated CP for this work.

4.3.2 PSI Multilayers on Carbon Paper Substrates

In order to demonstrate the viability of CP substrates in PSI-based photoelectrochemical devices, electrodes were coated with varying amounts of PSI using vacuum-assisted deposition, a common method for loading PSI or other biological species onto electrode surfaces. The resulting photocurrents produced within electrochemical wet cells of multilayered devices were anodic regardless of the diffusional mediator species used within the system (Figure 4.5A).

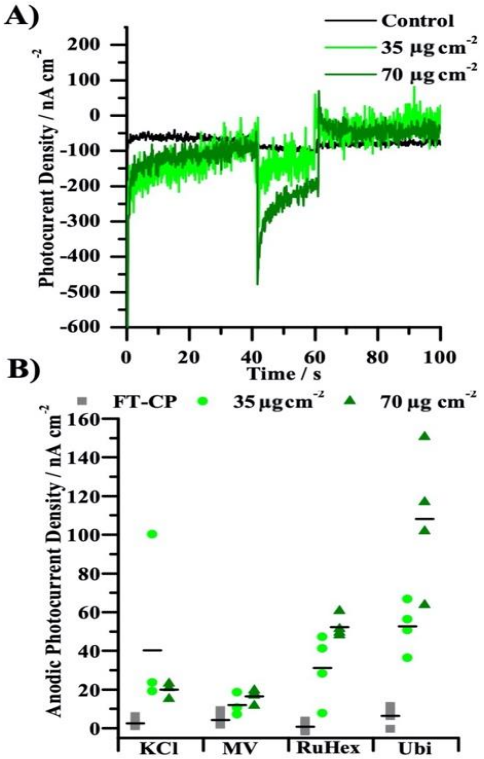

Figure 4.5. (A) Steady state photocurrent densities of control and PSI multilayers on FT-CP in the presence of various mediators (n = 4). Average photocurrent densities are represented by a solid dash. (B) The resulting photocurrent behavior of PSI multilayers under different deposition amounts in the presence of a 2 mM ubiquinone mediator.

The chosen mediators preferentially accept photoexcited electrons from the stromal F_B^- reaction center which leads to excess buildup of reduced species at the working electrode. Anodic photocurrent is realized when the reduced mediator species is sequentially oxidized at the underlying electrode. Of the mediators tested ubiquinone and RuHex showed the best improvement in photocurrent density, which is attributed to greater overpotentials versus the F_B reaction center of PSI when compared to methyl viologen. While RuHex exhibits the greatest overpotential with respect to F_B^-, ubiquinone undergoes a two-electron transfer and has been well characterized as an electron acceptor from photosynthetic protein complexes pointing to its overall higher performance.

Inherent photoactivity was observed at FT-CP control devices; however, the magnitude of this current was negligible (< 5 nA cm^{-2}) compared to the photocurrent densities produced

with PSI-modified electrodes. The shapes of the current profile exhibit time-dependent Cottrellian decay, indicating similar behavior of PSI on carbon fiber electrodes to multilayers assembled on conventional inorganic electrodes (Figure 4.5B). Furthermore, the time-dependent decay indicates diffusion-limited pathways are responsible for the sustained photocurrent, which directly benefit from increased electrode surface areas. Overall, PSI-modified carbon paper electrodes produced significantly higher photocurrent densities than unmodified CP substrates. When mediated with ubiquinone, the mean photocurrent density was 0.11 μA cm^{-2}, a 15-fold enhancement over bare FT-CP (0.007 μA cm^{-2}). These results validate adequately treated CP substrates as suitable electrodes for PSI, expanding what had previously been achieved using whole thylakoid systems.

4.3.3 Rapid Immobilization of PSI on CP Substrates Through Electropolymerization

In order to take advantage of the high surface area of treated CP substrates in PSI-immobilization, electropolymerization was used to entrap PSI within a conducting polymer scaffold formed *in situ*. As a result of their electrochemical growth, polymers used in electropolymerization are often inherently conductive, making them favorable for use in solar cells or other energy-related applications. Beyond PSI entrapment for solar energy conversion, this technique is also useful for the immobilization of enzymes and other sustainable components useful for sensing, energy production, and fuel generation.

To successfully entrap PSI in a conductive, electrochemically polymerized layer on CP or treated CP substrates, all components must first be combined and exposed to sufficient electrical potential needed to drive polymerization. The conductive polymer poly(3,4-ethylenedioxythiophene) polystyrene sulfonate (PEDOT:PSS) was chosen for its optical

transparency, low inherent photoactivity, and previously demonstrated success when used in PSI-based devices. In order to verify the occurrence of electropolymerization at the CP surface, substrates subjected to different treatment methods were exposed to both control and monomer-containing solutions and held at a constant potential of +1.2 V (vs Ag/AgCl). The resulting charge transferred to the solution was compared to evaluate the extent of polymerization (Table 4.1).

Table 1. Mean charge delivered (mC) during a 40 s hold of fixed potential +1.2 V (vs Ag/AgCl) in the absence and presence of EDOT:PSS and PSI (n = 3). [a] Control electrodes prepared by following electropolymerization protocol in phosphate buffer only.

	Control[a]	**PEDOT: PSS**	**PEDOT: PSS + PSI**
CP	-0.18 ± 0.06	-0.68 ± 0.08	-0.49 ± 0.50
FT-CP	-3.4 ± 0.1	-13 ± 2	-9.8 ± 0.8

Carbon paper electrodes produced higher net charges in runs containing EDOT and PSS when compared to exposure to a control solution of pure electrolyte (Table 4.1), indicating the occurrence of new faradaic processes tied to polymer formation. FT-CP consumed a 19-fold higher net charge over untreated CP indicating more extensive polymerization at hydrophilic surfaces. SEM images also confirm the more liberal growth of polymer off treated CP surfaces as compared to unmodified carbon paper. When polymerized in the presence of PSI, the total charge passed during polymerization remained largely unchanged, suggesting the presence of PSI protein did not significantly impede the growth of PEDOT:PSS.

Protein films were formed using an electropolymerization solution composed of a 1:4 ratio of precursor solution (0.01 M EDOT and 0.1 M PSS) to extracted PSI solution, with control films substituting unmodified elution buffer for PSI extract. Higher ratios of PSI to monomer than what have been used previously on planar electrodes were necessary to improve protein loading in the rapidly forming films due to higher surface area at treated carbon surfaces. Devices were tested in mediator solutions of 1 M KCl electrolyte. High electrolyte concentrations were used to improve the overall performance of the devices, as lower concentrations of KCl can lead to drifting dark photocurrents (I_{dark}). The drifting I_{dark} most likely stems from the high charging current associated with these high surface area, highly capacitive materials and should be accounted for when applying these materials to electrochemical systems.

Across the mediators tested, PSI-polymer films produced anodic photocurrent, similar to the results observed with vacuum deposited protein. Photocurrent densities were calculated by taking the difference between average light photocurrent densities (J_{light}) and dark photocurrent densities (J_{dark}) before and after light exposure. Across most mediators, composites containing PSI outperformed PEDOT:PSS films devices fabricated on flame treated CP (Figure 4.6).

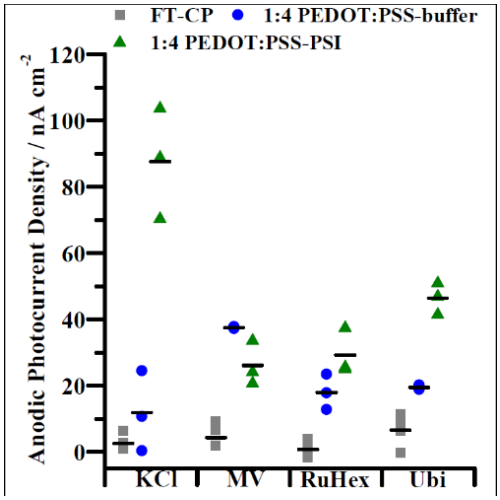

Figure 4.6. Photocurrent densities of composites formed on flame-treated CP substrates under potentiostatic conditions of +1.2 V for 40s in 1 M KCl with no mediator, 2mM MV, 2 mM RuHex, 2 mM ubiquinone (n = 3). Average photocurrent density values are represented by a solid dash.

The best performance was achieved in pure electrolyte solution, suggesting dissolved oxygen is effective at shuttling charge from the composite films to the underlying carbon electrode, with PSI-containing devices exhibiting a 7-fold increase in current density (-12 nA cm^{-2} vs -87 nA cm^{-2}). Relying on dissolved oxygen is not ideal for sustained photocurrent generation, however, as the formation of reactive oxygen species (ROS) can lead to protein and polymer degradation. The next best performance was observed in the presence of ubiquinone. Ubiquinone and other quinone derivatives are known to be natural electron acceptors in aerobic photosynthesis making them suitable candidates for PSI-based biohybrid devices.

In order to optimize the PEDOT:PSS-PSI composites prepared, alternative electropolymerization conditions were tested in order to maximize polymer growth and PSI intercalation. Using the same 1:4 ratio of monomer solution to PSI solution, increased polymerization times were tested at a constant +1.2 V (vs Ag/AgCl). As expected, the charge consumed and as such PEDOT:PSS grown increased proportionally with the polymerization time (Table 4.2); however, the photocurrent density barely increased (Figure 4.7).

Table 2. Mean charge delivered (mC) under different polymer growth conditions. PEDOT:PSS growth was achieved with either a set number of cycles between 0 and +1.3 V (vs Ag/AgCl) or for a set length of time at +1.2 V (vs Ag/AgCl) in the presence of PSI (n = 3).

	15 Cycles	**30 Cycles**	**50 Cycles**	**40 s**	**80 s**
Polymer	-39 ± 2	-69 ± 18	-98 ± 27	-16 ± 2	-35 ± 4
Polymer: PSI	-75 ± 30	-99 ± 25	-133 ± 21	-22 ± 1	-44 ± 1

Additionally, a potential sweep-based polymerization method (0 to +1.3 V vs Ag/AgCl potential window) was used in which the electrode was cycled between periods of electropolymerization (+0.9 to +1.3 V vs Ag/AgCl) and rest (+0.9 to 0.0 V vs Ag/AgCl). Under potential sweep electropolymerization, the quantity of polymer grown can be correlated to the number of growth-rest cycles performed, albeit with higher degrees of variance (Table 4.2).

The photoactivity of PEDOT:PSS controls prepared using a cycled potential method was higher than the photocurrent densities of films grown under potentiostatic conditions despite similar quantities of consumed charge during polymerization (Figure 4.7). Upon addition of PSI into the films, photocurrent densities of composites prepared using the cycled potential technique further increased well above the currents seen under potentiostatic growth. Increasing the number of cycles further improved the photoactivity and the deviation between devices. Ultimately, devices subjected to 50 potential sweep cycles produced the highest photocurrent densities (-196 nA cm^2), nearly a 4-fold increase over PSI-PEDOT:PSS films prepared under an 80 s potential hold (-53 nA cm^2) (Figure 4.7**)**. The photocurrent density from these films also surpassed what was achieved with PSI multilayers prepared using vacuum-assisted deposition warranting the use of electropolymerization as a rapid, accessible method to prepare bioelectrodes.

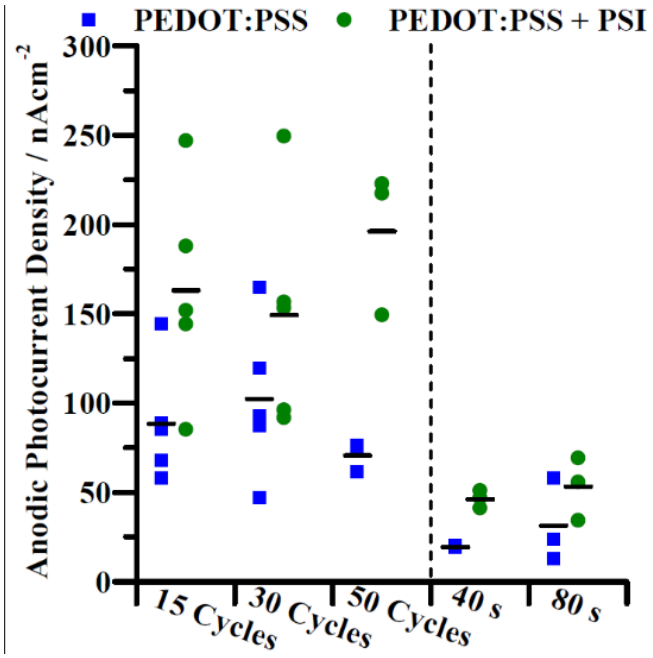

Figure 4.7. Photocurrent densities of PEDOT and PEDOT-PSI composites on FT-CP. Composites were formed either using a potential sweep method (100 mV s^{-1} scan rate from 0 V to +1.3 V for 15, 30, or 50 cycles) or potentiostatic conditions at varying times. All films were tested with a 2 mM ubiquinone/1 M KCl. Average photocurrent density values for the plotted device performances are represented by a solid dash.

PEDOT:PSS preparation using cyclic voltammetry seemed to have a more pronounced impact on the quality of protein-polymer composite. For one, the net charge consumed under potential sweep polymerization was greater than what was seen under potentiostatic growth, indicating higher densities of polymer at the electrode surface (Table 4.2). The photocurrent densities also surpassed what is expected solely based on the higher degree of polymerization, as evidenced between the electrodes prepared with 50 potential sweep cycles and those prepared under an 80 s potential hold. Whereas the charge consumed during electropolymerization increased by a factor of 3 for the two conditions, photocurrent densities increased nearly 4-fold, suggesting further enhancement of the produced composites. Cycling the applied potential during electropolymerization likely aids in replenishing protein and monomer at the growing electrode, improving device performance as seem with other bioelectrodes prepared in a similar manner.

The photocurrent densities obtained at FT-CP substrates are comparable to PSI multilayers assembled on graphene and graphene oxide coated substrates; however, the methods proposed in this study can be more readily applied in large scale device assembly applications and are better suited for distributable energy production. Furthermore, the photocurrent enhancement factor is greater than the observed increase in charge consumed during polymer growth. Additional factors such as increased protein loading likely contribute to photocurrent enhancement beyond increased polymer growth under dynamic polymerization conditions promoting their use in bioelectrode preparation. In conclusion, carbon paper substrates open the door to disposable, affordable, metal-free bioelectrodes capable of scalable solar energy conversion. These results support the surface area enhancement trends observed through faradaic current-based processes. As it stands untreated CP remains largely inaccessible to aqueous solutions detracting from its application in PSI-based biohybrid devices. Through simple and rapid pretreatment methods, CP electrodes can easily be converted into a usable, high surface area substrate in biohybrid solar energy conversion, serving as a metal-free alternative in energy harvesting applications.

4.3.4 Planar gold vs CP electrodes

To better determine the performance of CP electrodes in PSI based systems, additional experiments were conducted using planar gold electrodes as controls. Planar gold electrodes were used in previous studies as the substrate for electropolymerized PANI/PSI films. While this previous study demonstrated an advantage over devices composed of PSI multilayers, it did highlight limitations to the design. PANI electropolymerized onto gold electrodes with PSI had a greater photocurrent density than control gold electrodes with

the same polymerization times without PSI. In that study, the major difference was not observed until 40s of polymerization[122]. Further, that study showed the thickness of the PANI films increased linearly for the first 10-40s, prior to reaching a terminal thickness of 200nm, due in part to the concentration of surfactant and monomer within solution[122].

In this study, planar gold and CP electrodes were prepared with and without PSI using potentiostatic deposition for 45 or 180s The CP electrodes produced greater photocurrent compared to gold electrodes under each condition. Photocurrent increased as polymerization time increased, in samples with and without PSI, further demonstrating the photoactive properties of PANI alone. This also suggest that increased polymerization time resulted in increased deposition of PANI on the carbon paper. Additionally, while the photocurrent produced by Au/PANI electrodes increased while extending polymerization time from 45s to 180s, Au/PANI/PSI electrodes demonstrated lower photocurrents than the electrodes without PSI, given the same polymerization time. This can be attributed to a reduced amount of PANI polymerized and a low concentration of PSI. This trend is in contrast with CP samples, which showed increased improvement in photocurrents from CP/PANI/PSI electrodes over CP/PANI electrodes as polymerization time increased(Figure 4.8).

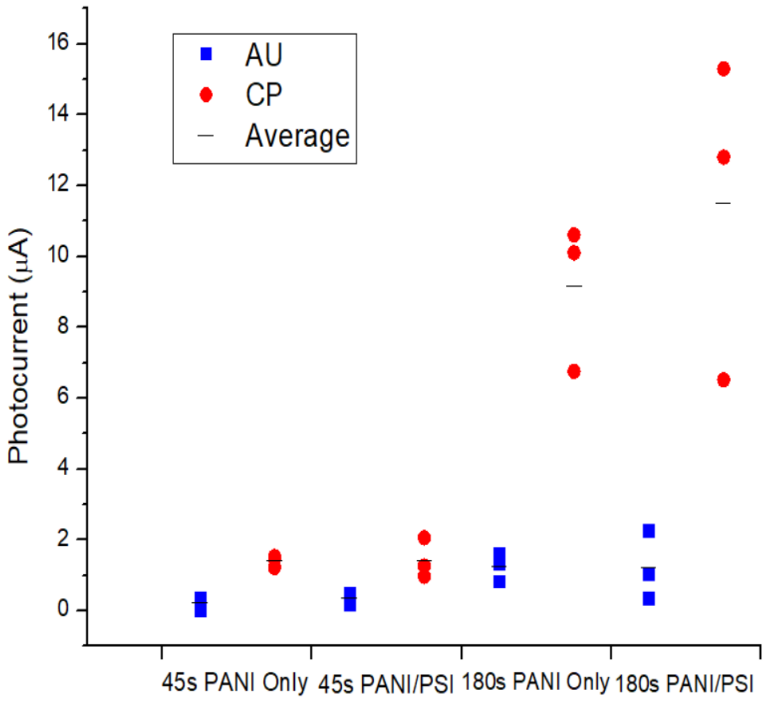

Figure 4.8 Photocurrent Density of planar gold and CP electrodes with PANI/PSI or PANI only films.

CP electrodes, with and without PSI, produced greater photocurrent density than planar gold controls, in part due to the photo response of PANI. The current experiment did not observe a terminal thickness of the active layer on the carbon paper electrode, nor did it observe a tradeoff between increased thickness and photocurrent. The porosity and inherent roughness of the CP electrodes did not allow for standard profilometry to observe the thickness of the PANI layers on the CP electrodes. Instead, this study integrated the polymerization current-time curve in order to compare the total charge delivered, which corresponds to the amount of aniline monomer polymerized. While this method did not account for PANI polymerized in solution and not adhered to the electrode, the greater amplitude of current at constant potential resulted in increased charge delivered during polymerization and increased photocurrent density in both gold and CP electrodes (Figure 4.9). Comparing the charge delivered during polymerization of PANI produced trends similar to those observed with PCA of the same electrodes, suggesting if the high surface

area electrodes did have a terminal thickness, it is beyond the limits of this experiment.

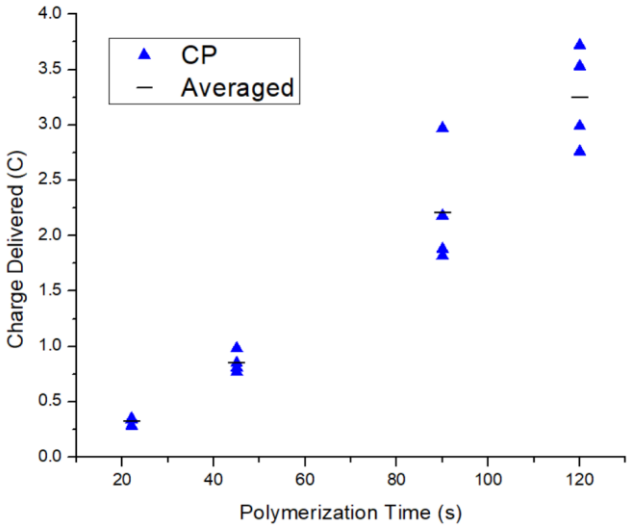

Figure 4.9 Charge delivered during potentiostatic electropolymerization of PANI onto CP electrodes at 22s, 45s, 90s, and 120s.

Further, this experiment quantified the PSI protein entrapped within the PANI films on both CP and planar gold electrodes, at different polymerization times using ICP-OES. Ideally, each PSI protein includes 12 iron atoms corresponding to the three Iron-sulfur complexes at the terminal end of the electron transport chain. Comparing the concentration of trace iron within the dissolved films allows comparison of the quantity of entrapped protein(Figure 4.10). Under each time conditions, the concentration of PSI within PANI films on CP electrodes was significantly greater than what was observed on planar gold. The concentration of protein in the films formed on planar gold did not significantly vary across the different polymerization times, which aligns with the previous observations of a terminal thickness of the PANI/PSI film. The increase in protein concentration in the CP films did not increase linearly with time, but exponentially. These results suggest that more PSI proteins were entrapped as the polymer fibers grew longer. The alignment of protein quantification results, with the observed charge delivered, and the measured photocurrent density suggest the increased surface area of the CP electrodes led to

increased loading of PANI/PSI films.

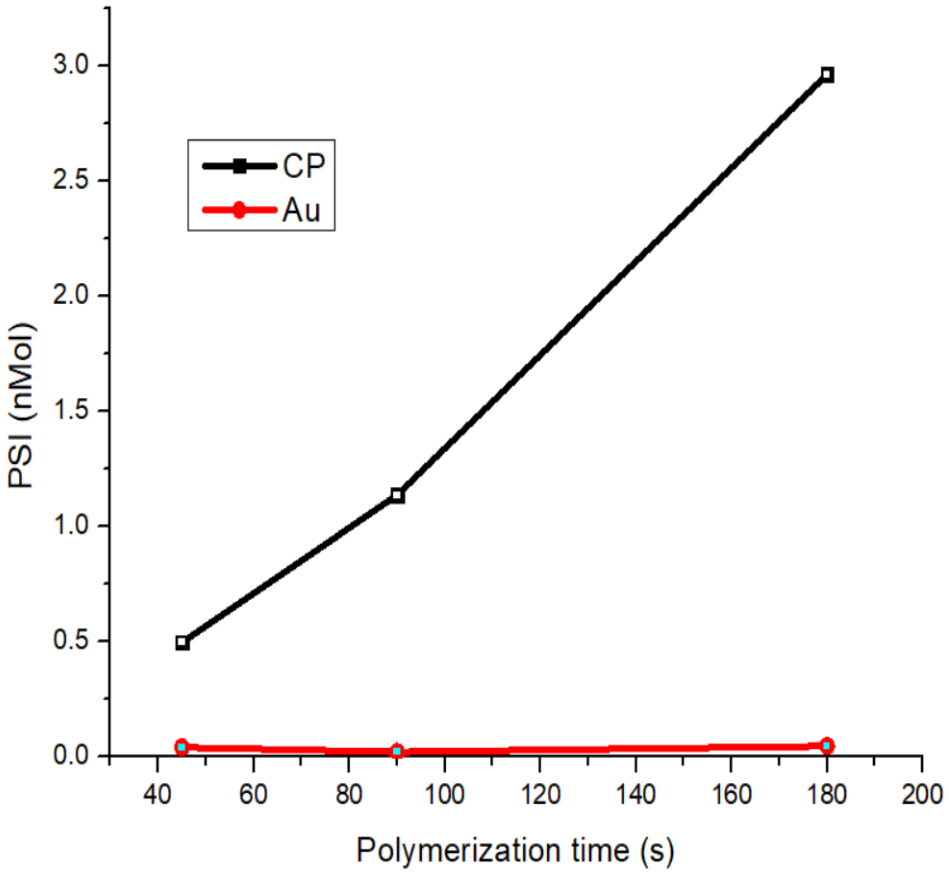

Figure 4.10 Plot of PSI content within the PANI/PSI films electropolymerized on planar gold and CP electrodes for 45s, 90s, and 180s. Values are based on ICP-OES detection of iron within digested films, using the stoichiometric relationship of 12 iron atoms to each PSI protein.

SEM of the electrodes showed the morphology of the PANI on the gold to be more globular compared to the more tendril style morphology observed on the carbon paper. This difference is observed at both time points, with and without the presence of PSI. The morphology of the PANI has been shown previously to correspond with conductivity of the polymer, suggesting a difference in the effectiveness as a charge transfer layer. As the surface area of the PANI increases, the distance for charge transfer decrease which in turn improves electrochemical performance.[148,151,157] Babaiee et al. worked to optimize electropolymerization of PANI on graphite by cycling potential between -0.2V and 1.0V, finding that slower sweeping rates, like 25mV/s, produced the most conductive PANI

construct. In the SEM provided of that experiment, the more conductive PANI appeared to have a greater surface area, and a morphology similar to what was observed in the CP electrodes.[148] Our polymerization techniques used a steady-state potential to produce the observed morphology. Zhang et al was able to observe the morphology of intermediates in the process of making chemically oxidized PANI, noting the presence of nanotubes, nanofibers, and microspheres at different points of the reaction. The more electroactive morphologies of tubes and fibers developed later in the reaction.[157] The difference in the morphology of PANI on the gold and CP electrodes contributes to the difference in photocurrent density of the systems.

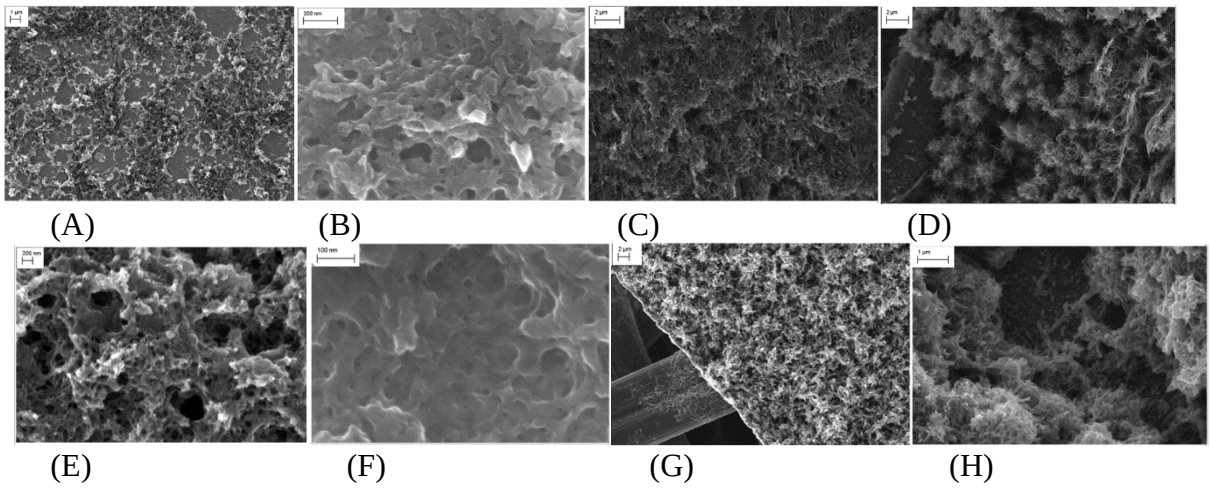

Figure 4.11. SEM Images of (A) 45s PANI on Gold(B)45s PANI/PSI on Gold (C)45s PANI on CP (D) 45s PANI/PSI on CP(E) 180s PANI on Gold(F) 180s PANI/PSI on Gold(G) 180s PANI on CP (H) 180s PANI/PSI on CP

EIS of both gold and CP electrodes with electropolymerized PANI further demonstrated the difference in the electrochemical properties of the PANI between the two electrodes. On gold electrodes, the charge transfer resistance increased significantly from bare electrodes to electrode with PANI polymerized for either 45 or 180s. In contrast, the charge transfer resistance in carbon paper electrodes was reduced dramatically between bare electrodes and samples with PANI polymerized over 45s, and much more for samples

polymerized for over 180s. The reduced charge transfer resistance corresponds with the increased surface area of the PANI on the carbon paper electrode. Further, the EIS results also demonstrate increased loading of PANI on the CP electrodes compared to the gold electrodes over the same time, through the increase in double layer capacitance. As a conductive polymer, PANI demonstrates inherent pseudo capacitance. In the gold samples the capacitance of the electrode is barely changed with the addition of PANI, or the increased polymerization time. On the CP electrodes the double layer capacitance is increased by orders of magnitude between the bare electrode and the electrodes with PANI polymerized over 180s. (Table 4.3)

Table 4.3 EIS data for CP and Planar gold electrodes without PANI films, and with PANI films electropolymerized for 45s or 180s. Impedance data was fit to Randles circuit and minimized to determine values. N=3

Sample	Polymerization time(s)	R_{CT} (ohms)	C_{DL} (F)
Au	0	46.7	1.77×10^{-6}
CP	0	422	1.41×10^{-6}
Au	45	678	3.64×10^{-6}
CP	45	40.2	1.08×10^{-4}
Au	180	531	2.80×10^{-6}
CP	180	1.34×10^{-7}	3.34×10^{-3}

To better understand if the improvement observe was a result of physical properties of the high surface area CP electrodes, or an electrochemical property of the CP electrodes, further study was conducted using high surface area gold electrodes. The process of evaporating gold directly onto the carbon paper substrate reduced the overall electroactive surface area, likely due to filling pits, and pores between fibers, however, the calculated ECSA of the electrodes was still roughly 4.5 times that of planar gold with the same geometric surface area (Figure 4.12). When comparing the electropolymerization curves, the high surface area gold electrodes take a shape more similar to the CP electrodes than

the planar gold electrodes, slowly decreasing in current magnitude during the initial 15s of polymerization, and gradually increasing with the remaining time. While the values of total charge delivered during electropolymerization were slightly lower than CP electrodes, the values were still significantly greater than planar gold electrodes and did not suggest a terminal thickness.

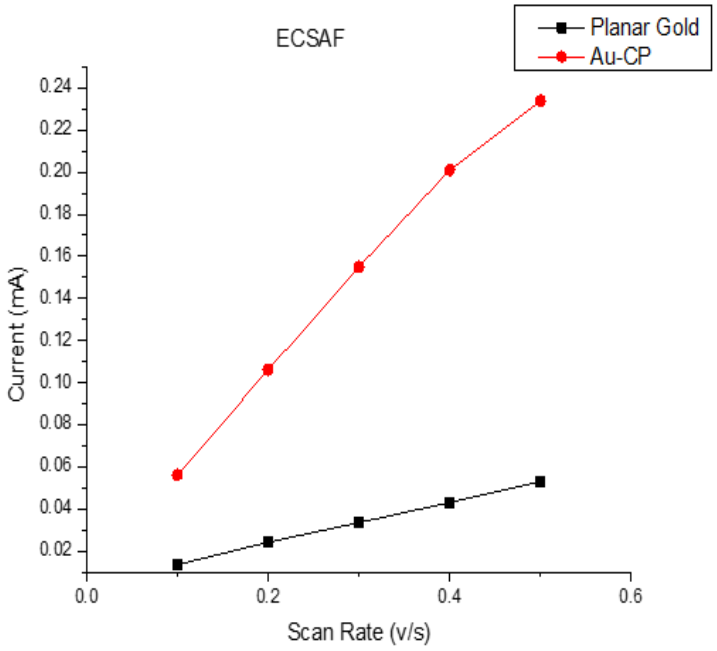

Figure 4.12 Linear depiction of ECSA scaling between planar gold electrodes and high surface area gold electrodes. Plotted points represent an average measured non-faradaic current at a specific potential away from redox reactions in CVs of the electrodes, against the scan rate of the CV. Comparing the slope of the lines allows comparison of the ECSA of electrodes of the same material

When comparing the photocurrent produced within photochemical wet cells, the high surface area gold electrodes produced significantly higher photocurrent than planar gold electrodes, and similar values as CP electrodes (figure 4.13). One distinction in the results for the high surface area gold electrodes was the increased difference between the photocurrent produced in PANI/PSI films compared to PANI only controls. This improvement may be attributed to the reflective properties of the gold, which allow incident light to be redirected back into the active layer, rather than absorbed in the carbon

paper.

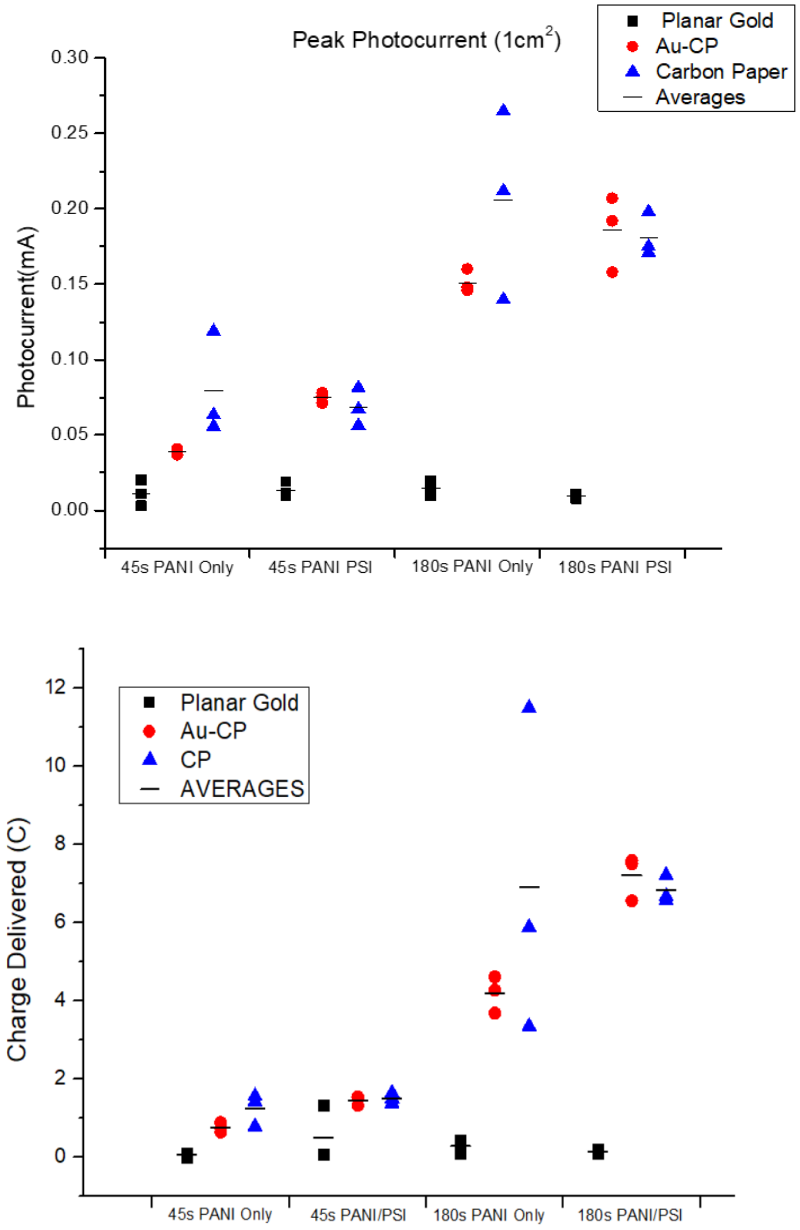

Figure 4.13 Photocurrent produced from planar gold, high surface area gold, and CP electrodes with PANI/PSI or PANI only films, electropolymerized 45s or 180s. Charge delivered during electropolymerization.

Lastly, using SEM to characterize the morphology of the PANI electropolymerized on the different films also showed the high surface area gold electrodes to perform more similarly to the CP electrodes than planar gold. While the films did not exhibit is much distinct high surface area fibril morphology observed on the CP electrodes, the

morphology was more granular with higher surface area than the globular morphology observed on planar gold, suggesting improved conductivity.

4.4 Conclusion

Carbon paper was successfully utilized as an all-carbon, low-cost alternative to inorganic electrodes in conventional PSI-based biohybrid photoelectrochemical cells for mediator-driven solar energy conversion. Prior to use, it is critical to pretreat CP substrates in order to maximize the accessible surface area through both the removal of any protective coating and the creation of hydrophilic moieties on the fiber's surface. Simple treatments such as soaking in acid solutions or exposure to an open flame proved effective, with flame treatment improving the electrochemically active surface area by a factor of roughly 10 for Faradaic processes. PSI vacuum deposited on flame treated CP produced a consistent anodic photocurrent (0.11 μA cm^{-2}) using a ubiquinone mediator. More stable photoactive composites can be formed by entrapping PSI within an electropolymerized composite, which capitalizes on the improved CP electrode surface area following pretreatment. Using cyclic voltammetry as a polymerization method, the produced photocurrent densities could be pushed to 0.22 μA cm^{-2} under the conditions tested in this study. Further, Carbon paper electrodes improved the performance of electropolymerized PANI/PSI films by increasing the amount of active layer produced, increasing the concentration of PSI within the films, and improving the conductivity of the polymers produced. Further study suggest these gains can be accomplished with other high surface area electrodes materials, and that a reflective material may produce even greater results. These methods can be readily employed to upscale the size of the produced photoactive electrode beyond benchtop dimensions.

CHAPTER 5

Design of Solid-State Biohybrid Photovoltaics

This chapter will describe the effort to design functional PSI based solid-state photovoltaics, using carbon paper electrodes, and conductive polymers. To date, no other PSI solid-state devices with carbon paper electrodes have been reported within the literature. In addition to this novelty, these design efforts aim to improve certain key performance attributes, like scalability, low cost, and low environmental impact, while not necessarily optimizing performance. This was a truly iterative process, and while not all versions of the design are reported, the goal is to demonstrate an initial functional design that can be improved upon with additional research. This work was completed with the support of Dr. Chris Stachurski, Matthew Galazzo, Elisabeth Wood, and Dr. Kody Wolfe.

5.1 Introduction

The need for clean, cheap, and reliable energy has been a driving force in research for some time, though recent economic, political, and environmental concerns have increased the urgency. Photovoltaics offer a means of using the sun to produce reliable energy, leveraging the photocatalytic effect in materials to use light to drive the flow of electrons. This field of research has been dominated by the use of wide band gap semiconductors, like silicon, doped to prefer certain charge carriers, and aligned to allow those carriers to flow[35]. This model is theorized to have an upper limit at 30% efficiency, however, research on novel semiconductors, multi-junction cells, and the use of concentrators are continuing to drive the efficiency forward[60,65]. The breakthrough study by Gratzel in 1989 introduced a new design for photovoltaics, the dye sensitized solar cell[32]. This design still possessed the wide band gap semiconductor, in the form of TiO_2 nanoparticle, sintered

onto a transparent conductive metal oxide glass slide, and added an organic die to attach to those nanoparticles. The dye would absorb photons at a particular wavelength and transfer excited electrons directly to the conduction band of the TiO_2. The source of the electrons was an ionic fluid with a reversible redox pair, like I_2/I_3^-, that could donate electrons to the dye and be replenished at the carbon cathode. This design led to more advancements with improved dye designs, more efficient ionic fluids, and innovations in TiO_2 nanoparticle application. While the design offered a new, cheaper photovoltaic, the systems were not as efficient as silicon based devices, and the risk of photovoltaics losing the toxic fluids, either through leaking or evaporation, made them less practical[34,35]. This led to other innovations, like solid state dye sensitized solar cells, organic photovoltaics, and perovskite solar cells, collectively grouped by the National Renewable Energy Laboratory (NREL) as emerging photovoltaics[35].

A common theme among the emerging photovoltaics is the use of energetically aligned novel materials to transfer charge. This can include conductive polymers both in the active layer and serving as direct carrier transfer layers, like PEDOT:PSS or polyaniline. This can also include novel materials like organic metal halides called perovskites, with adjustable band gaps, that can more efficiently achieve charge separation. Materials selected for electrodes are often determined by the work function, to ensure alignment throughout the system, and to maximize the potential of the device. Much of the current research in emerging photovoltaics is focused on improving manufacturing processes, that will both reduce the cost of the device, and the cost of the energy produced[34,35]. Additionally, improvements that encapsulate the system, and reduce interface impedance improve the longevity and efficiency of the device, again reducing the cost of the energy produced[68,74,75]. These systems are currently a leading effort in photovoltaic research,

however, to date, they have not yet overcome the efficiency of the best performing solid state semicrystalline solar cells.

Another class of photovoltaics leverages the machinery of photosynthesis to create a flow of electrons. Biohybrid photovoltaic research has been conducted around the world over the last 50 years, using whole thylakoids, or one of the two major membrane bound proteins within the photosynthetic process: Photosystem I (PSI) and Photosystem II (PSII)[20,21,131]. Photosystem I is a roughly 500 kDa protein found within plants, algae and some photosynthetic cyanobacteria, predominately composed of chlorophyll arrays surrounding an electron transport chain. The chain begins at a chlorophyl dimer designated as the p700 site, where the energy of photons collected by the chlorophylls is used to excite electrons, through a series of phylloquinone mediators, through three iron-sulfur complexes, culminating at the F_B site where it is transferred with roughly 1.1eV of additional energy[80-88]. The process can happen in a fraction of a second, across a distance of 10nm with efficiency that approaches unity. Within the process of photosynthesis, the proteins use absorbed light to create an exciton pair, and drive electron transport across the thylakoid membrane with the help of diffusional mediators, in order to create chemical energy. Likewise, within biohybrid photovoltaics, the protein is used within the active layer to drive charge carrier generation. While biohybrids have not demonstrated the same efficiency as other emerging photovoltaics, the advantage of these systems is the ubiquitous and renewable supply of photodiode material. The use of plant proteins can dramatically lower the cost of the devices, while also reducing the environmental impact, both of which are desirable traits in next generation energy development[89].

This field has benefitted from the advances of other emerging photovoltaics, taking advantage of the application of conductive polymers to not only serve as direct charge

transfer materials, but preserving the protein in a functional conformation within the polymer film. In a 2015 paper, Gizzie et al published a design for a solid-state device, where the active layer of polyaniline (PANI) and PSI was electropolymerized directly onto the anode, with an evaporated metal serving as the cathode[120]. This study demonstrated the feasibility of a solid state photovoltaic, along with the importance of band alignment while building a layered device. This study aims to build on this success by designing another solid state biohybrid photovoltaic, utilizing a PANI/PSI active layer, but introducing new materials and fabrication techniques to reduce cost.

5.2 Experimental

5.2.1 Anode Preparation

Transparent glass slides, coated with Indium doped Tin Oxide (ITO) were cut into 2.5 cm x 1 cm samples. The samples were cleaned through a series of 15 min sonication baths in acetone, ethanol, and DI water respectively, followed by 15 minutes of plasma treatment within a PDC-32G plasma cleaner/sterilizer.

Two methods were used to create a compact TiO_2 blocking layer directly onto the conductive ITO. For both methods, samples were masked to ensure an unblocked ITO lead and a $1cm^2$ active area for the anode. The first method sputtered a 30nm layer of TiO_x, at a rate of .5 nm/min, using an AMAJ multimode deposition chamber, then annealed on a hotplate at 500 ^oC for 1 hour. The second method adopted a protocol from Su et al and electrodeposited TiO_2 with a three electrode set-up within a CHI 660 workstation, using a platinum mesh counter electrode, and an Ag/AgCl (sat KCl) reference electrode[197]. The electrodeposition solution was a 50 mM $TiCl_3$ solution, raised to a pH of 2.5 with NaHCO3, and purged of oxygen with nitrogen gas. The working electrode was held at

1.1v for 600s. Electrodes were rinsed with DI water and dried under air.

Cyclic voltammetry was used to determine the effective blocking of ITO electrodes. Cleaned ITO electrodes were masked, limiting the exposed electroactive surface area to a circular .71cm^2. CVs were conduct with RuHex before and after electrodeposition of the blocking layer to allow for comparison. XRD was used to confirm the blocking layer produced from both methods was TiO_2.

A dense suspension of TiO_2 nanoparticles was then electrosprayed onto the dry anode surface based on a protocol adopted from Zhu et al[43]. The suspension was composed of 6g of Anatase TiO_2 nanoparticles (>25nm), 8g ethylene glycol, and 1g acetic acid (normal). The suspension was magnetically stirred for 12 hours prior to use. The suspension was loaded within a 1ml syringe and pumped at a rate of 50μl/hr into an 18G stainless steel needle. The needle was held at 10.5 kV by a BA model 205A-20R high voltage power supply, at a height of 4cm above the anodes. The anodes were staged on at hot plate at 125^o C and connected to the power supply ground. Samples were masked to ensure an unblocked lead of ITO, and a 1cm^2 active area of anode surface. The system sprayed each anode until a thin even coat of TiO_2 np was applied (3 min). Samples were then removed from the electrospraying system and allowed to sinter on a hot plate at 500^o C for 3 hours, observing the color change from pale-white, to dark-brown, and finally bright-white. Anodes were allowed to gradually cool to room temperature prior to further use. XRD was used to ensure the anatase conformation of TiO_2 remained. Scanning electron microscopy was used to evaluate the structure of the NP layer, and profilometry was used to measure the average thickness.

Polyviologen(PV) was synthesized based on a protocol adapted from Do et al. Equimolar ratios of 4,4'-bipyridyl and 4-dibromodecane were mixed in dried N,N-

dimethylformamide (DMF). The mixture was magnetically stirred, under reflux, at 110^{o} C for 12 hours. The resulting powder was washed and filtered under vacuum with N-hexane and dichloromethane. The remaining yellow product was dried under vacuum, weighed and characterized with Fourier Transfer Infrared-Red spectroscopy (FTIR), cyclic voltammetry, and nuclear magnetic resonance. A sample of PV was dissolved within DI water to produce a 10mg/ml solution. 80μl of solution was applied directly onto the TiO_2 np surface and allowed to dry under vacuum for 1 hour.

For some devices a monolayer of PSI solution was added to the anode. 200μl of solution was pipetted directly onto the active area and allowed to dry under vacuum for 1 hour.

Polyaniline nanofibers were electrospun from a solution of emeraldine salt and camphor sulfonic acid in equal molar ratio dissolved within chloroform. Polyethylene oxide (PEO) was added as a copolymer (2% w/v), and the solution was magnetically stirred for 12 hours. The solution was pumped through a stainless steel 22G needle at a rate of 1ml/hr. A potential of 15kV was applied to the needle, and the substrate, set 12 cm below the needle, was connected to the power supply ground. Thin layers of PANI/CSA fibers were electrospun directly onto some iterations of anodes and cathodes to reduce interface impedance.

5.2.2 Cathode Preparation

Carbon Paper cathodes were prepared as described in previous studies from our group[120,122]. T-60 Toray carbon paper was flame treated for 10s, ensuring complete coverage, and observing a slight color change from dark to dull grey. The carbon paper was then cut into 1cm x 2cm samples and masked with tape to leave 1cm^2 of exposed

geometric surface area. A small strip of carbon tape adhesive was added to provide mechanical support to the carbon paper electrode lead.

Polyaniline films were electropolymerized directly onto CP electrodes using a three electrode set-up within a CHI 660 electrochemical workstation with associated software, using an Ag/AgCl (sat KCl) reference, and a platinum mesh counter electrode. The electropolymerization solution (1M aniline, .946 M HCl, and .004 M Na_3PO_4) was combined with eluted PSI solution (1μM) in a 4:1 ratio. The working electrode was held at 1.2v for 60 or 90s, then allowed to dry under vacuum for 1 hr.

Solid state devices were assembled so that the $1cm^2$ active area of the cathode was in direct contact with the $1cm^2$ active area of the anode, with electrode leads pointing in opposite directions. The systems were sandwiched between glass microscope slides and secured with rubber bands to maintain constant and even pressure. Devices were then evaluated for open circuit potential, V_{oc}, photocurrent density, *j*, and i-v curves, where the anode served as the working electrode.

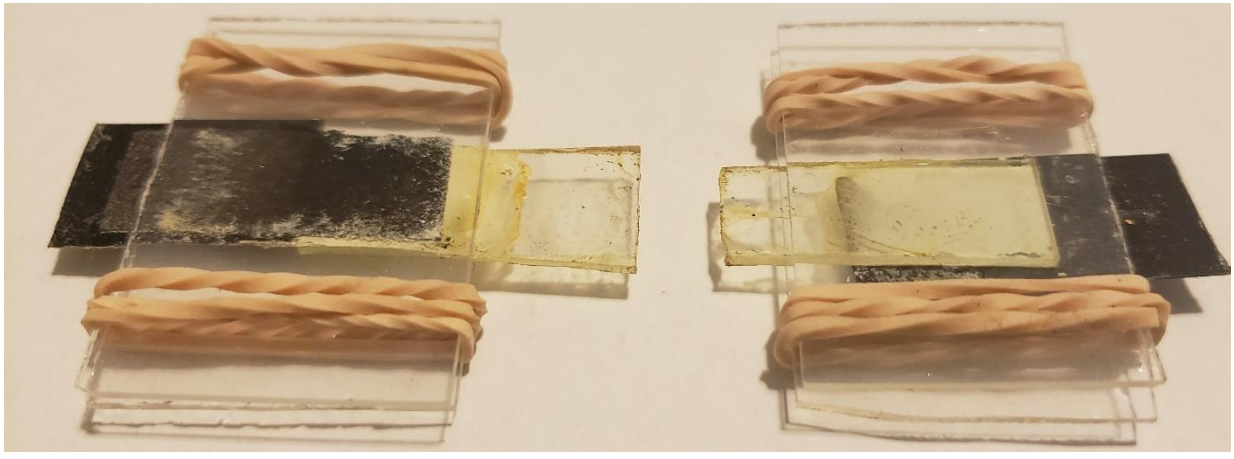

Figure 5.1 Assembled biohybrid photovoltaics, top and bottom view

5.3 Results & Discussion

The initial goal of this research was to replicate our previous work, using an electropolymerized PANI/PSI active layer within a functional solid state device, demonstrating both photocurrent and open circuit potential. This study hoped to replace the evaporated metal cathode with a high surface area carbon paper electrode, introducing greater scalability and reduced cost to each device. Additionally, this study aimed to leverage the advantages of electropolymerizing PANI/PSI directly onto the CP electrodes, namely increased loading of PANI/PSI, and improved conductivity of the PANI film. These adjustments introduced a number of new challenges to the devices. In the previous study, the active layer was electrodeposited directly onto the TiO_2 np, and the metal cathodes were evaporated directly onto the active layer. This design maximized the active surface area of TiO_2 used and minimized impedance. In contrast, electropolymerizing the active layer directly onto the cathode meant these devices would need to be assembled, introducing increased interface impedance between layers. Additionally, while the PANI/PSI active layer was still flexible and able to change shape with appropriate pressure, the assembled device would not likely contact all of the TiO_2 np, creating air gaps and recombination traps that would decrease performance, and reduce open circuit potential[69]. To address these issues, and others, an iterative approach to designing and testing new devices was applied.

The earliest iteration electropolymerized PANI/PSI active layers on CP and planar gold electrodes. Devices were then assembled using anodes prepared for use in DSSCs. The anodes were ITO coated glass slides, with a thin layer of TiO_2 np produced via sol-gel techniques, applied through spin coating, and sintered at 500^o C. The cathodes were masked to control the exposed surface area and the two electrodes were sandwiched

between two glass slides and held in place with standard office binder clips. A small plastic spacer was added between the cathode and glass slide to ensure contact between the exposed PANI/PSI film and the anode. While the planar gold devices were functional, demonstrating a minimal V_{oc} and photocurrent near 10 nA/cm2, no devices with CP cathodes demonstrated photocurrent, or V_{oc} of at least 1mv. This led to a layer by layer approach to improving the system design.

5.3.1 Open-Circuit Potential

The primary issue to address was the lack of open circuit potential within assembled devices. The open circuit potential is the maximum voltage a solar device can provide to an external circuit under steady illumination. This value describes the potential difference during quasi-equilibrium where photo-derived charge carriers accumulate at the cathode and anode, while the rates of charge carrier generation and recombination are relatively equal[69]. In general, the value is related to the difference between the highest occupied molecular orbital (HOMO) of the electron donating material and the lowest unoccupied molecular orbital (LUMO) of the accepting material. In traditional photovoltaics, like those based on silicon P-N junctions, the open circuit potential is generally the difference between the fermi levels of the positive and negative regions, or the band gap of the semiconductor. In less ordered systems, like amorphous silicon, and most organic photovoltaics, gap states can decrease the average energy level of the HOMO, and increasing the average energy level of the LUMO, decreasing the V_{oc}[34,35,56,69]. In this study, the charge separation occurs within the PSI protein, and the conductive polyaniline which entrapped the protein, was responsible for transporting the charge carriers from the

protein to the respective electrodes, serving as both the electron donor acceptor within the system. The high surface area morphology of intertwined PANI fibrils created ample opportunity for recombination of charge carriers within the active layer. This is an issue often observed in organic photovoltaics, but can be addressed, both with adjustments to the crystallinity of the PANI/PSI film, as well as additional layers within the device to improve charge transfer from the polymer and reduce recombination at the electrode surface[69].

5.3.2 Band Diagram

The performance of these devices are dependent upon the alignment of the various layers, and the efficiency of charge transfer. The charge separation occurs within the active layer of a PANI/PSI film as well as the PSI monolayer. Charge separation at the P700 site drives excited electrons through the electron transport chain, culminating at the F_B site. The PANI film acts as a solid state charge transfer material, leveraging charge hopping along its aromatic backbone to shuttle excited electrons away from the protein. The holes created at the P700 site are similarly transferred through the PANI to the carbon paper cathode. The work function of the carbon paper, estimated near -4.6 eV vs vacuum, was readily able to receive holes as it is energetically higher than the protein P700 site[172]. The layer of polyviologen, with a redox potential at roughly -4.01 eV, provides a redox polymer to serve as an efficient electron transfer material from active layer to the conduction band of the TiO_2 np, at roughly -4.2eV vs vacuum[198]. The illuminated np would then transfer the electrons through the blocking layer, and to the conductive ITO surface. (Figure 5.2)

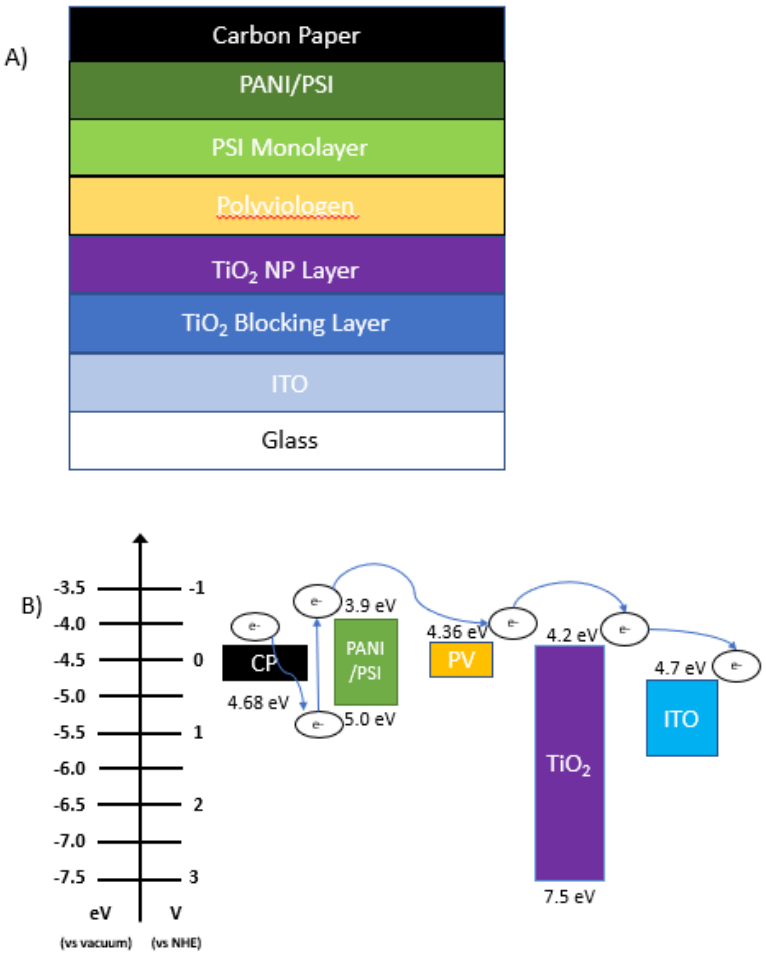

Figure 5.2 Schematic of biohybrid device, and ideal energetic pathway of electrons within the device.

5.3.3 Device Performance

The performance of functional assembled devices was characterized with linear sweep voltammetry in both illuminated and dark conditions, resulting in i-v curves of CP/PANI/PSI devices and CP/PANI only controls (Figure 5.3). For this study, functional devices were required to demonstrate potential greater than 1mv both in the dark and illuminated. A measured potential in the dark demonstrates the devices does not include a short circuit. CP/PANI/PSI systems demonstrated a V_{oc} greater than 470mv, J_{sc} of 80nA/cm^2, a maximum power point (MPP) of 12.8nW and fill factor of .34. In contrast

CP/PANI only controls demonstrated V_{oc} of 144mv, J_{sc} of 18nA/cm2 and an MPP of .934nW, owing its performance in part to the photoactivity of PANI in the active layer. While these results demonstrate a stark decrease in performance compared to previously reported PSI based devices, the design parameters have not yet been optimized. Various factors, like the thickness of the active layer, the polymer annealing temperature, the amount of polyviologen applied, the thickness of the TiO_2 np layer, and the blocking layer thickness can all be adjusted to improve interfaces, maximize light absorbed, reduce resistance, and maximize performance. To date, these are the first functional PSI based solid state photovoltaics to utilize a carbon paper electrode.

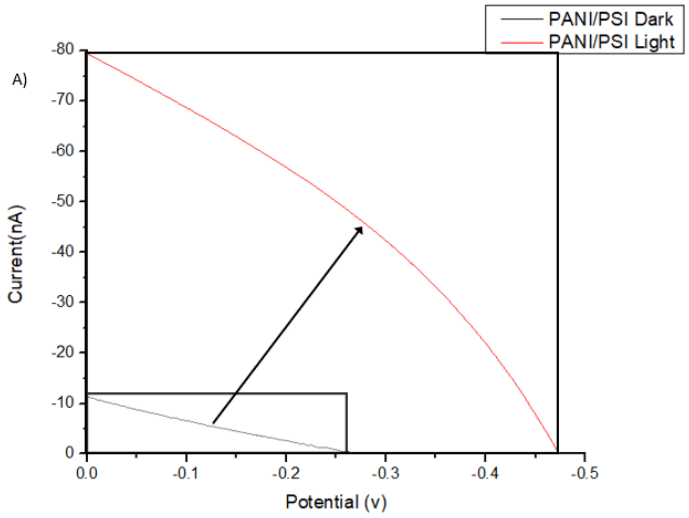

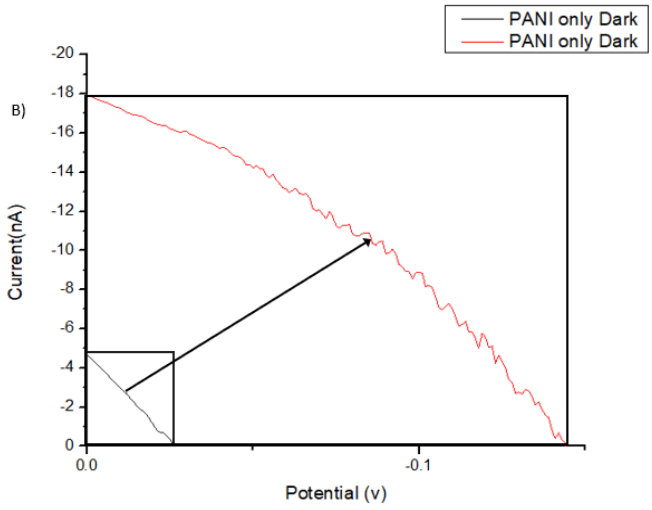

Figure 5.3 Representative i-V curves of (A) PANI/PSI biohybrid device and (B) PANI only control device.

Of the approximately 250 solid state devices assembled with various combinations of CP/PANI/PSI, less than 20 devices demonstrated both V_{oc} and photocurrent, with the design reported above providing the most functional systems. The maximum V_{oc} observed was .534v with an average at .333v. These values are similar to the Voc reported in literature from other emerging solid state photovoltaics. The maximum photocurrent density recorded from devices was .899$\mu A/cm^2$, with an average of .167 $\mu A/cm^2$ which is in line with some other current PSI based photovoltaics, but orders of magnitude lower than the best performing systems, and well below other emerging photovoltaics like PSCs. This result may be the most addressable problem as improvements in device assembly, and layer thickness optimization will likely reduce impedance and increase the flow of charge carriers within the system.

5.3.4 Blocking layer

Figure 5.4 ITO anode with sputtered 30nm TiO_x Blocking layer

A thin compact semiconductor blocking layer provides a critical gate within the photovoltaic device, preventing shorts and reducing recombination at the electrode surface. Literature suggest different methods of producing an effective layer of TiO_2 directly onto the ITO anode surface, including sputtering of TiO_x, spin-coating a TiO_2 precursor, electrodeposition, and atomic layer deposition[37-42]. The literature also suggest different optimal thicknesses based on the method of production, balancing the increased charge transfer resistance of thicker layers, and the possibility of pinholes or fissures in thinner layers. This group was able to produce TiO_2 blocking layers through sputtering, electrodeposition, spin coating and chemical bath. Sputtering was the most consistent method, as the deposition was monitored digitally, creating a uniform 30nm layer of TiO_x at a rate of .5nm a minute(Figure5.4). Electrodeposition was a more complex procedure, and dependent on a fresh deposition solution, at the appropriate pH, and purged of oxygen gas during the process. The process is based on the anodic oxidative hydrolysis of $TiCl_3$ in an acidic solution:

$$Ti^{3+} + H_2O \longrightarrow TiOH^{2+} + H^+$$

$$TiOH^{2+} + H_2O - e^- \longrightarrow TiO_2 + 3H^+$$

The reduced cost of materials, and consistency of the blocking layers produced suggest this method may be more ideal for future manufactured devices. The resulting blocking layers from spin-coated precursors or chemical baths based on $TiCl_4$ were less consistent, compact, or uniform compared to either sputtering or electrodeposition, though these processes were the simplest, cheapest, and most scalable methods.

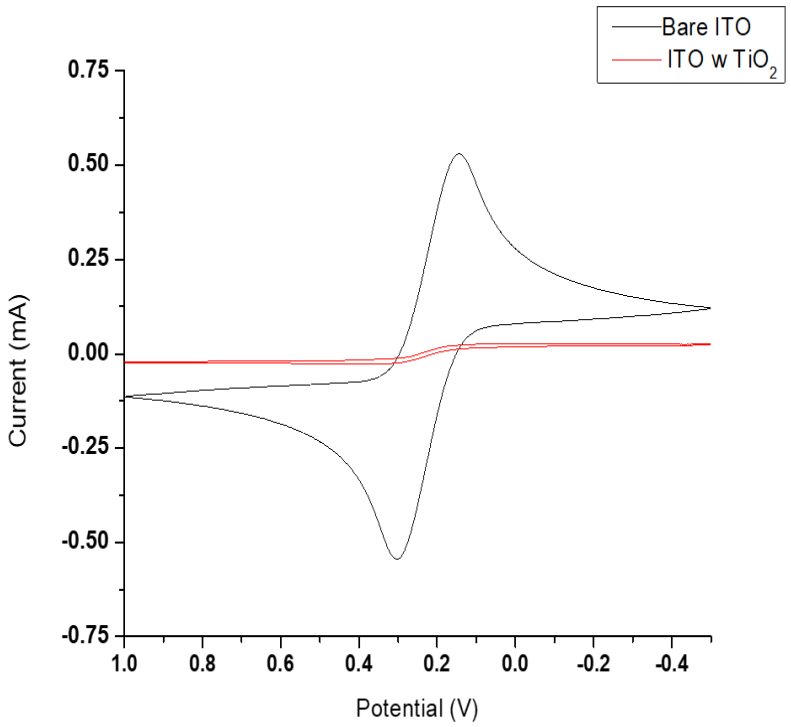

Figure 5.5 CVs of RuHex using masked ITO anodes as the working electrode show the effect of electrodeposited TiO_2 blocking layer.

The effectiveness of the blocking layer is characterized via CV, using a controlled surface area and a known redox pair(Figure5.5). The peak current density observed in the CV, Ip , is directly proportional to the area of the electrode, as described by the Randles-Servcik equation. Comparing the Ip observed on bare ITO electrodes and the ITO electrodes after electrodeposition, should describe how much of the electrode surface area was effectively blocked, as all other factors remained equal. Electrodeposition of 600s produced a 95% reduction in Ip, and the sigmoidal shape and broad peaks of the blocked CV suggest the blocking layer is compact, and the signal observed is due to electron hopping through the layer rather than a direct interaction with the electrode surface area. The shape may also indicate the presence of some structural defect like pinholes, that may allow for recombination within the blocking layer if the layer was formed too thick[199].

These results are in line with those observed by Su et al whose original protocol was adapted for this research[197]. XRD of the compact crystalline layers on ITO slides demonstrated peaks associated with anatase TiO_2, regardless of the method of preparation, though some peak spreading was observed, and is associated with the thin, compact, and highly ordered crystalline layer.(Figure 5.6)

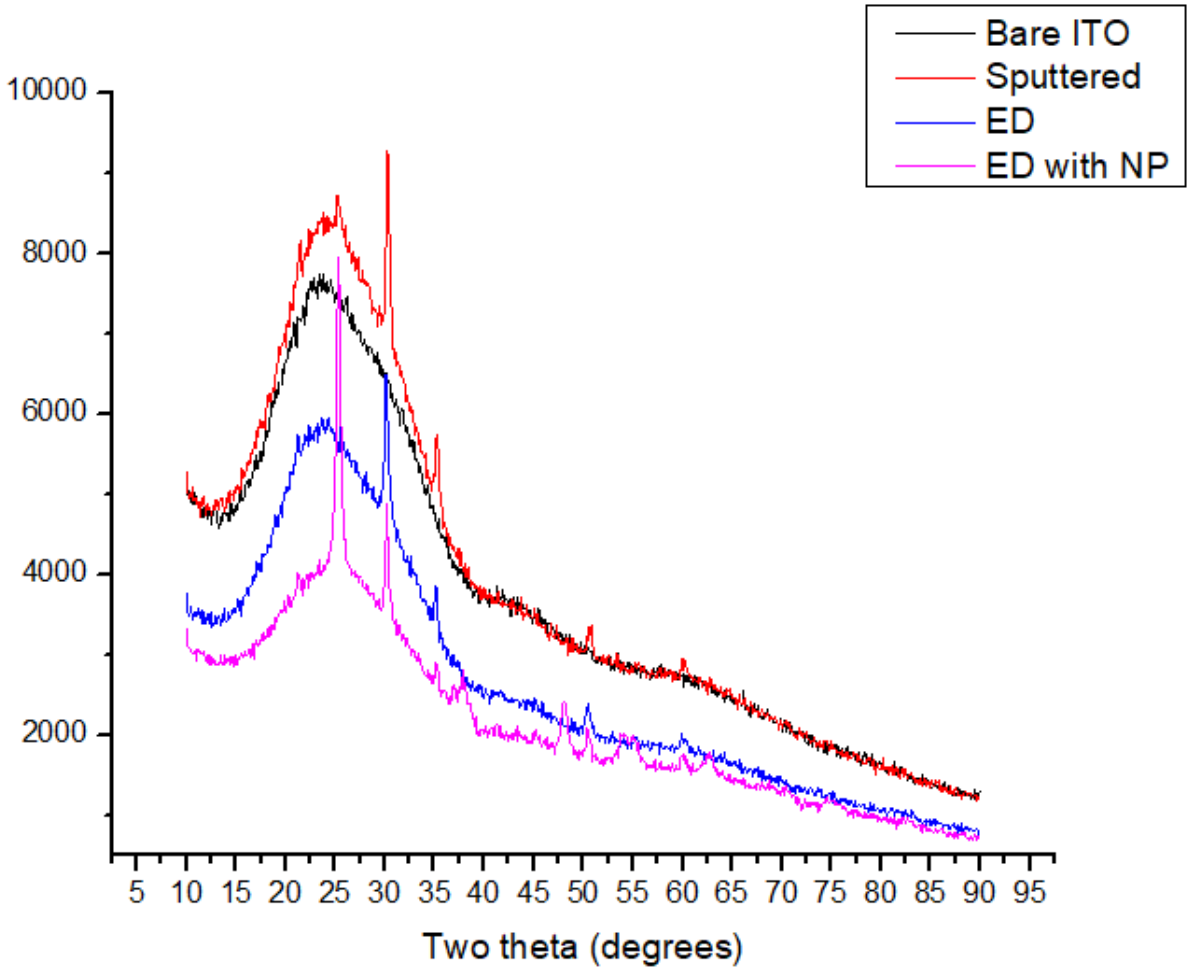

Figure 5.6 Overlayed XRD of bare ITO, ITO with sputtered TiO_x, ITO with ED TiO_2, and ITO with ED TiO_2 and electrosprayed TiO_2 np.

5.3.5 TiO_2 NP Layer

TiO_2 nanoparticles have been a nearly ubiquitous aspect of modern photovoltaics, especially within DSSC research[200-208]. The semiconductor has high stability, low cost, and minimal risk to the environment. Both the rutile and anatase conformations have solar

application, though for many, anatase is preferred due to the slightly larger band gap, increased carrier mobility, and smaller particles compared to rutile, making it very efficient for photoactivity[201,208]. The use of nanoparticles increases the electroactive surface area available for charge transfer, and in most DSSC, various dyes are attached directly to the TiO_2 nanoparticles[24,205]. Three dimensional hierarchical structures maximize the amount of dye that can be loaded within the system, increasing the light that can be absorbed, and the charge carriers that can be generated. Both the source of TiO_2 nanoparticles, and their method of application can create complications within the device.

This group previously leveraged a sol-gel technique with a Titanium alkoxide precursor to synthesize the nanoparticles and used spin coating or dipping to apply the particles directly onto ITO and FTO slides[205]. Commercial paste of TiO_2 nanoparticles are available for purchase specifically for the production of photovoltaics, however the quality, cost, and availability can vary over time, which may not be ideal for reproducible results[44]. The traditional methods of applying these pastes often call for a dilution with ethanol, followed by spin coating or doctor blading. The density of nanoparticles on the anode surface is dependent on the dilution of the paste, as well as the speed of rotation. These methods are effective in providing an evenly distributed layer of nanoparticles across the area of the electrode, maintaining enough transparency to maximize the amount of light absorbed, though pinholes and fissures can occur during or after sintering[44]. These methods are limited though, in their ability to produce vertical three dimensional structures.

Electrospraying provides an effective means to produce stacked three dimensional features of TiO_2 nanoparticles on the electrode surface. The ethylene glycol provided the high viscosity necessary to maintain a well-defined Taylor cone under high voltage, while the normal acetic acid improved the conductivity of the paste. The ITO surface of the

anodes were masked with a conductive tape to both maintain a lead for the electrode, and ensure the conductive surface was connected to the grounding wire of the power supply. The slow flow rate and high voltage produced a fine mist of TiO_2 nanoparticles being drawn, vertically, to the surface of the electrode. The three dimensional structures were confirmed through SEM, and profilometry confirmed and average height of 25 μm(Figure5.7). While these structures were stable, they demonstrated some fragility under high pressure, even after sintering at 500^o C. XRD spectra demonstrate the electrosprayed TiO_2 np layer maintained the anatase conformational peaks.

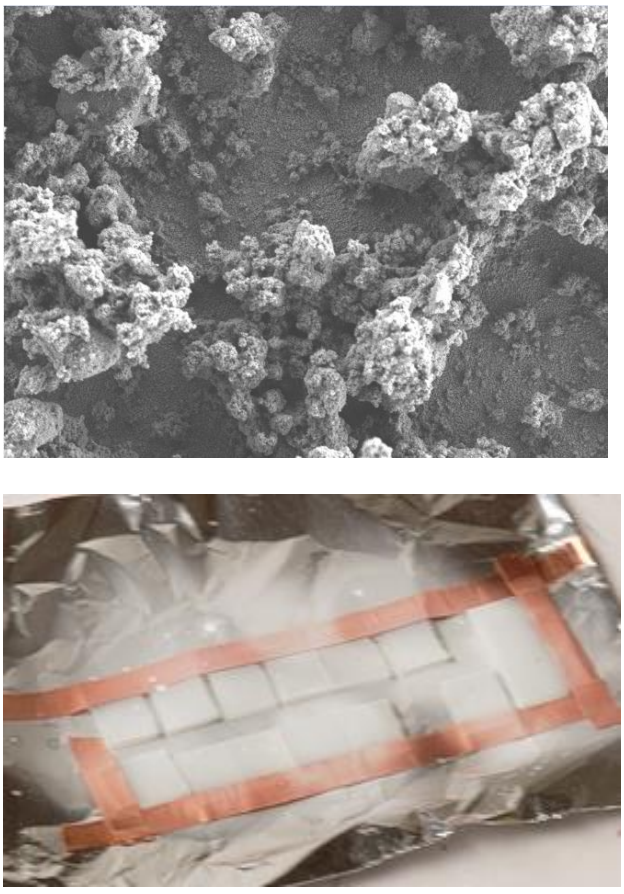

Figure 5.7 SEM of TiO_2 nanoparticle layer showing vertical three dimensional structure. Image of anodes after electrospray TiO_2 nanoparticles, prior to sintering.

5.3.6 Electron Transport Material Layer

In order to take advantage of the high surface area of the nanoparticles, an additional electron transfer material layer was added to the anode. This material needed to be flexible

enough to fill the spaces created within the three dimensional structures of the nanoparticles, with a redox potential between the F_B site of the active layer and the conductive band of TiO_2. Early iterations attempted to electrospin nanofibers of PANI directly onto the anode surface, in order to reduce impedance at the interface between the anode and the active layer film(Figure 5.8). This method was effective in producing conductive PANI fibers, though the mechanical properties were limited and largely dependent on the amount of PEO within the solution, where more conductive solutions, with a lower weight percent of copolymer, often resulted in electrosprayed PANI rather than discernable fibers. While early devices demonstrated increased photocurrent with the application of PANI/CSA, the devices did not consistently produce systems that demonstrated $V_{OC.}$ This suggest the material, while conductive, may not have been energetically aligned to serve as an effective electron transport material. A number of studies have shown its application as an effective hole transport material in other solid state photovoltaics.

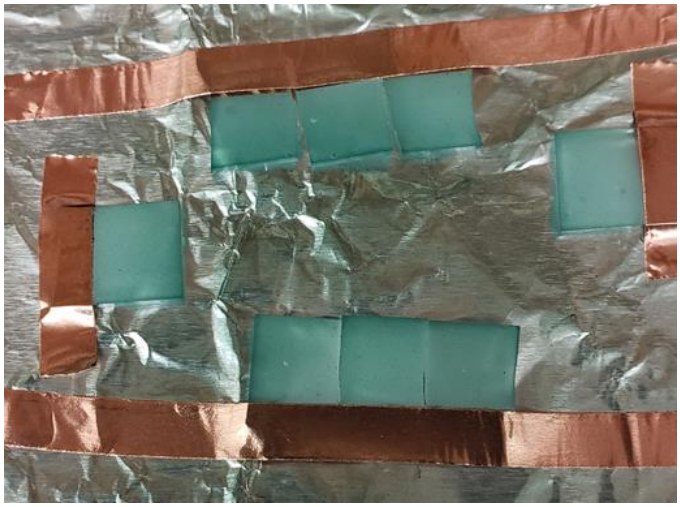

Figure 5.8 Anodes with electrospun PANI/CSA fibers directly onto the TiO2 np layer.

Methyl Viologen (MV) is often used as a diffusional mediator with PSI based systems,

acting as an electron acceptor from the F_B site of the protein[102,209,210]. Ward et al previously demonstrated the improved photocatalytic effect of a solution of TiO_2 nanoparticles by adding MV to the electrochemical wet cell, suggesting the molecule is energetically aligned to efficiently transfer electrons to the nanoparticles in a diffusional state[209]. Our lab has recently published a study by Dervishogullari et al where the redox polymer polyviologen, synthesized from bipyridyl and xylene, served as an effective electron transfer material between PSI monolayers and an ITO anode[129]. Do et al demonstrated the impact of counter ions used with polyviologens to adjust the redox potential of the polymer for better energetic alignment within photovoltaics[198].

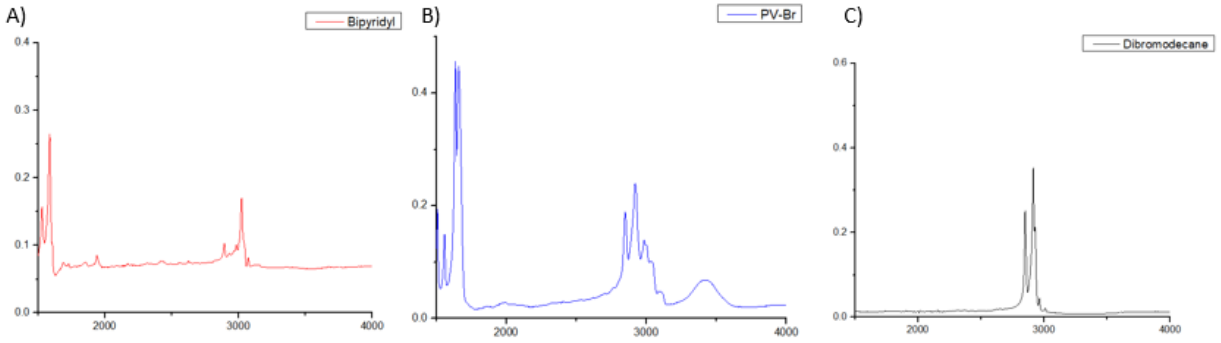

Figure 5.9 FTIR of (A) Bipyridyl, (B) synthesized PV-Br, and (C) Dibromodecane

This study adopted the protocol used by Do to synthesize poly(1,1'-didodecyl1-4,4'bipyridinium dibromide) (PV-Br) as the reported work function, -4.01eV vs vacuum, fell between the F_B site of PSI and the conduction band of TiO_2. The synthesis produced a high yield of bright yellow powder, which was readily dissolved in DI water for both characterization and application. FTIR reveals the polymer possesses the aromatic stretching peaks from the bipyridyl near wavenumbers 1500 and 3000, while also showing increased alkane peaks near wavenumber 3000 from the dibromodecane.(Figure 5.9) The CV of the PV-Br solution demonstrated reduction and oxidation peaks with an $E_{1/2}$ at

-.341v vs Ag/AgCl (Sat KCl) as expected(Figure 5.10). Devices assembled with the vacuum-deposited PV-Br applied directly to the anode consistently produced both Voc and photocurrent, in contrast to the previous iteration, while control devices without the polymer layer produced neither. The improvement in observed V_{oc} could be attributed to improved band alignment, improved efficiency of charge transfer away from the active layer, or a reduction of trap states within the TiO_2 np layer.

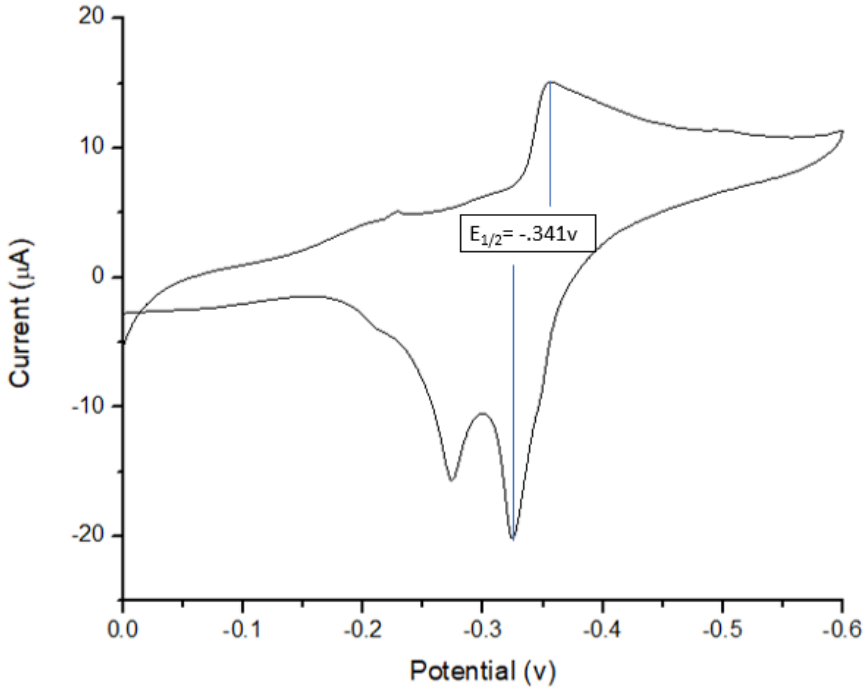

Figure 5.10 CV of a 10mg/ml solution of synthesized PV-Br, using a glassy carbon electrode.

5.3.7 PANI/PSI Active Layer

The effort to produce cathodes from carbon paper, conductive polymer, and PSI that would consistently result in functional devices was iterative in nature. While planar electrodes, like gold, and heavily doped silicon would readily produce functional solid state devices with the anodes as prepared, the high surface area CP electrodes would often not demonstrate V_{oc}, with and without the PANI film. This suggested the rate of

recombination within the carbon paper electrode and active layer was greater than rate of charge carrier generation. To overcome this issue a number of different device designs were applied to adjust the properties of the active layer. While some of these designs did produce functional devices, it was not until the addition of PV-Br to the anode that device performance was consistent and repeatable. For those devices PANI/PSI films were electropolymerized potentiostatically, for 60 seconds.

One of the first efforts to improve cathode design was to increase polymerization time. The previous study on carbon paper electrodes demonstrated that as polymerization time increased, the photocurrent from the PANI/PSI film increased, as the high surface area CP electrode could load more polymer and protein over time. Additionally, with increased time, the PANI demonstrates increased conductivity, and its own photoactivity would contribute to the performance of the device. PCA of early solid state devices, without Voc, saw photocurrent increase with increased polymerization time. Other efforts attempted to change the oxidation state of the PANI within the film by holding it a potential within a solution of HCl. The conformation of PANI can be changed with potential in the presence of a strong acid, protonating and deprotonating the polymer chain[163]. This change can be observed in the color of the film shifting between a dark black and a bright blue green hue. The goal was to determine if the less conductive version of the polymer would limit recombination within the active layer, while still supporting the charge transfer for the entangled protein. The graphs of these efforts show the increasing resistance with time, reaching an almost insulating state after roughly 15s at -.8v(Figure 5.11). Unfortunately, this change did not produce functional devices with V_{oc}. Additional cathodes were designed with a mix of dynamic and potentiostatic electropolymerization. This effort was to change the morphology of the PANI film to reduce recombination at the electrode

surface, while maintaining a conductive and robust PANI/PSI active layer. The immediate results were evident during the static electropolymerization, as the shape of static polymerization changed. This process produced some functional devices; however, the results were not consistent.

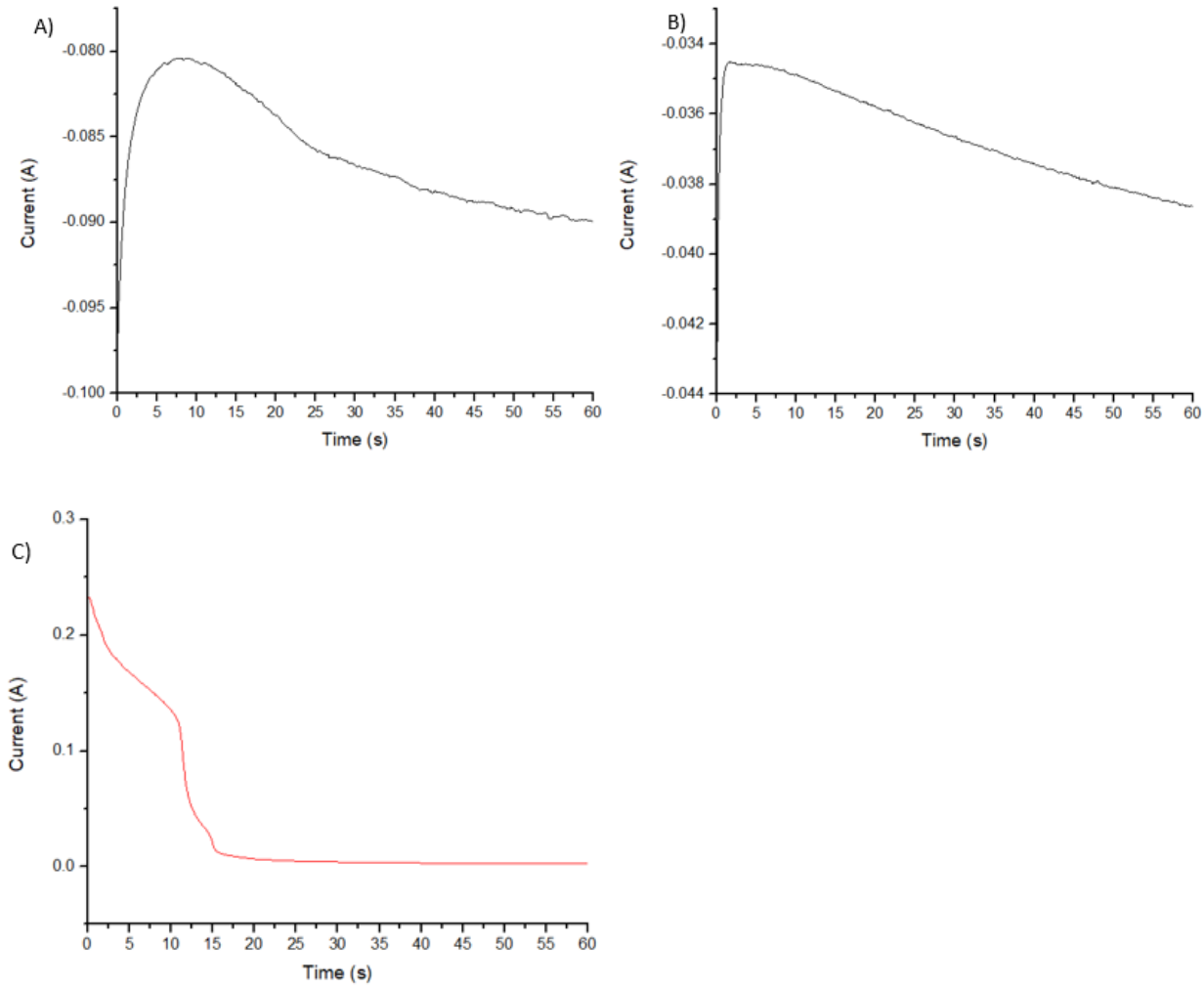

Figure 5.11 Amperometric i-t curves of potentiostatic electropolymerization of PANI on CP electrodes. (A) shows standard electropolymerization while (B) is potentiostatic after 30cycles of potentiodynamic electropolymerization. (C) shows the i-t curve of a PANI film on a CP electrode held at constant potential within a 1M solution of HCl

5.3.8 Follow on Efforts

In addition to further characterization and optimization of this design, our group has begun additional work to further the impact of this research. Scalability is an important

performance parameter that would allow this design to be used for more applications. The carbon paper adds some modicum of scalability given its commercial availability in a wide spectrum of sizes. The fabrication techniques used in this research are being evaluated on their effectiveness with larger substrates, namely the electropolymerization and electrodeposition steps, as both can be hindered by the size and shape of the electric fields used within the potentiostat. In some early efforts, electropolymerization on large carbon paper electrodes (2 cm^2, $4cm^2$) is limited to the outer edges of the electrode, not evenly covering the surface. Additionally, preliminary work has shown that scaling the polymerization time in proportion to the change in geometric surface area is not sufficient to maintain similar properties in the electrodes. Scaling the charge delivered during polymerization by the change in electrochemically active surface area has been more effective, though much more research is needed in this effort.

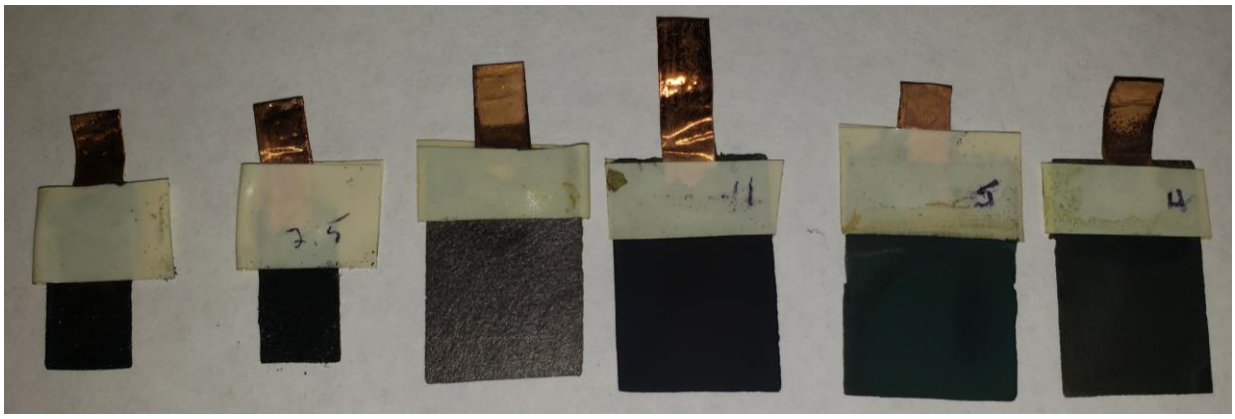

Figure 5.13 CP electrodes of different sizes ($1cm^2$ and $4cm^2$) with electropolymerized PANI films

Another modification to the design with initial results include the application of Cytochrome C within the solid state device. The current device design leverages the conductive polymer PANI to entrap the PSI protein, while both donating electrons to the P700 site and accepting electrons from the F_B site. This arrangement and distribution of

proteins throughout the active layer may increase the chances for recombination. The addition of PV-Br as an electron transfer material provided an efficient means of exchanging excited electrons from the active layer to the TiO_2 np layer. A second mediator, at the P700 site may also improve performance of the system. Baker et al used $Os(bpy)_2Cl_2$, entrapped with PSI within a Nafion solution, leveraging a charge hopping mechanism to scavenge holes from the P700 site of PSI, and demonstrated the role of a solid state mediator in improving the photocurrent of PSI devices[27]. Similarly, redox proteins like Cytochrome C, have served as mediators in solid state PSI devices, leveraging a charge hopping mechanism[82,132,133]. These proteins often include large transition metal centers surrounded by organic material that conforms to the center based on the oxidation state of the metal. This allows for efficient transport of charge using a larger organic system. Cytochrome C has been used with PSI by a number of groups, allowing the two proteins to complex electrostatically, demonstrating improved electrochemical performance when appropriately paired vs controls[82,132,133]. The protein is able to interact with the PSI at the P700 site, and more efficiently provide electrons, improving the performance of the system. Additionally, the protein itself may slow charge recombination within the active layer, increasing the observed open circuit potential in the process[211]. Our group has conducted some initial attempts to incorporate the protein with some promising results. We have previously incorporated Cytochrome C within the PANI/PSI polymerization solution and compared solid state devices made with the two different conditions. The device with Cytochrome C demonstrated nearly double the photocurrent as the PANI/PSI controls. This effort will be replicated within the current design of solid-state devices to determine if this result is seen consistently in functional solid state devices. (Figure5.13)

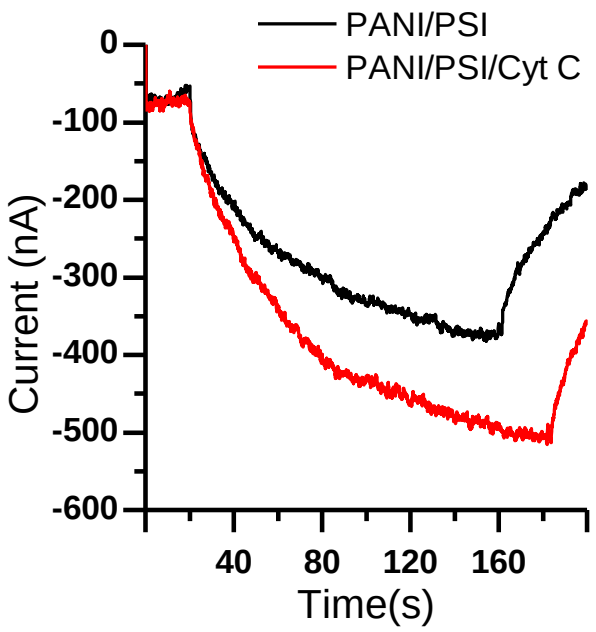

Figure 5.13 PCA of solid state device with CP cathodes, with and without cytochrome C entrapped within the PANI/PSI film

Another effort with preliminary results is the use of a layer-by-layer approach to cathode fabrication. Our group recently publish a study describing a PSI-based device where layers of PEDOT are added between layers of PSI on a planar gold electrode[125]. The process first applies an amino ethanethiol (AET) layer to create a positively charged, and amine terminated electrostatic surface on the gold electrode. The electrode is then submerged within a dilute solution of PEDOT:PSS (.5mg/ml) for 15 mins, followed by submersion into a PSI solution for 30 minutes. This process was repeated to produce the desired number of layers, with 6 layers producing the greatest photocurrent density at just over 500nA/cm^2. This process was adopted, by replacing the gold electrode with flame treated carbon paper and replacing the AET layer with a PEDOT:PSS film, electropolymerized with cyclic voltammetry. The submersion times were also extended to 30 minutes each. Early results of carbon paper electrodes with two layers of PEDOT:PSS and PSI demonstrate high photocurrent produced over time, within an electrochemical wet

cell, without the use of a diffusional mediator. The figure below shows that as the light turns on, the device produces an initial cathodic photocurrent density of $2\mu A/cm^2$, followed by a standard Cottrellian decay, associated with charge transfer limited by diffusion. This suggest the immediate response was provided by the outer surface layers of PSI and PEDOT:PSS. After 12s of illumination the photocurrent density dramatically rises to over 10 $\mu A/cm^2$ with a slow decay after the light sources was removed(Figure 5.14). This result is roughly 40 times greater than the output previously reported for two layers on a planar gold substrate, with the use of a diffusional mediator, 2 mM ubiquinone. Further studies are required to assemble this cathode with the anodes designed within this study as another means of producing high performing solid-state PSI based devices that leverage carbon paper electrodes.

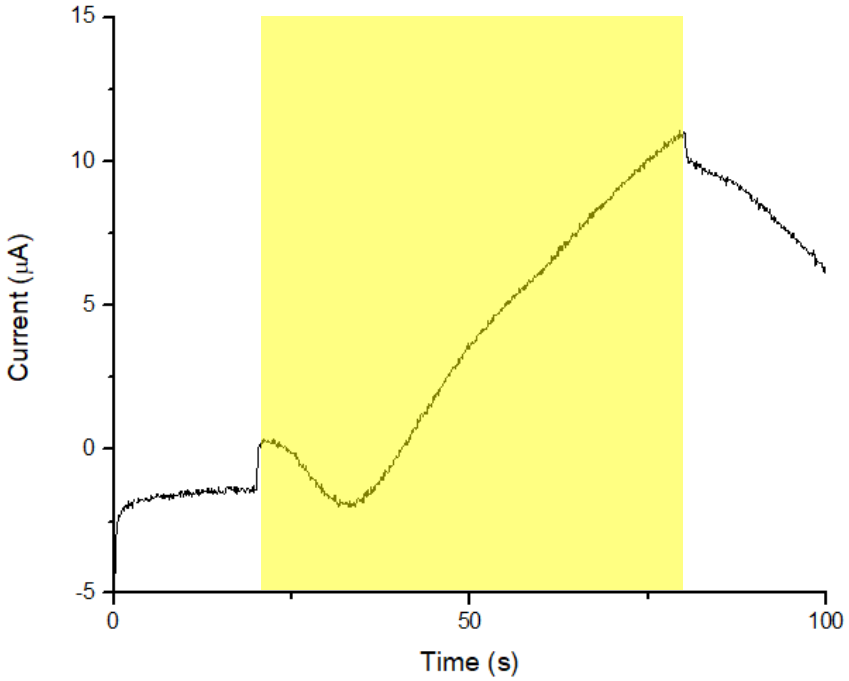

Figure 5.14 PCA of CP cathode, with two of PSI and PEDOT:PSS, applied sequentially, in an electrochemical wet cell, without the use of diffusional mediators.

5.4 Conclusion

This study offers a new baseline design for solid-state PSI-based photovoltaics, using materials and fabrication techniques that reduce cost and environmental impact. These are the first reported solid-state PSI-based devices to incorporate carbon paper electrodes as a high surface area and low cost alternative to precious metal electrodes. This study also highlights the importance of the various material layers to allow an efficient transfer of carriers through the devices, while minimizing recombination and interfacial impedance. The use of scalable fabrication processes like electrospraying/spinning, electrodeposition, and electropolymerization lower barriers to production for further research. Much additional work is needed to optimize this basic design and improve device performance. This will require additional standardization of fabrication and assembly, with a more thorough characterization of system attributes. From there, additional work to control layer thickness, stability, efficiency, and system resistance would be able to move forward. Ultimately, this design may provide a new perspective on biohybrid photovoltaics in general, demonstrating the value of a low-cost assembled devices that leverages a replaceable cathode, and renewable active layer.

Chapter 6: Conclusion

The central goal of this research was to address the growing expeditionary energy gap by developing a novel biohybrid photovoltaic. The use case was based on the shifting operational needs of the Army, and offered applications for tactical robotics, delocalized sensors, and networked warfighters as part of the army modernization strategy. While the technology is not mature, these applications should support further research and development investments from the Department of Defense (DoD) to address a growing need. In contrast to the current research focus, looking to maximize efficiency and stability in order to reduce SWaP-C, the biohybrid solution instead looks to minimize production cost and the overall environmental impact of the system, as long as the power requirements are met. This shift in view creates an opportunity to supplement the current expeditionary energy mix with a solution so cheap and benign, that it can be readily sacrificed or left behind after an operation as required.

Additionally, this work demonstrated the feasibility of an assembled photovoltaic, as opposed to a single unit being manufactured layer by layer, or an encapsulated system. This is another deviation from current research, accepting the degradation or decrease in performance associated with an assembled device. The opportunity this creates is a photovoltaic with a durable anode system, while the cathode and active layer are disposable. Field assembled and maintained photovoltaics would be a novel capability, with cheap and disposable cathodes further lowering the overall cost of the energy produced, as the active layer is produced by plants, carbon paper is cheaper at scale, and the most expensive components would be included with the durable anode. This would extend the life of devices and create additional solutions for sustained operations in austere environments.

Beyond the department of defense, assembled biohybrid photovoltaics may have a number of benefits in other sectors as well. A key innovation will be efficiently isolating the protein anywhere, from multiple sources, and preparing efficient cathodes for system use. Populations near heavy vegetation, but limited access to energy grids could use these systems in tandem with other renewable resources to maintain life-saving equipment like water pumps or refrigerators. Small communities may be able to transform yard clipping into biohybrid photovoltaics that support a microgrid. Space exploration efforts, looking to colonize distant planets may also take advantage of using the green waste from food plots, to help power their systems, as other materials may not be an option. Consider the threat posed by microplastics and algae blooms in the ocean. With these systems, harvested algae could serve as a source of PSI, while recovered plastic could be carbonized and repurposed as electrode materials. The opportunities for further development are limited by the imagination, and availability of resources.

This dissertation began with a description of the DoD modernization strategy, and the impact of the growing energy gap, highlighting the efforts currently being taken to address them. The work by PM Expeditionary Energy & Sustainment Systems and PdM Soldier power to plan for a future of renewable clean energy on the battlefield will bear fruit over the next decade as the forces begins to shift away from its reliance on fossil fuels and rechargeable batteries.

The first chapter provides some background information on the field of emerging photoelectric from NREL, describing not only how these systems work, but their advantages and limitations. Further, focusing on these emerging systems from an acquisition professional perspective helps determine which emerging technologies

represent the best investments for expeditionary energy applications given the SWaP-C and environmental performance parameters. Based on the current research, especially in roll-on manufacturing processes, the long term plan from PdM Soldier power to leverage perovskite cells for future expeditionary energy needs is sound, with encapsulation and stability being the next key gates for maturity.

The next chapter discussed the materials and methods used throughout the research, with emphasis on Photosystem I, carbon paper electrodes, and the conductive polymer polyaniline. Additionally, this chapter introduced a number of key electrochemical fabrication and characterization techniques critical to accomplishing this work, introducing key concepts that help describe the results. This chapter also begins to describe the truly interdisciplinary aspects of this research, including biology, chemistry, electrical engineering, physics, and engineering to design, fabricate, and characterize this design. Improvement on this design will also benefit from an interdisciplinary effort, as all disciplines may provide small changes that support a cumulative impact.

The next chapter focused on the application of carbon paper electrodes in biohybrid systems. The goal was to incorporate a new material, with well-defined electrochemical properties, that was both cheaper, and more scalable than the traditional metal electrodes. The work began with pretreatment to remove the hydrophobic PTFE coating, showing that flame treatment was more effective than acid treatment, as verified by electrochemical active surface area, CV, contact angle measurement, and Raman spectroscopy. Next, we demonstrated the application of high surface area CP electrodes as substrates for PSI monolayers and electropolymerized films of conductive polymers with PSI in electrochemical photovoltaic wet cells, with and without diffusional mediators. We then compared the high surface area CP electrodes with the planar gold electrodes used in

previous studies, showing the cp electrodes did not demonstrate the terminal thickness observed after 45s seen on planar gold, and that photocurrent density was considerably greater. SEM showed PANI/PSI films grown on CP electrodes demonstrated a morphology associated with higher conductivity, and EIS confirmed reduced charge transfer resistance with increased loading of PANI films on CP electrodes. Afterwards, we compared high surface area gold electrodes to both CP electrodes, and planar electrodes, observing similar trends, suggesting the high surface area influenced the loading and morphology of the PANI produced. This work paved the way for further improvement in biohybrid photovoltaic devices, as the CP electrode would introduce lower production cost, and increased scalability, while also increasing the electrochemical performance of the PANI/PSI active layer.

The final chapter described the iterative design effort involved in developing a function solid state device utilizing a CP electrode, and PANI/PSI active layer. To be considered functional, devices needed to demonstrate at least 1 mv of potential, both illuminated and in the dark, as well as produce photocurrent. The most successful, and consistent design used a flame treated carbon paper cathode with an electropolymerized PANI/PSI film for an active layer. The anode was cleaned ITO, with an electrodeposited blocking layer of TiO_2, an electrosprayed layer of TiO_2 nanoparticles, a vacuum deposited layer of PV-BR as an electron transport material, and finally, a vacuum deposited PSI monolayer. This device produce nearly 500mv of Voc and photocurrent density in the range of 10^{-7} a/cm^2 . Significantly more work is necessary to characterize and improve the design, though early results demonstrate the feasibility of the system for future research.

Ultimately, the technology to convert the energy of the sun into usable clean cheap energy is all around us. It is growing on every continent, and within every ocean. Our

ability to take advantage of that technology to address our own energy needs, and their impact on our economy, environment, politics, and national defense, will be based on our willingness to invest in a slightly different perspective.

References

1. Milley, M.A., (2016, October 4). 2016 Dwight David Eisenhower Luncheon Speech [Speech Audio/Visual recording]. AUSA, https://www.ausa.org/events/ausa-annual-meeting-exposition/sessions/eisenhower-luncheon

2. US Army in Multi-Domain Operations 2028. TP525-3-1, 6 December 2018

3. Perkins, D.G. , Multi-Domain Battle: The Advent of Twenty-First Century War. Military Review November-December (2017).

4. Decker, G. F. & Wagner, L. C. Army Strong: Equipped , Trained and Ready - Final Report of the 2010 Army Acquisition Review. 1–246 (2011).

5. US Army Futures Command Task Force, Army Futures Command, https://www.army.mil/standto/archive/2018/03/28/ (28 March 2018)

6. Judson, J, US Army asks congress to shift millions in FY18 dollars.Whats behind the request, Defensenews.com, https://www.defensenews.com/land/2018/07/17/army-asks-congress-to-shift-millions-in-fy18-dollars-to-pay-for-big-modernization-efforts/, (17 Jul, 2018)

7. www.armyfuturescommand.com

8. US Army Futures Command Concept for Maneuver in Multi-Domain Operations. AFC Pamphlet 71-20-1, 7 July 2020

9. https://www.peocscss.army.mil/pme2s2.html

10. https://www.peosoldier.army.mil/Equipment/Equipment-Portfolio/Project-Manager-Close-Combat-Squad-Portfolio/Soldier-Tactical-Power/

11. Mittal, V. US Soldiers' Burdon of Power: More Electronics Means Lugging More Batteries. Forbes.com, https://www.forbes.com/sites/vikrammittal/2020/10/26/energy-management-a-deciding-factor-of-future-battles/?sh=17354e852b1a. (26 October 2020)

12. Lafontaine, D. DOD approves Army Mobile Power program as joint capability demonstration. Army.mil, https://www.army.mil/article/234082/dod_approves_army_mobile_power_program_as_joint_capability_demonstration. (30 Mar, 2020)

13. Helman, C. For U.S Military, More Oil Means More Death, Forbes.com,https://www.forbes.com/2009/11/12/fuel-military-afghanistan-iraq-business-energy-military.html?sh=5074ac9f4562. (21 Nov 2009)

14. Glaser, C. L. (2013). How Oil Influences U.S. National Security. *International Security*, *38*(2), 112–146. http://www.jstor.org/stable/24480932

15. US Army Climate Strategy, https://www.army.mil/e2/downloads/rv7/about/2022_army_climate_strategy.pdf (2022)

16. Mittal, V. Twenty Pounds of Batteries or a Rolled-up solar Panel, Forbes.com, https://www.forbes.com/sites/vikrammittal/2021/06/02/twenty-pounds-of-batteries-or-a-rolled-up-solar-panel/?sh=5374e5056583 . (2 Jul, 2021)

17. Manser, J. S., Christians, J. A. & Kamat, P. V. Intriguing Optoelectronic Properties of Metal Halide Perovskites. *Chem. Rev.* **116**, 12956–13008 (2016).

18. Tucker, P., The US Army is Making Synthetic Biology a Priority, Defense One, https://www.defenseone.com/technology/2019/07/us-army-making-synthetic-biology-priority/158129/ (1 Jul 2019)

19. Steel, J.J, Bates, K. L., Barnhart, M.D. Investing in our nation's future military leaders' synthetic biology knowledge to understand and recognize threats and applications, *Synthetic Biology*, Volume 4, Issue 1, 2019, ysz024, https://doi.org/10.1093/synbio/ysz024

20. Musazade, E. *et al.* Biohybrid solar cells: Fundamentals, progress, and challenges. *J. Photochem. Photobiol. C Photochem. Rev.* **35**, 134–156 (2018).

21. Carro, L., Hablot, E., Coradin, T., Biofuel, B. Á. & Biosensors, Á. Hybrids and biohybrids as green materials for a blue planet. 263–271 (2014) doi:10.1007/s10971-013-3153-z.

22. Ravi, S. K. & Tan, S. C. Progress and perspectives in exploiting photosynthetic biomolecules for solar energy harnessing. *Energy and Environmental Science* vol. 8 (2015).

23. Srivastava, S. K. *et al.* A Biogenic Photovoltaic Material. **2**, 1–6 (2018).

24. Baker, D. R. *et al.* Comparative photoactivity and stability of isolated cyanobacterial monomeric and trimeric photosystem i. *J. Phys. Chem. B* **118**, 2703–2711 (2014).

25. Manocchi, A. K. *et al.* Photocurrent generation from surface assembled photosystem i on alkanethiol modified electrodes. *Langmuir* **29**, 2412–2419 (2013).

26. Simmerman, R. F. *et al.* Engineering Photosystem i Complexes with Metal Oxide Binding Peptides for Bioelectronic Applications. *Bioconjug. Chem.* **26**, 2097–2105 (2015).

27. Baker, D. R., Simmerman, R. F., Sumner, J. J., Bruce, B. D. & Lundgren, C. A. Photoelectrochemistry of photosystem I bound in Nafion. *Langmuir* **30**, 13650–13655 (2014).

28. Ridge Carter, J., Baker, D. R., Austin Witt, T. & Bruce, B. D. Enhanced photocurrent from Photosystem i upon in vitro truncation of the antennae chlorophyll. *Photosynth. Res.* **127**, 161–170 (2016).

29. https://www.nrel.gov/about/history.html

30. https://www.nrel.gov

31. https://www.nrel.gov/pv/cell-efficiency.html

32. Regan, B. O. & Gratzelt, M. A low-cost, high-efficiency solar cell based on dye-sensitized colloidal Ti02 films. **353**, 737–740 (1991).

33. Sharma, K., Sharma, V. & Sharma, S. S. Dye-Sensitized Solar Cells: Fundamentals and Current Status. *Nanoscale Res. Lett.* **13**, (2018).

34. Benesperi, I., Michaels, H. & Freitag, M. The researcher's guide to solid-state dye-sensitized solar cells. *Journal of Materials Chemistry C* vol. 6 11903–11942 (2018).

35. Luceño-Sánchez, J. A., María Díez-Pascual, A. & Capilla, R. P. Molecular Sciences Materials for Photovoltaics: State of Art and Recent Developments. (2019) doi:10.3390/ijms20040976.

36. Tennakone, K. et al. A dye-sensitized nano-porous solid-state photovoltaic cell.*Semicond. Sci. Technol.* **10, 1789-1693** (1995).

37. Bin, J. W., Kim, D. H., Sung, Y. M. & Park, M. W. Effects of TiO2 electron blocking layer on photovoltaic performance of photo-electrochemical cell. *Opt. Mater. (Amst).* **36**, 1454–1458 (2014).

38. Kim, D. H., Woodroof, M., Lee, K. & Parsons, G. N. Atomic Layer Deposition of High Performance Ultrathin TiO 2 Blocking Layers for Dye-Sensitized Solar Cells. 1014–1020 (2013) doi:10.1002/cssc.201300067.

39. Yoo, B. *et al.* Chemically deposited blocking layers on FTO substrates : Effect of precursor concentration on photovoltaic performance of dye-sensitized solar cells. *J. Electroanal. Chem.* **638**, 161–166 (2010).

40. You, A., Be, M. A. Y. & In, I. The effect of screen printed blocking layer on the performance of monolithic DSSC The effect of screen printed blocking layer on the performance of monolithic DSSC. **060003**, 0–6 (2020).

41. Kavan, L., Tétreault, N., Moehl, T. & Grätzel, M. Electrochemical characterization of TiO2 blocking layers for dye-sensitized solar cells. *J. Phys. Chem. C* **118**, 16408–16418 (2014).

42. Sangiorgi, A., Bendoni, R., Sangiorgi, N., Sanson, A. & Ballarin, B. Optimized TiO2 blocking layer for dye-sensitized solar cells. *Ceram. Int.* **40**, 10727–10735 (2014).

43. Zhu, T. *et al.* Electrospray dense suspensions of TiO2 nanoparticles for dye sensitized solar cells. *Aerosol Sci. Technol.* **47**, 1302–1309 (2013).

44. Hajjaji, A., Amlouk, M., Gaidi, M., Bessais, B. & El Khakani, M. A. *Tio2 properties and deposition techniques*. *SpringerBriefs in Applied Sciences and Technology* (2015). doi:10.1007/978-3-319-13353-9_1.

45. Patra, S. *et al.* Low-temperature electrodeposition approach leading to robust mesoscopic anatase TiO2 films. *Sci. Rep.* **6**, (2016).

46. Lawman, G. M. & Hammond, P. T. Solid-state dye-sensitized solar cells combining a porous TiO2 film and a layerby-layer composite electrolyte. *Small* **1**, 1070–1073 (2005).

47. Grätzel, M. Sol-gel processed TiO2 films for photovoltaic applications. *J. Sol-Gel Sci. Technol.* **22**, 7–13 (2001).

48. Xiang, Y. *et al.* Improved performance of nanoporous TiO2 film in dye-sensitized solar cells via ZrCl4 and TiCl4 surface co-modifications. *Mater. Sci. Semicond. Process.* **49**, 48–53 (2016).

49. Bach, U. et al. Solid-state dye-sensitized mesoporous TiO2 solar cells with high photon-to-electron conversion efficiencies. *Nature*. **395,** 583-585 (1998)

50. Wang, H. *et al.* Solid-state composite electrolyte Lil/3-hydroxypropionitrile/SiO 2 for dye-sensitized solar cells. *J. Am. Chem. Soc.* **127**, 6394–6401 (2005).

51. Boschloo, G. Improving the performance of dye-sensitized solar cells. *Front. Chem.* **7**, 1–9 (2019).

52. Krüger, J. *et al.* High efficiency solid-state photovoltaic device due to inhibition of interface charge recombination. *Appl. Phys. Lett.* **79**, 2085–2087 (2001).

53. Krishnan, G. Polymer Ruled Electronics World. **2**, 225–230 (2016).

54. Tan, S. *et al.* Property influence of polyanilines on photovoltaic behaviors of dye-sensitized solar cells. *Langmuir* **20**, 2934–2937 (2004).

55. Surana K., Mehra R.M. (2018) Quantum Dot Sensitized Solar Cells (QDSSCs). In: Khan Z. (eds) Nanomaterials and Their Applications. Advanced Structured Materials, vol 84. Springer, Singapore. https://doi.org/10.1007/978-981-10-6214-8_12

56. car, H. & Sariciftci, N. S. Organic solar cells: An overview. *J. Mater. Res.* **19**, 1924–1945 (2004).

57. Xu, X. *et al.* Thermally stable, highly efficient, ultraflexible organic photovoltaics. doi:10.1073/pnas.1801187115.

58. Wu, Y. *et al.* Fine-Tuning Semiconducting Polymer Self-Aggregation and Crystallinity Enables Optimal Morphology and High-Performance Printed All-Polymer Solar Cells. *J. Am. Chem. Soc.* **142**, 392–406 (2020).

59. Gu, X. *et al.* Comparison of the Morphology Development of Polymer–Fullerene and Polymer–Polymer Solar Cells during Solution-Shearing Blade Coating. *Adv. Energy Mater.* **6**, 1–12 (2016).

60. Von Hauff, E. Impedance Spectroscopy for Emerging Photovoltaics. *J. Phys. Chem. C* **123**, 11329–11346 (2019).

61. Dabera, G. D. M. R., Lee, J. & Hatton, R. A. An Electrode Design Rule for Organic Photovoltaics Elucidated Using a Low Surface Area Electrode. *Adv. Funct. Mater.* **29**, 1–9 (2019).

62. Konios, D. *et al.* Reduced graphene oxide micromesh electrodes for large area, flexible, organic photovoltaic devices. *Adv. Funct. Mater.* **25**, 2213–2221 (2015).

63. Jäckle, S. *et al.* Junction formation and current transport mechanisms in hybrid n-Si/PEDOT:PSS solar cells. *Sci. Rep.* **5**, (2015).

64. Zhou, Y. *et al.* High performance all-polymer solar cell via polymer side-chain engineering. *Adv. Mater.* **26**, 3767–3772 (2014).

65. Rao, S., Morankar, A., Verma, H. & Goswami, P. Emerging Photovoltaics: Organic, Copper Zinc Tin Sulphide, and Perovskite-Based Solar Cells. *J. Appl. Chem.* **2016**, 1–12 (2016).

66. Kawakita, J., Fujikawa, Y., Nagata, T. & Chikyow, T. Interfacial charge transfer behavior of conducting polymers as contact electrode for semiconductor devices. *Jpn. J. Appl. Phys.* **55**, (2016).

67. Feast, W. J., Tsibouklis, J., Pouwer, K. L., Groenendaal, L. & Meijer, E. W. Synthesis, processing and material properties of conjugated polymers. *Polymer (Guildf).* **37**, 5017–5047 (1996).

68. Ahmad, J., Bazaka, K., Anderson, L. J., White, R. D. & Jacob, M. V. Materials and methods for encapsulation of OPV: A review. *Renew. Sustain. Energy Rev.* **27**, 104–117 (2013).

69. Qi, B. & Wang, J. Open-circuit voltage in organic solar cells. 24315–24325 (2012) doi:10.1039/c2jm33719c.

70. Hao, M. Y. *et al.* Effect of energetic distribution of trap states on fill factor in perovskite solar cells. *J. Power Sources* **479**, (2020).

71. Bou, A. *et al.* Beyond Impedance Spectroscopy of Perovskite Solar Cells: Insights from the Spectral Correlation of the Electrooptical Frequency Techniques. *J. Phys. Chem. Lett.* **11**, 8654–8659 (2020).

72. Kojima, A., Teshima, K., Shirai, Y. & Miyasaka, T. Organometal halide perovskites as visible-light sensitizers for photovoltaic cells. *J. Am. Chem. Soc.* **131**, 6050–6051 (2009).

73. Cheacharoen, R. *et al.* Encapsulating perovskite solar cells to withstand damp heat and thermal cycling. *Sustain. Energy Fuels* **2**, 2398–2406 (2018).

74. Li, J. *et al.* Encapsulation of perovskite solar cells for enhanced stability: Structures, materials and characterization. *J. Power Sources* **485**, (2021).

75. Corsini, F. & Griffini, G. Recent progress in encapsulation strategies to enhance the stability of organometal halide perovskite solar cells. *JPhys Energy* **2**, (2020).

76. Jaeki Jeong1, 2, 3, 11 *et al.* Pseudo-halide anion engineering for α-FAPbI3 perovskite solar cells. *Nature* **592**, (2020).

77. Zhang, M. *et al.* Single-layered organic photovoltaics with double cascading charge transport pathways: 18% efficiencies. *Nat. Commun.* **12**, 1–10 (2021).

78. Zhang, D. *et al.* A molecular photosensitizer achieves a V oc of 1.24 V enabling highly efficient and stable dye-sensitized solar cells with copper(II/I)-based electrolyte. *Nat. Commun.* **12**, 2–11 (2021).

79. Sjoholm, K. H., Rasmussen, M. & Minteer, S. D. Bio-solar cells incorporating catalase for stabilization of thylakoid bioelectrodes during direct photoelectrocatalysis. *ECS Electrochem. Lett.* **1**, 2012–2014 (2012).

80. Fromme, P., Jordan, P. & M, N. K. Structure of photosystem I. **1507**, (2001).

81. Amunts, A., Drory, O. & Nelson, N. The structure of a plant photosystem I supercomplex at 3.4 Å resolution. *Nature* **447**, 58–63 (2007).

82. Stieger, K. R. *et al.* protein architectures:the defined co-assembly of. 10695–10705 (2016) doi:10.1039/c6nr00097e.

83. Webber, A. N. & Lubitz, W. P700: The primary electron donor of photosystem I. *Biochim. Biophys.*

Acta - Bioenerg. **1507**, 61–79 (2001).

84. Ciobanu, M., Kincaid, H. A., Jennings, G. K. & Cliffel, D. E. Photosystem I patterning imaged by scanning electrochemical microscopy. *Langmuir* **21**, 692–698 (2005).

85. Ben-Shem, A., Frolow, F. & Nelson, N. Crystal structure of plant photosystem I. *Nature* **426**, 630–635 (2003).

86. Ben-Shem, A., Frolow, F. & Nelson, N. Evolution of photosystem I - From symmetry through pseudosymmetry to asymmetry. *FEBS Lett.* **564**, 274–280 (2004).

87. Castañeda Ocampo, O. E. *et al.* Mechanism of Orientation-Dependent Asymmetric Charge Transport in Tunneling Junctions Comprising Photosystem i. *J. Am. Chem. Soc.* **137**, 8419–8427 (2015).

88. Brettel, K. & Leibl, W. Electron transfer in photosystem I. *Biochim. Biophys. Acta - Bioenerg.* **1507**, 100–114 (2001).

89. Teodor, A. H. & Bruce, B. D. Putting Photosystem I to Work: Truly Green Energy. *Trends in Biotechnology* vol. 38 1329–1342 (2020).

90. Wang, X. *et al.* Solubilization and Stabilization of Isolated Photosystem I Complex with Lipopeptide Detergents. *PLoS One* **8**, 1–12 (2013).

91. Nagakawa, H. *et al.* Efficient hydrogen production using photosystem I enhanced by artificial light harvesting dye. *Photochem. Photobiol. Sci.* **18**, 309–313 (2019).

92. Shubin, V. V. *et al.* Thermostability of photosystem I trimers and monomers from the cyanobacterium Thermosynechococcus elongatus. *Spectrochim. Acta - Part A Mol. Biomol. Spectrosc.* **179**, 17–22 (2017).

93. Ivanov, A. G., Velitchkova, M. Y., Allakhverdiev, S. I. & Huner, N. P. A. Heat stress-induced effects of photosystem I: an overview of structural and functional responses. *Photosynth. Res.* **133**, 17–30 (2017).

94. Zeynali, A., Ghiasi, T. S., Riazi, G. & Ajeian, R. Organic solar cell based on photosystem I pigment-protein complex, fabrication and optimization. *Org. Electron. physics, Mater. Appl.* **51**, 341–348 (2017).

95. Beam, J. C. *et al.* Construction of a Semiconductor-Biological Interface for Solar Energy Conversion: P-Doped Silicon/Photosystem I/Zinc Oxide. *Langmuir* **31**, 10002–10007 (2015).

96. Gunther, D., Leblanc, G., Cliffel, D. E. & Kane Jennings, G. Pueraria lobata (Kudzu) photosystem i improves the photoelectrochemical performance of silicon. *Ind. Biotechnol.* **9**, 37–41 (2013).

97. Ciesielski, P. N. *et al.* Enhanced photocurrent production by Photosystem i multilayer assemblies. *Adv. Funct. Mater.* **20**, 4048–4054 (2010).

98. Robinson, M. T., Armbruster, M. E., Gargye, A., Cliffel, D. E. & Jennings, G. K. Photosystem i Multilayer Films for Photovoltage Enhancement in Natural Dye-Sensitized Solar Cells. *ACS Appl. Energy Mater.* **1**, 301–305 (2018).

99. Barhom, H., Carmeli, C. & Carmeli, I. Fabrication of Electronic Junctions between Oriented

Multilayers of Photosystem I and the Electrodes of Optoelectronic Solid-State Devices. *J. Phys. Chem. B* (2021) doi:10.1021/acs.jpcb.0c08161.

100. Robinson, M. T., Cliffel, D. E. & Jennings, G. K. An Electrochemical Reaction-Diffusion Model of the Photocatalytic Effect of Photosystem i Multilayer Films. *J. Phys. Chem. B* **122**, 117–125 (2018).

101. Chen, G., LeBlanc, G., Jennings, G. K. & Cliffel, D. E. Effect of redox mediator on the photo-induced current of a photosystem i modified electrode. *J. Electrochem. Soc.* **160**, 315–320 (2013).

102. Petrova, A., Mamedov, M., Ivanov, B., Semenov, A. & Kozuleva, M. Effect of artificial redox mediators on the photoinduced oxygen reduction by photosystem I complexes. *Photosynth. Res.* **137**, 421–429 (2018).

103. Gunther, D. *et al.* Photosystem i on graphene as a highly transparent, photoactive electrode. *Langmuir* **29**, 4177–4180 (2013).

104. Ciesielski, P. N. *et al.* Photosystem I - Based biohybrid photoelectrochemical cells. *Bioresour. Technol.* **101**, 3047–3053 (2010).

105. Simmerman, R. F. *et al.* Engineering Photosystem i Complexes with Metal Oxide Binding Peptides for Bioelectronic Applications. *Bioconjug. Chem.* **26**, 2097–2105 (2015).

106. Sokol, K. P. *et al.* Rational wiring of photosystem II to hierarchical indium tin oxide electrodes using redox polymers. *Energy Environ. Sci.* **9**, 3698–3709 (2016).

107. Robinson, M. T., Gizzie, E. A., Mwambutsa, F., Cliffel, D. E. & Jennings, G. K. Mediated approaches to Photosystem I-based biophotovoltaics. *Curr. Opin. Electrochem.* **5**, 211–217 (2017).

108. Szewczyk, S., Białek, R., Burdziński, G. & Gibasiewicz, K. Photovoltaic activity of electrodes based on intact photosystem I electrodeposited on bare conducting glass. 1–12 (2020).

109. Samuel Ko, B. *et al.* Effect of surface composition on the adsorption of photosystem I onto alkanethiolate self-assembled monolayers on gold. *Langmuir* **20**, 4033–4038 (2004).

110. Leblanc, G., Gizzie, E., Yang, S., Cliffel, D. E. & Jennings, G. K. Photosystem I protein films at electrode surfaces for solar energy conversion. *Langmuir* **30**, 10990–11001 (2014).

111. Faulkner, C. J., Lees, S., Ciesielski, P. N., Cliffel, D. E. & Jennings, G. K. Rapid assembly of photosystem I monolayers on gold electrodes. *Langmuir* **24**, 8409–8412 (2008).

112. Zhao, F., Ruff, A., Rögner, M., Schuhmann, W. & Conzuelo, F. Extended Operational Lifetime of a Photosystem-Based Bioelectrode. *J. Am. Chem. Soc.* **141**, 5102–5106 (2019).

113. Ciesielski, P. N., Cliffel, D. E. & Jennings, G. K. Kinetic model of the photocatalytic effect of a photosystem i monolayer on a planar electrode surface. *J. Phys. Chem. A* **115**, 3326–3334 (2011).

114. Manocchi, A. K. *et al.* Photocurrent generation from surface assembled photosystem i on alkanethiol modified electrodes. *Langmuir* **29**, 2412–2419 (2013).

115. Kiliszek, M. *et al.* Orientation of photosystem i on graphene through cytochrome: C 553 leads to improvement in photocurrent generation. *J. Mater. Chem. A* **6**, 18615–18626 (2018).

116. Tapia, C. *et al.* Wiring of Photosystem I and Hydrogenase on an Electrode for Photoelectrochemical H2 Production by using Redox Polymers for Relatively Positive Onset Potential. *ChemElectroChem* **4**, 90–95 (2017).

117. Zeynali, A., Ghiasi, T. S., Riazi, G. & Ajeian, R. Organic solar cell based on photosystem I pigment-protein complex, fabrication and optimization. *Org. Electron. physics, Mater. Appl.* **51**, 341–348 (2017).

118. Version, D. University of Groningen Integration and modification of photosystem I for bio-photovoltaics Gordiichuk, Pavlo. (2016).

119. Bennett, T. H. *et al.* Jolly green MOF: confinement and photoactivation of photosystem I in a metal–organic framework. *Nanoscale Adv.* **1**, 94–104 (2019).

120. Gizzie, E. A. *et al.* Photosystem I-polyaniline/TiO2solid-state solar cells: Simple devices for biohybrid solar energy conversion. *Energy Environ. Sci.* **8**, 3572–3576 (2015).

121. Kincaid, H. A., Niedringhaus, T., Ciobanu, M., Cliffel, D. E. & Kane Jennings, G. Entrapment of photosystem I within self-assembled films. *Langmuir* **22**, 8114–8120 (2006).

122. Gizzie, E. A., Leblanc, G., Jennings, G. K. & Cliffel, D. E. Electrochemical preparation of photosystem I-polyaniline composite films for biohybrid solar energy conversion. *ACS Appl. Mater. Interfaces* **7**, 9328–9335 (2015).

123. Robinson, M. T., Simons, C. E., Cliffel, D. E. & Jennings, G. K. Photocatalytic photosystem I/PEDOT composite films prepared by vapor-phase polymerization. *Nanoscale* **9**, 6158–6166 (2017).

124. Cherubin, A. *et al.* Encapsulation of Photosystem I in Organic Microparticles Increases Its Photochemical Activity and Stability for Ex Vivo Photocatalysis. *ACS Sustain. Chem. Eng.* **7**, 10435–10444 (2019).

125. Wolfe, K. D. *et al.* Layer-by-Layer Assembly of Photosystem I and PEDOT:PSS Biohybrid Films for Photocurrent Generation. *Langmuir* **37**, 10481–10489 (2021).

126. Molamohammadi, S., Seyed Jalili, Y. & Riazi, G. Photosystem i application in biohybrid polymer solar cells. *AIP Adv.* **8**, (2018).

127. Badura, A. *et al.* Photocurrent generation by photosystem 1 integrated in crosslinked redox hydrogels. *Energy Environ. Sci.* **4**, 2435–2440 (2011).

128. Gordiichuk, P. I. *et al.* Solid-state biophotovoltaic cells containing photosystem i. *Adv. Mater.* **26**, 4863–4869 (2014).

129. Dervishogullari, D., Gizzie, E. A., Jennings, G. K. & Cliffel, D. E. Polyviologen as Electron Transport Material in Photosystem I-Based Biophotovoltaic Cells. *Langmuir* **34**, 15658–15664 (2018).

130. Qiu, X. *et al.* Self-Regenerating Soft Biophotovoltaic Devices. *ACS Appl. Mater. Interfaces* **10**, 37625–37633 (2018).

131. Ravi, S. K., Udayagiri, V. S., Suresh, L. & Tan, S. C. Emerging Role of the Band-Structure Approach in Biohybrid Photovoltaics : A Path Beyond Bioelectrochemistry. **1705305**, 1–18 (2018).

132. Stieger, K. R. *et al.* current conversion based on photosystem I within. 17009–17017 (2016) doi:10.1039/c6ta07141d.

133. Stieger, K. R. *et al.* Biohybrid architectures for efficient light-to-current conversion based on photosystem i within scalable 3D mesoporous electrodes. *J. Mater. Chem. A* **4**, 17009–17017 (2016).

134. Kazemzadeh, S., Riazi, G. & Ajeian, R. Novel Approach of Biophotovoltaic Solid State Solar Cells Based on a Multilayer of PS1 Complexes as an Active Layer. *ACS Sustain. Chem. Eng.* **5**, 9836–9840 (2017).

135. Nguyen, K.; Bruce, B. D., Growing green electricity: Progress and strategies for use of Photosystem I for sustainable photovoltaic energy conversion. *Biochimica et Biophysica Acta (BBA) - Bioenergetics* **2014,** *1837*, 1553-1566.

136. Wolfe, K. D.; Dervishogullari, D.; Passantino, J. M.; Stachurski, C. D.; Jennings, G. K.; Cliffel, D. E., Improving the stability of photosystem I–based bioelectrodes for solar energy conversion. *Current Opinion in Electrochemistry* **2020,** *19*, 27-34.

137. Friebe, V. M.; Frese, R. N., Photosynthetic reaction center-based biophotovoltaics. *Current Opinion in Electrochemistry* **2017,** *5*, 126-134.

138. Baba, K.; Itoh, S.; Hastings, G.; Hoshina, S., Photoinhibition of Photosystem I electron transfer activity in isolated Photosystem I preparations with different chlorophyll contents. *Photosynthesis Research* **1996,** *47*, 121-130.

139. Reeves, S. G.; Hall, D. O., [8] Higher plant chloroplasts and grana: General preparative procedures (excluding high carbon dioxide fixation ability chloroplasts). In *Photosynthesis and Nitrogen Fixation - Part C*, San Pietro, A. B. T.-M. i. E., Ed. Academic Press: 1980; Vol. 69, pp 85-94.

140. Shiozawa, J. A.; Alberte, R. S.; Thornber, J. P., The P700-chlorophyll a-protein: Isolation and some characteristics of the complex in higher plants. *Archives of Biochemistry and Biophysics* **1974,** *165* (1), 388-397.

141. Gorbunoff, M. J., The interaction of proteins with hydroxyapatite: I. Role of protein charge and structure. *Anal Biochem* **1984,** *136* (2), 425-432.

142. Korotych, O.; Mondal, J.; Gattás-Asfura, K. M.; Hendricks, J.; Bruce, B. D., Evaluation of commercially available styrene-co-maleic acid polymers for the extraction of membrane proteins from spinach chloroplast thylakoids. *European Polymer Journal* **2019,** *114*, 485-500.

143. Åkerlund, H.-E.; Andersson, B.; Persson, A.; Albertsson, P.-Å., Isoelectric points of spinach thylakoid membrane surfaces as determined by cross partition. *Biochimica et Biophysica Acta (BBA) - Biomembranes* **1979,** *552* (2), 238-246.

144. Eftekhari, A., Li, L. & Yang, Y. Polyaniline supercapacitors. *J. Power Sources* **347**, 86–107 (2017).

145. Abd Razak, S. I. *et al.* A review of electrospun conductive polyaniline based nanofiber composites and blends: Processing features, applications, and future directions. *Adv. Mater. Sci. Eng.* **2015**, (2015).

146. Stejskal, J., Sapurina, I. & Trchová, M. Polyaniline nanostructures and the role of aniline oligomers in their formation. *Prog. Polym. Sci.* **35**, 1420–1481 (2010).

147. Hidayat, A. T., Kusumaatmaja, A., Chotimah, Soekrisno, R. & Triyana, K. Effect of polyaniline polymerization methods on the preparation of electrospun polyaniline nanofiber. *AIP Conf. Proc.* **1755**, (2016).

148. Babaiee, M., Pakshir, M. & Hashemi, B. Effects of potentiodynamic electropolymerization parameters on electrochemical properties and morphology of fabricated PANI nanofiber/graphite electrode. *Synth. Met.* **199**, 110–120 (2015).

149. Hammo, S. M. Effect of Acidic Dopants properties on the Electrical Conductivity of Poly aniline. *Tikrit J. Pure Sci.* **17**, 2012 (2012).

150. Potphode, D. D., Sivaraman, P., Mishra, S. P. & Patri, M. Polyaniline/partially exfoliated multi-walled carbon nanotubes based nanocomposites for supercapacitors. *Electrochim. Acta* **155**, 402–410 (2015).

151. Yanilmaz, M., Dirican, M., Asiri, A. M. & Zhang, X. Flexible polyaniline-carbon nanofiber supercapacitor electrodes. *J. Energy Storage* **24**, 100766 (2019).

152. Dominic, J. *et al.* Supercapacitor performance study of lithium chloride doped polyaniline. *Appl. Surf. Sci.* **460**, 40–47 (2018).

153. Zhou, S. X. *et al.* Facile synthesis of self-assembled polyaniline nanorods doped with sulphuric acid for high-performance supercapacitors. *Vacuum* **143**, 63–70 (2017).

154. Yu, T. *et al.* Synthesis of microspherical polyaniline/graphene composites and their application in supercapacitors. *Electrochim. Acta* **222**, 12–19 (2016).

155. Liu, H. *et al.* Three-dimensional graphene/polyaniline composite material for high-performance supercapacitor applications. *Mater. Sci. Eng. B Solid-State Mater. Adv. Technol.* **178**, 293–298 (2013).

156. Yan, Y., Cheng, Q., Wang, G. & Li, C. Growth of polyaniline nanowhiskers on mesoporous carbon for supercapacitor application. *J. Power Sources* **196**, 7835–7840 (2011).

157. Zhang, L. *et al.* Three-dimensional structures of graphene/polyaniline hybrid films constructed by steamed water for high-performance supercapacitors. *J. Power Sources* **342**, 1–8 (2017).

158. Wang, L. *et al.* Flexible solid-state supercapacitor based on a metal-organic framework interwoven by electrochemically-deposited PANI. *J. Am. Chem. Soc.* **137**, 4920–4923 (2015).

159. Cherrington, R., Liang, J. 2 - Materials and Deposition Processes for Multifunctionality, Design and Manufacture of Plastic Components for Multifunctionality, 2016, 19-51

160. Somboonsub, B. *et al.* Comparison of the thermally stable conducting polymers PEDOT, PANi, and PPy using sulfonated poly(imide) templates. *Polymer (Guildf).* **51**, 4472–4476 (2010).

161. Li, W. *et al.* Understanding the role of different conductive polymers in improving the nanostructured sulfur cathode performance. *Nano Lett.* **13**, 5534–5540 (2013).

162. Bryan, A. M., Santino, L. M., Lu, Y., Acharya, S. & D'Arcy, J. M. Conducting Polymers for Pseudocapacitive Energy Storage. *Chem. Mater.* **28**, 5989–5998

163. Wallace, G., Spinks, G, Kane-Maguire, L.,Teasedale, P., (2003) Conductive Electroactive Polymers:Intelligent Material Systems(2nd ed),(pp 121-177)Boca Raton, Florida, CRC Press

164. Frontera, P. *et al.* Polyaniline nanofibers: Towards pure electrospun PANI. *AIP Conf. Proc.* **1459**, 253–255 (2012).

165. Al-Jallad, M. & Atassi, Y. Preparation of nonwoven mats of electrospun poly(lactic acid)/polyaniline blend nanofibers: A new approach. *J. Appl. Polym. Sci.* **133**, 1–10 (2016).

166. Beygisangchin, M., Rashid, S. A., Shafie, S., Sadrolhosseini, A. R. & Lim, H. N. Preparations, properties, and applications of polyaniline and polyaniline thin films—a review. *Polymers (Basel).* **13**, (2021).

167. Desilvestro,J. and Scheifele,W., Morphology of electrochemically prepared Polyaniline. Influence of Polymerization Parameters. *J. Mater. Chem.*1993,3:263

168. Mathur, R. B., Maheshwari, P. H., Dhami, T. L. & Tandon, R. P. Characteristics of the carbon paper heat-treated to different temperatures and its influence on the performance of PEM fuel cell. *Electrochim. Acta* **52**, 4809–4817 (2007).

169. Yuan, C. J., Wang, C. L., Wu, T. Y., Hwang, K. C. & Chao, W. C. Fabrication of a carbon fiber paper as the electrode and its application toward developing a sensitive unmediated amperometric biosensor. *Biosens. Bioelectron.* **26**, 2858–2863 (2011).

170. Teixeira, C. O., Andrade, L. & Mendes, A. Easy processing carbon paper electrode for highly efficient perovskite solar cells. *J. Power Sources* **479**, 1–8 (2020).

171. Ye, D. et al. Role of defects and oxygen-functional groups in carbon paper cathode for high-performance direct liquid fuel cells. Carbon (Elsevier Ltd, 2022). doi:10.1016/j.carbon.2022.02.053.

172. Singh, A. K., Yasri, N., Karan, K. & Roberts, E. P. L. Electrocatalytic Activity of Functionalized Carbon Paper Electrodes and Their Correlation to the Fermi Level Derived from Raman Spectra. *ACS Appl. Energy Mater.* **2**, 2324–2336 (2019).

173. Kuwahara, T., Ohta, H., Kondo, M. & Shimomura, M. Immobilization of glucose oxidase on carbon paper electrodes modified with conducting polymer and its application to a glucose fuel cell. *Bioelectrochemistry* **74**, 66–72 (2008).

174. Bard, A., Faulkner, L. Electrochemical Methods:Fundamentals and applications(2nd ed), (pp226-256). Hoboken, New Jersey, John Wiley & Sons,inc. (2001)

175. Wolfe, K. D. *et al.* Photosystem I Multilayers within Porous Indium Tin Oxide Cathodes Enhance Mediated Electron Transfer. *ChemElectroChem* 596–603 (2019) doi:10.1002/celc.201901628.

176. Bard, A., Faulkner, L. Electrochemical Methods:Fundamentals and applications(2nd ed), (pp 368-414). Hoboken, New Jersey, John Wiley & Sons,inc. (2001)

177. Sekar, N & Ramasamy, R. (2013). Electrochemical Impedance Spectroscopy for Microbial Fuel Cell Characterization. Journal of Microbial and Biochemical Technology. 5. 10.4172/1948-5948.S6-004.

178. Agostiano, A., Ceglie, A. & Monica, M. Della. 564--Current-Potential Curves of Photosystems . **155**, 377–384 (1983).

179. Lee, I.; Lee, J. W.; Warmack, R. J.; Allison, D. P.; Greenbaum, E. Molecular Electronics of a Single Photosystem I Reaction Center: Studies with Scanning Tunneling Microscopy and Spectroscopy. Proc.

Natl. Acad. Sci. U.S.A. 1995, 92, 1965−1969.

180. Terasaki, N.; Yamamoto, N.; Hiraga, T.; Yamanoi, Y.; Yonezawa,T.; Nishihara, H.; Ohmori, T.; Sakai, M.; Fujii, M.; Tohri, A.; et al. Plugging a Molecular Wire into Photosystem I: Reconstitution of the Photoelectric Conversion System on a Gold Electrode. Angew. Chem., Int. Ed. 2009, 48, 1585−1587.

181. Kievit, O.; Brudvig, G. W. Direct Electrochemistry of Photo- system I. J. Electroanal. Chem. 2001, 497, 139−149.

182. Yehezkeli, O.; Tel-Vered, R.; Michaeli, D.; Nechushtai, R.; Willner, I. Photosystem I (PSI)/Photosystem II (PSII)-Based Photo- Bioelectrochemical Cells Revealing Directional Generation of Photo- currents. Small 2013, 9, 2970−2978.

183. Mershin, A.; Matsumoto, K.; Kaiser, L.; Yu, D.; Vaughn, M.; Nazeeruddin, M. K.; Bruce, B. D.; Graetzel, M.; Zhang, S. Self- Assembled Photosystem-I Biophotovoltaics on Nanostructured TiO2 and ZnO. Sci. Rep. 2012, 2. (11)

184. Leblanc, G., Winter, K. M., Crosby, W. B., Jennings, G. K. & Cliffel, D. E. Integration of photosystem i with graphene oxide for photocurrent enhancement. *Adv. Energy Mater.* **4**, 1–5 (2014).

185. Darby, E. *et al.* Photoactive films of photosystem I on transparent reduced graphene oxide electrodes. *Langmuir* **30**, 8990–8994 (2014).

186. Ciornii, D. *et al.* Construction of photobiocathodes using multi-walled carbon nanotubes and photosystem I. *Phys. Status Solidi Appl. Mater. Sci.* **214**, (2017).

187. Morlock, S., Subramanian, S. K., Zouni, A. & Lisdat, F. Scalable Three-Dimensional Photobioelectrodes Made of Reduced Graphene Oxide Combined with Photosystem i. *ACS Appl. Mater. Interfaces* **13**, 11237–11246 (2021).

188. Mayrhuber, I., Dennison, C. R., Kalra, V., & Kumbur, E. C. (2014). Laser-perforated carbon paper electrodes for improved mass-transport in high power density vanadium redox flow batteries. Journal of Power Sources, 260, 251–258. https://doi.org/10.1016/j.jpowsour.2014.03.007

189. Arechederra, R., & Minteer, S. D. (2008). Organelle-based biofuel cells: Immobilized mitochondria on carbon paper electrodes. Electrochimica Acta, 53(23), 6698–6703. https://doi.org/10.1016/j.electacta.2008.01.074

190. Pandey, G. P., Rastogi, A. C., & Westgate, C. R. (2014). All-solid-state supercapacitors with poly(3,4-ethylenedioxythiophene)- coated carbon fiber paper electrodes and ionic liquid gel polymer electrolyte. Journal of Power Sources, 245, 857–865. https://doi.org/10.1016/j.jpowsour.2013.07.017

191. Hsieh, C. Te, Hung, W. M., & Chen, W. Y. (2010). Electrochemical activity and stability of Pt catalysts on carbon nanotube/carbon paper composite electrodes. International Journal of Hydrogen Energy, 35(16), 8425–8432. https://doi.org/10.1016/j.ijhydene.2010.04.125

192. Hsieh, C. Te, Teng, H., Chen, W. Y., & Cheng, Y. S. (2010). Synthesis, characterization, and electrochemical capacitance of amino-functionalized carbon nanotube/carbon paper electrodes. Carbon, 48(15), 4219–4229. https://doi.org/10.1016/j.carbon.2010.07.021

193. Bombelli, Paolo, Marie Zarrouati, Rebecca J. Thorne, Kenneth Schneider, Stephen J.L. Rowden, Akin Ali, Kamran Yunus, et al. 2012. “Surface Morphology and Surface Energy of Anode Materials

Influence Power Outputs in a Multi-Channel Mediatorless Bio-Photovoltaic (BPV) System." *Physical Chemistry Chemical Physics* 14 (35): 12221–29. https://doi.org/10.1039/c2cp42526b.

194. Gholipour, S., Correa-Baena, J. P., Domanski, K., Matsui, T., Steier, L., Giordano, F., … Hagfeldt, A. (2016). Highly Efficient and Stable Perovskite Solar Cells based on a Low-Cost Carbon Cloth. Advanced Energy Materials, 6(20), 1–7. https://doi.org/10.1002/aenm.201601116

195. Rasmussen, M. & Minteer, S. D. Thylakoid direct photobioelectrocatalysis: Utilizing stroma thylakoids to improve bio-solar cell performance. *Phys. Chem. Chem. Phys.* **16**, 17327–17331 (2014).

196. Choi, D., Bosca, A., Pedros, J., Martinez, J., Barranco, V., Rojo, J., Kim, Y. Calle, F., Improvement of the adhesion between polyaniline and commercial carbon paper by acid treatment and its application in supercapacitor electrodes. Composite Interfaces, vol 23, Issue 2, 133-143 (2016), doi: 10.1080/09276440.2016.1112221.

197. Su, T., Hsieh, T., Hong, C. & Wei, T. Electrodeposited Ultrathin TiO 2 Blocking Layers for Efficient Perovskite Solar Cells. *Nat. Publ. Gr.* 1–8 (2015) doi:10.1038/srep16098.

198. Do, T. T., Hong, H. S., Ha, Y. E., Park, C. Y. & Kim, J. H. Investigation of the property change of polymer solar cells by changing counter anions in polyviologen as a cathode buffer layer. *Macromol. Res.* **23**, 177–182 (2015).

199. Sangiorgi, A., Bendoni, R., Sangiorgi, N., Sanson, A. & Ballarin, B. Optimized TiO2 blocking layer for dye-sensitized solar cells. *Ceram. Int.* **40**, 10727–10735 (2014).

200. Endrődi, B., Kecsenovity, E., Rajeshwar, K. & Janáky, C. One-Step Electrodeposition of Nanocrystalline TiO2 Films with Enhanced Photoelectrochemical Performance and Charge Storage. *ACS Appl. Energy Mater.* **1**, 851–858 (2018).

201. Reyes-Coronado, D. *et al.* Phase-pure TiO2 nanoparticles: Anatase, brookite and rutile. *Nanotechnology* **19**, (2008).

202. Jeong, E. *et al.* Pinhole-free TiO2/Ag(O)/ZnO configuration for flexible perovskite solar cells with ultralow optoelectrical loss. *RSC Adv.* **9**, 9160–9170 (2019).

203. Patra, S. *et al.* Low-temperature electrodeposition approach leading to robust mesoscopic anatase TiO2 films. *Sci. Rep.* **6**, (2016).

204. Lawman, G. M. & Hammond, P. T. Solid-state dye-sensitized solar cells combining a porous TiO2 film and a layerby-layer composite electrolyte. *Small* **1**, 1070–1073 (2005).

205. Grätzel, M. Sol-gel processed TiO2 films for photovoltaic applications. *J. Sol-Gel Sci. Technol.* **22**, 7–13 (2001).

206. Ashkarran, A. A. & Mohammadizadeh, M. R. Superhydrophilicity of TiO2 thin films using TiCl4 as a precursor. *Mater. Res. Bull.* **43**, 522–530 (2008).

207. Hsu, C. P. *et al.* EIS analysis on low temperature fabrication of TiO2 porous films for dye-sensitized solar cells. *Electrochim. Acta* **53**, 7514–7522 (2008).

208. Yan, H., Wang, X., Yao, M. & Yao, X. Band structure design of semiconductors for enhanced photocatalytic activity: The case of TiO2. *Prog. Nat. Sci. Mater. Int.* **23**, 402–407 (2013).

209. Ward, M. D., White, J. R. & Bard, A. J. Electrochemical Investigation of the Energetics of Particulate Titanium Dioxide Photocatalysts. The Methyl Viologen-Acetate System. *J. Am. Chem. Soc.* **105**, 27–31 (1983).

210. Proux-Delrouyre, V. *et al.* Electrocatalytic Investigation of Light-Induced Electron Transfer between Cytochrome c6 and Photosystem I. *J. Am. Chem. Soc.* **125**, 13686–13692 (2003).

211. Ogunsolu, O. O., Wang, J. C. & Hanson, K. Increasing the Open-Circuit Voltage of Dye-Sensitized Solar Cells via Metal-Ion Coordination. (2017) doi:10.1021/acs.inorgchem.7b01531.

Appendix A:NREL Best Efficiency Chart 07262021